UNIVERSITY OF CAPE TOWN
IYUNIVESITHI YASEKAPA • UNIVERSITEIT VAN KAAPSTAD

# Understanding HCCI characteristics in mini-HCCI engines

***Author:***

***Kyle Collair***

*Supervised by:*

*Mr. Gareth Floweday and Dr. Andy Yates*

*Sasol Advanced Fuels Laboratory*

sasol
*reaching new frontiers*

**A dissertation submitted to the Department of Mechanical Engineering, University of Cape Town, in partial fulfilment of the requirements for the degree of Master of Science in Engineering.**

Cape Town, South Africa
August 2006

## *Declaration*

1. I know the meaning of plagiarism and declare that all of the work in the document, save for that which is properly acknowledged, is my own.
2. Each significant contribution to, and quotation in this project from the works of other people has been attributed, cited and referenced.
3. I have not allowed and will not allow anyone to copy my work with the intention of passing it off as his or her own work.

Signature: ____________________________

# *Acknowledgments*

This study was funded and supported by Sasol Technology Fuels Research which is headed by Mr Paul Morgan.

The author wishes to thank and extend his gratitude towards the following people for their contributions to this project:

- **Gareth Floweday** (Sasol Advanced Fuels Laboratory, University of Cape Town) for his diligent supervision, inspiration and invaluable support.
- **Prof. Andy Yates** (Sasol Advanced Fuels Laboratory, University of Cape Town) for his support, guidance and motivation.
- **Owen Metcalfe** (Sasol Advanced Fuels Laboratory, University of Cape Town) for his CFD breathing model and his patience.
- **Ian Lemberger** (Sasol Advanced Fuels Laboratory, University of Cape Town) for his help in constructing the engine testing rig.
- **The mechanical engineering workshop staff** at the University of Cape Town for their continuous assistance and infinite patience.
- **Dr Martin Hepperle** (Institute of Aerodynamics, Germany) for his guidance in setting up the propeller characteristics model.
- **Kate Schrire and my family** for their loving support and continuous motivation.

# *Synopsis*

This study examines the successful use of Homogeneous-Charge, Compression-Ignition (HCCI) combustion in a standard issue model-aero "diesel" engine. This two-stroke engine, unlike the more common glow-plug versions, operates without any form of combustion initiator. The fuel and air are premixed using a simple carburettor and ignited by piston compression only. The engine therefore operates in HCCI-mode even though it is referred to as a "model diesel engine".

Of particular interest is the fact that the engine is easily started from cold, warm and hot conditions. It runs stably from idle to over 11000rpm and is shown to run at high load points across the speed range with extremely conservative pressure rise rates. Furthermore, this engine is shown not to exhibit any knocking (high pressure oscillations) within its normal range of operation.

The speed-load operational envelope of the engine is mapped out using a range of propellers and a propeller speed-load calibration rig. Air/fuel ratio, inlet air and exhaust gas temperatures are examined within this operational envelope. Areas of unstable operation and extremities in stable operation are also mapped out and discussed. The engine's use of inlet throttling, crankcase pumping and residual exhaust gas metering is modelled and discussed. In addition, the engine's inherent ability to maintain constant combustion phasing over varying operating conditions is also investigated.

The standard model-aero engine fuel (a mixture of paraffin, ether, castor oil and ignition improver) is tested in an Ignition Quality Tester$^{TM}$ (IQT$^{TM}$) and in a larger 4-stroke variable compression-ratio HCCI engine. These results are then compared with the HCCI operating characteristics of n-heptane in this larger engine.

A computational fluid dynamics (CFD) model was successfully used to investigate the flow regimes, thermal profile and spatial fresh-charge distribution within the engine. This CFD simulation showed a highly stratified thermal distribution with a significant boundary layer. A small level of mixture inhomogeneity was observed in the CFD simulation results. However slight, this resulted in similarly inhomogeneous burning as observed in the engine with combustion being initiated in the four zones of higher fresh charge concentration.

A single-zone, implicit, discrete, pseudo-dimensional combustion simulation was used to investigate changes in combustion phasing due to changes in operating conditions. The results of the combustion simulation followed similar trends observed in engine-testing.

# TABLE OF CONTENTS

1. INTRODUCTION

2. BACKGROUND AND THEORY REVIEW

3. CHARACTERISING THE ENGINE LOAD

4. FUEL-RELATED TESTING

5. ENGINE TESTING

6. ENGINE MODELLING

**7. CONCLUSIONS AND RECOMENDED FURTHER WORK**

**8. REFERENCES AND OTHER SOURCES**

**9. APPENDICES**

# LIST OF FIGURES

# LIST OF TABLES

# DEFINITIONS, ACRONYMS AND ABBREVIATIONS

**AI:** Auto-ignition (see auto-ignition)

**AFR:** Air-Fuel Ratio (mass basis)

**Angle Of Attack:** The angle of deviation from horizontal for a wing section.

**Auto-ignite/Auto-ignition:** Spontaneous combustion without any form of external initiation (such a spark or glow-plug). Characterised by the simultaneous bulk combustion of the reactants

**BDC:** Bottom dead centre – the piston is at its lowest position in the cylinder

**BMEP**: Break Mean Effective Pressure – A concept used to describe the performance of engines with different displacement

**CAD**: Crank Angle Degrees

**Cetane:** Concept used to describe to auto-ignition performance of (usually diesel-like) fuels. A higher cetane number implies a propensity for auto-ignition

**CFD:** Computational Fluid Dynamics

**Chemkin:** Chemistry modelling package

**Chord:** The characteristic length of a wing cross section

**Cool-Flame:** Low temperature heat release characteristic of fuels with pronounced NTC behaviour

**CR:** Compression Ratio. Unless otherwise stated refers to the geometric compression ratio

**DCN**: Derived Cetane Number

**DEE:** Diethyl-Ether

**EGR:** Exhaust Gas Recirculation

**EVC:** Exhaust Valve Closing

**EVO:** Exhaust Valve Opening

**HCCI:** Homogeneous Charge, Compression Ignition

**IQT$^{TM}$:** Ignition Quality Tester

**IVC**: Inlet Valve Closing

**IVO:** Inlet Valve Opening

**GTL**: Gas-To-Liquids, A generic term referring to liquid fuels derived from gas

**Knock/Knocking:** High pressure oscillations caused by simultaneous, uncontrolled auto-ignition of un-reacted combustion gasses. The high pressure oscillations are caused by resulting shock waves reflecting off the inside of the combustion chamber. Often knock may be heard as a "pinging" or "hammering" sound accompanied by rough running. Knock is usually detrimental to engine performance and longevity

**Lambda ( ):** Refers to the AFR (inverse of equivalence ratio, ) with =1 equivalent to the stoichiometric AFR. >1 indicates lean fuelling whereas <1 indicates rich fueling

**LTFT:** Low Temperature Fischer Tropsch refining process

**MFB:** Mass Fraction Burned referring the fraction of fuel burned

**n-Heptane:** Paraffinic hydrocarbon with seven carbon atoms and saturated with hydrogen. Primary reference fuel with zero octane rating often used to calibrate the performance of other fuels. n-heptane has a strong tendency to auto-ignite.

**NOx:** Undesirable generic Nitrous Oxide gasses formed during combustion
**NTC**: Negative Temperature Coefficient
**Particulate:** Soot-like emission usually associated with diesel engines
**PAW:** Progress Aero Works – The manufacturers of the engine used in this study
**PPM or PPMC**: parts per million or parts per million carbon
**PT**: Pressure Transducer
**R/C:** Radio Controlled
**Scavenging:** Combined intake and exhaust procedure utilised in two-stroke engines. As both intake and exhaust valve opening usually have overlap in a two-stroke engine a positive pressure differential between the intake and exhaust is required to drive fresh charge into the cylinder and remove as much of the remaining exhaust gas as possible
**Short Circuiting:** Undesirable consequence of having the intake and exhaust valve opening overlap in a two-stroke engine is that some fresh charge usually passes straight through the cylinder and out the exhaust port without combusting
**SOC:** Start of Combustion
**Stalling:** The air velocity flowing over a wing section is too low to produce any lift
**Stoichiometric:** Theoretical chemically correct mixture resulting in the hypothetical complete reaction of all reactants
**TDC:** Top Dead Centre – the piston is at its highest position in the cylinder
**THC**: Total Hydrocarbons
**Windmillling:** When a propeller is auto-rotated by the incoming air velocity causing drag without providing and thrust

# 1. INTRODUCTION

Model-aero engines are most commonly used to power radio-controlled model aircraft and are split into two categories: “glow-plug” and “model-diesel”. The latter, despite being referred to as a “model diesel engine”, is in fact a homogeneous-charge, compression-ignition (HCCI) engine. It uses a simple carburettor to premix the fuel and air, and ignites this nominally homogenous mixture using only the heat of compression. In contrast, glow-plug engines use a glow-plug to initiate combustion. This type of HCCI engine is of particular interest largely because it is able to operate over a wide range of speed and load with good transient ability. It does so without any undesirable effects on performance or damage to the engine in a manner similar to glow-plug model-aero engines, but in a manner extremely unusual for HCCI engines.

Various control strategies have been used in an attempt to extend the operating range and transient operability of HCCI engines by maintaining suitable combustion phasing despite changing operating conditions. Most of these involve trying to mitigate the changes to the combustion phasing caused by varying operating conditions, but often these methods of control are too slow to respond to the rapidly changing operating conditions. The model-aero engine is, by contrast, extremely simple and operates without any of these complex controls. Once the air-fuel ratio and compression ratio are correctly set up, one need only adjust the throttle to vary the load/speed with the engine running much like any other type of model-aero engine. The effect of the throttle in this two-stroke engine simultaneously meters in fresh charge and controls exhaust residual fraction in such a way as to maintain appropriate combustion phasing.

This project sought to investigate the operating range and combustion characteristics of the model-aero engine. Of particular interest were the limits of stable combustion and what operating characteristics defined these limits. It was also of value to investigate the combustion behaviour outside of the engine’s operating range (i.e. knocking or misfiring). In addition, investigations into the engine’s general behaviour and combustion-phasing response to changes in operating conditions sought to reveal factors which enabled HCCI-operation over a broad operating range and allowed good transient operation. The original fuel components were tested to determine their role as possible HCCI-enablers.

Experimental work included:

- Fuel-component testing in an Ignition Quality Tester (IQT$^{TM}$) apparatus.
- Comparative fuel testing between the model-aero fuel and n-heptane in a Ricardo E6 test engine operating in HCCI mode.
- Characterising the speed vs. load properties of the propellers used for testing the model-aero engine.
- Running the model-aero engine at a variety of speed-load points thus mapping out its operating range.
- Investigating areas outside the normal operating range (knocking, misfiring)
- Observing changes in combustion phasing in response to changes in operating conditions.

Modelling work included:

- Modelling the speed vs. load characteristics of a variety of propellers thus determining the most suitable sizes for testing.
- CFD modelling of the engine's breathing characteristics to determine:
  1) The in-cylinder spatial temperature profile.
  2) The affect of residual exhaust-gas fraction on cylinder-gas composition, temperature and concentration.
  3) The effects of in-cylinder flow conditions as result of the engine's two-stage breathing process and unique port arrangement.
- An Excel-based numerical simulation of the engine was used to investigate the effects of speed and load on combustion phasing as well their combined effects on achieving constant combustion phasing over a variety of load and speed points.

This report begins with a review of the relevant background theory regarding:
  - Model-aero propellers
  - HCCI
  - Model-aero engines
  - Fuels

This is followed by three sections describing all the experimental work, but also includes the modelling work regarding the model-aero propellers. The next section describes the engine-modelling investigation including both the CFD simulation and the Excel combustion model. This report concludes in a chapter in which conclusions are drawn and recommendations are made regarding further work.

# 2. BACKGROUND AND THEORY REVIEW

## 2.1. MODEL AERO PROPELLERS

### 2.1.1. General Behaviour

The propellers used in this study were all fixed-pitch and of the Master Airscrew K-series type. The naming convention (eg. "12x6") refers to the diameter in inches by the pitch in inches (at 75% of the blade radius). The pitch of a propeller refers to the theoretical, ideal distance travelled by the propeller for a single revolution (analogous to screw threads). For two propellers of the same diameter the one with the larger pitch will require more torque for a given rpm [1, 2, 3]. Given two propellers with the same pitch the one with the larger diameter would require a larger torque for a given rpm [1, 2, 3]. It is not possible to decouple the speed-load characteristics of a fixed pitch propeller and as a result, the very regular behaviour of such a propeller was described using the following equation:

$T = C_t \times \rho \times n^2 \times \phi^5$ [2, 3] (Equation 1)

- T = Torque (Nm)
- $C_t$ = Torque performance coefficient
- = Air density (kg/m$^3$)
- n = Propeller rotational velocity in (rps)
- = Propeller diameter (m)

A graphic representation of this behaviour is displayed in Figure 1 showing the torque increasing as speed increases.

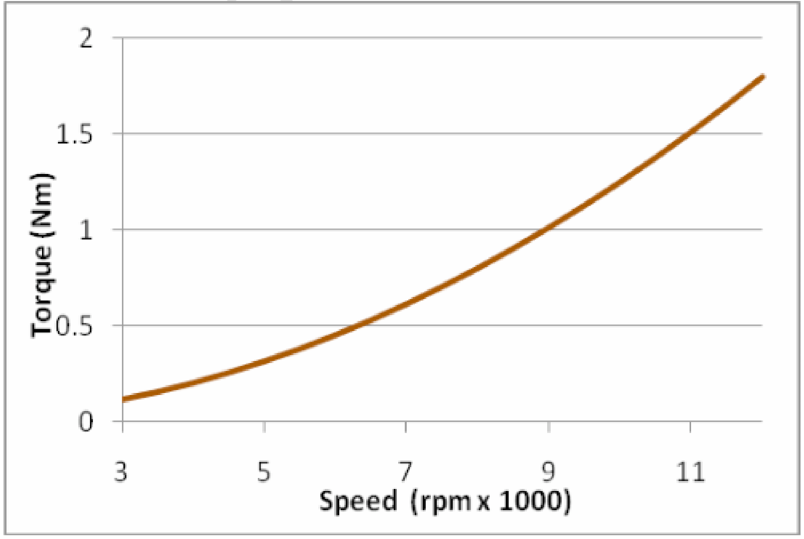

**Figure 1:** Typical torque vs. speed behaviour for a fixed pitch propeller as modelled using equation 1 for a 15x10 propeller

### 2.1.2. Propeller Performance Modelling using Glauert Blade Element Theory

There are some simple explicit formulae which describe the performance behaviour of propellers. Unfortunately these describe the behaviour of propellers when an aircraft is in motion. In this situation, the propellers experience an incoming air velocity equal to the velocity of the aircraft. These relationships were therefore unsuitable for the conditions in this study since the propellers were tested under bench conditions with zero incoming air velocity.

Glauert Blade Element Theory is a technique used to analyse the aerodynamic behaviour of a spinning blade – in this case a propeller [3]. It is a technique developed for the discreet analysis of propeller blades and does not require a non-zero incoming air velocity. Glauert Blade Element Theory was therefore chosen as an appropriate method of determining simple propeller performance characteristics.

This method analyses discreet sections of the propeller blade with the overall blade characteristics obtained through a summation of the characteristics of all the discreet parts. Each individual blade element is analysed as a discreet aerofoil section. The fundamental concepts of this method rely on each discreet section behaving like a spinning section of a wing with differing characteristic dimensions (chord, angle of attack etc.) depending on which element is being analysed.

The lift and drag for each section is determined as if each element is a regular wing (with the air velocity provided by the tangential velocity of the spinning blade element). The model uses a stream-tube concept to take account of the stationery air drawn into the spinning propeller where it is then accelerated and swirled around in the slipstream. This method also incorporates the relevant changes in both axial and angular momentum of the air through the spinning propeller.

This method does not account for radial flow components or secondary flow effects such as tip vortices. As a result, the model tends to under predict torque slightly depending on the operating conditions [3]. This was deemed acceptable as the discrepancy is relatively small (with overall efficiency over predicted by 5-10%). It is also limited by the number of discreet sections per blade (more sections yields more accuracy, but with diminishing gains in accuracy as the number of sections increase). It is worth noting that the model breaks down under extreme operating conditions such as the blade becoming stalled or when a large portion of the blade is wind-milling. Neither of these phenomena were a concern for this study as none of the propellers ever operated under such conditions.

During the formulation of the model, absolute accuracy was less important than easy implementation and obtaining useful results as this model was only used to guide the selection of propellers for testing and not meant to replace experimental speed-load characterisation.

A reproduction of Auld and Srinivas' implementation (as used in this study) of this method may be found in appendix 2.

## 2.2. HOMOGENEOUS-CHARGE COMPRESSION-IGNITION (HCCI)

HCCI engines have the potential ability to combine into one system, the two respective benefits of conventional gasoline (SI) and diesel (CI) engines; namely low emissions and high efficiency [4].

SI engine performance and efficiency is fundamentally limited due to its reliance on spark-initiated, flame-front propagation. Spark ignition flame propagation requires a near-stoichiometric mixture which limits the use of leaner combustion in homogeneous-charge SI engines [5]. The speed of flame-front propagation and possible auto-ignition of the unburned mixture (knocking) limits the maximum compression ratio of SI engine and with it the efficiency benefits associated with an increased compression ratio.

In favour of SI engines are their high fuel conversion efficiencies at near-stoichiometric conditions [5] and very low emissions due to the easy implementation of effective exhaust gas after-treatment systems in the form of the commonly used three-way catalyst. SI engines also have high power to weight capabilities due to the lower structural strength required by the lower compression ratios combined with high speed capabilities.

CI engines traditionally have higher compression ratios and a leaner overall air-fuel ratio (AFR). This is due to the fact that they do not rely on a spark or flame–front propagation. Instead, CI engines initiate combustion by spraying fuel into a hot, pressurised combustion chamber. The combustion process is then limited by the fuel droplet evaporation, mixing and diffusion [5]. The result of which is that while the bulk AFR may be lean, the local conditions where combustion occurs may be very rich. These rich conditions result in high local combustion temperatures (increasing $NO_x$ production) and incomplete oxidation of the fuel (resulting in increased particulate formation). So while CI engines have better thermodynamic efficiency due to lean bulk AFR operation and high compression ratio, they typically have high $NO_x$ and/or particulate emissions. The lean operation also makes effective exhaust gas after-treatment more difficult [6] and more expensive.

A classical HCCI engine aspirates and compresses a homogeneous air-fuel mixture (like a carburettor or port injected gasoline engine). This mixture is auto-ignited purely by compression with no external ignition control mechanism (such as a spark-plug, glow-plug or direct fuel injection). The homogeneous bulk combustion of the mixture results in relatively low temperature combustion which can potentially lower $NO_x$ formation [7]. The homogeneity of the combustion also decreases particulate formation as there are no locally rich zones to initiate particulate formation [8]. In addition, the auto-ignition combustion mechanism is not limited to a near-stoichiometric mixture, but allows for leaner, more thermally efficient combustion [4]. Unlike a diesel which may have a lean bulk air-fuel ratio with locally rich areas, the entire mixture in an HCCI engine has a nominally identical air-fuel ratio and thus burns more uniformly. HCCI engines also have the ability to operate without a throttle (like a diesel) which eliminates pumping losses at part-load and increases efficiency.

In an HCCI engine the burn duration and combustion phasing are all controlled purely by combustion chemistry. Aspects of combustion such as burn-duration can, however, be affected by physicals conditions inside the cylinder such as thermal and fuel stratification. The lack of external control over the ignition point and combustion behaviour has made wide-range HCCI operation a challenge [10, 11]. As a result, classical HCCI engines are typically limited in their speed-load operational envelopes, with cold starting and extremities of conventional engine speed and load points remaining difficult to attain.

The operating range limits are defined by the following factors:

- Low-load: very lean operation results in very low combustion temperatures and usually misfiring cycles (or sometimes no combustion). Both lead to very high CO and HC emissions and the low temperatures not allowing correct phasing
- High-load: rapid burning results in high pressure rise rates and knocking
- Low-speed: the time-effect on the auto-ignition delay can advance combustion phasing causes high pressure rise rates and sometimes knocking
- High-speed: the time effect on the auto-ignition delay can retard combustion phasing causing misfire

Transient operation is also difficult due to the available methods of load and speed control. Varying the speed or load can often simultaneously affect any number of critical factors such as air-fuel ratio, inlet pressure or the residence time of reactants. Each of these (and other) factors effect the combustion chemistry kinematics and auto-ignition reactions the results of which are that the optimum operating conditions for one point are often not easily changed to match the optimum operating conditions at another point [12,13].

Due to these difficulties, experimental implementations are often mixed-mode HCCI engines which incorporate many types of control systems into one engine so as to achieve HCCI operation over a wide range while using some other conventional combustion in areas unattainable by HCCI. These concepts may take the form of a stratified charge, direct injection gasoline spark-assisted HCCI engine with variable compression ratio (as pursued by Mercedes-Benz in their DiesOtto concept). This is far from a pure, classical HCCI engine, but allows for many of the benefits of HCCI (albeit for only part of the engine's operational map). Unfortunately these engines are more expensive than conventional engines due to their complexity.

Due to the potential benefits of expanding the range of operation and transient operating ability for HCCI these have become primary objectives in pure and mixed-mode HCCI engine development.

## 2.3. MODEL-AERO ENGINES

The Progress Aero Works (PAW) two-stroke, model-aero HCCI "diesel" engine is an example of a very simple internal combustion engine available on the market today and its design has remained relatively unchanged for over fifty years. Conversely, research HCCI engines and conceptual HCCI implementations are some of the most complex internal combustion engines. These engines often employ complex control strategies such as variable valve timing, heated inlets and multiple fuel injection events all in an attempt to control combustion phasing. The PAW engine in this study used none of these controls to achieve reliable, repeatable HCCI combustion. The specifications for the PAW-40 engine used in this study can be found below:

**Table1:** PAW40 engine specifications

| | **Value** | **Unit** |
|---|---|---|
| **Displacement** | 6.55 (measured) | $cm^3$ |
| **Bore** | 20.32 (measured) | mm |
| **Stroke** | 20.08 (measured) | mm |
| **Compression Ratio** | Variable | |
| **Speed Range** | 4000-11500 (manufacturer's claim) | rpm |
| **Rated Output** | 708 (manufacturer's claim) | Watts |
| **Max Prop** | 13x8 or equivalent (manufacturer's claim) | |
| **Min Prop** | 10x6 or equivalent (manufacturer's claim) | |

The unusual arrangement of the engine's intake system has a substantial effect on the engine's performance characteristics due to a combination of the following:

- Conventional single-jet carburettor with barrel throttle valve
- Two-stage breathing through the crank case (crank-case scavenged)
- The port arrangement (in-cylinder flow dynamics and valve timing)

The model aero engine utilises a two-step breathing process that is commonly used in small two-stroke engines. Air and fuel are first aspirated into the crank case, where the mixture is then pressurised before entering the cylinder. A regular barrel-type throttle valve on the carburettor controls the mass of air and fuel admitted to the crank-case by varying the inlet pressure of the mixture entering the crank-case. During the compression stroke, the rising piston creates an expanding volume in the crank-case. As a result, a fresh charge is sucked into the crank-case due to the pressure differential. Shortly after TDC, the crank-case inlet port closes and the crank gasses are pressurised by the descending piston (in the sealed crank-case). Pressurised crank-case pumping means the mixture in the crank-case is always above atmospheric when the cylinder inlet valves open. This improves exhaust gas scavenging and significantly increases the performance of two-stroke engines.

The engine is not boosted, however, and since the exhaust ports (open to nominally atmospheric pressure) are the last to close, the pressure at EVC is also always close to atmospheric pressure. Therefore only the mass of fresh charge admitted to the cylinder varies with different throttle positions, with the balance made up of exhaust residuals. Therefore closing the throttle not only decreases engine load due to decreased fuelling, but also increases exhaust residuals. Since the engine is run with a fixed propeller, engine speed also drops with decreased load.

Model-Aero Engine Operating Cycle through 360 CAD from BDC to BDC:

1. BDC @ $-180^o$
2. Crank-case inlet-port opens @ $-133^o$
3. Aspiration of fresh charge into crank case (with possible momentum effects improving flow into the cylinder due to the small overlap in port-timing)
4. Cylinder intake port closes @ $-126^o$
5. Exhaust port closes @ $-116^o$
6. Compression of in-cylinder reactants
7. Combustion (SOC close TDC for typical timing)
8. TDC @ $0^o$
9. Expand combusted gasses
10. Crank case port closes @ $45^o$
11. Crank case gas compression (by descending piston)
12. Exhaust port opens (blowdown) @ $116^o$
13. Cylinder intake port opens @ $126^o$
14. Fresh charge fills cylinder when $P_{cylinder} < P_{crank\ case}$
15. BDC @ $180^o$

**Figure 2:** Unmodified PAW-40 engine. Note the compression-ratio adjustment screw protruding from the head

Previous studies conducted on model aero engines have concentrated on the more common glow-plug engines rather than the HCCI engine being considered in this study (aka “model-aero diesel”). As a result, glow-plug engines have been well documented and of the studies considered, most investigate the general performance and combustion-characteristics of the engine (much like the general aims of this study). These types of engines have limited application other than powering model-aero aircraft. Other than general investigations, previous studies have also sought to investigate and possibly remedy the problems limiting broader use of these engines as power sources; namely, high emission, noise and vibrations.

While model-aero HCCI engines also have limited applications, they at least share a fundamental combustion mechanism with larger research HCCI engines. This might allow for information transfer between the obscure model-aero HCCI engine and the possibly-mainstream, larger HCCI engine. Of the studies reviewed, little was discussed regarding the scalability of the mechanisms which enable HCCI operation in the model-aero engine and what could be carried over to enable HCCI operation in other types of HCCI engines.

Manente et al. investigated an ether-fuelled model-aero HCCI engine suggested the following about these types of engines [14]

- High emissions levels due to unique NOx formation mechanisms not found in classical HCCI engines, High HC and CO emissions due to incomplete combustion of the fuel (as found in most 2-stroke engines)
- Low IMEP values due to poor combustion efficiency and short circuiting of the in-coming fresh charge
- Multi-stage heat release indicative of “cool-flame” combustion

The body of the report contains further more specific references to this body of research and each case is discussed in detail as it is encountered.

## 2.4. FUELS

HCCI combustion phasing relies entirely on the auto-ignition characteristics of the fuel (under the operating conditions of the engine). As a result, its importance is paramount to understanding the HCCI operating characteristics of any engine. The auto-ignition delay of a fuel determines the combustion phasing while aspects such as burn duration affect the heat release rate of the burning mixture. Incorrectly matching these aspects to an engine and operating conditions will result in undesirable combustion phenomena or possibly no combustion at all.

The auto-ignition characteristics of a fuel are strongly dependent on its response to increases in temperature and pressure [15]. Increasing the temperature of an air-fuel mixture generally shortens the auto-ignition delay of the mixture. However some fuels exhibit a limited range of "negative temperature coefficient" (NTC) behaviour where increasing test temperatures results in increased ignition delay times as shown in Figure 4 [15]. This NTC behaviour is associated with a "cool flame" reaction which precedes the main heat release. The cool flame reaction causes a relatively small temperature rise, but significantly influences the ignition delay of the main heat release.

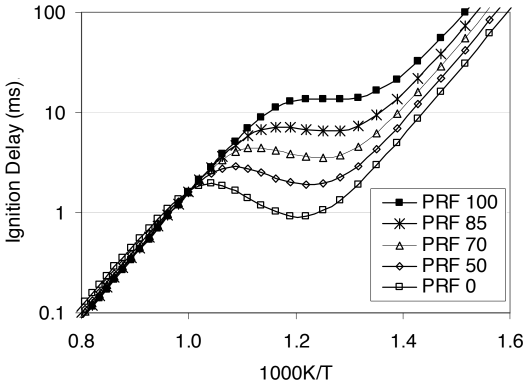

**Figure 3:** Fuels with pronounced NTC behaviour [15]

The model-aero engine uses a unique fuel blend called D1000 which consists of conventional kerosene, diethyl-ether, isopropyl-nitrate and castor oil.

**Table2:** D1000 fuel specifications and properties

| **D1000 Fuel Composition** | | |
|---|---|---|
| **Component** | **Volume %** | **Characteristics** |
| **Kerosene** | 35 | Diesel like paraffinic fuel |
| **Di-Ethyl-Ether** | 35 | High cetane, good vaporisation |
| **Castor Oil** | 28 | 2-Stroke lubricant |
| **Isopropyl-Nitrate** | 2 | Very high cetane ignition improver |

The two main combusting fuel components have similar auto-ignition characteristics. Data on diethyl-ether suggested it was a two-stage auto-ignition fuel (as opposed to other alcohol fuels like TAME or MTBE which have single stage behaviour) [16]. Kerosene is also known to exhibit definite two stage auto-ignition behaviour [17, 18].

# *3. Characterising the Engine Load – Model Aero Propellers*

## 3.1. THE USE OF PROPELLERS

The main reason for choosing to use propellers and an intermediate calibration rig (instead of directly connecting the engine to a dynamometer) was that the maximum speed for a given propeller also represented the point of maximum power for that propeller. This therefore also represented the optimum engine setup for maximum power from that propeller (as any other setup resulted in a lower speed). Maximum power required optimised combustion phasing [19, 20, 21,22] and tuning the engine in this manner provided a convenient method of simultaneously altering various engine parameters for optimum combustion phasing. Conceivably, a suitable variety of propellers would cover a suitably large area of the engine's operational load and speed map to test its important operating characteristics.

Not using a conventional engine dynamometer bypassed many of the problems ordinarily associated with engine dyno-testing such as; engine vibrations (a substantial issue with the PAW engine), motor/dyno electrical control, power/load matching and cost. A viable electric motor-based engine dynamometer concept was considered, but the power and speed range of the engine made either the electric control hardware or the motor hardware prohibitively expensive with little benefit.

The commonly used Master Airscrew K-Series propellers were used for all the experiments and for all the modelling. They provided a suitably large range of sizes and were commonly available.

## 3.2. NUMERICAL MODELLING

Initially it was unclear which propellers were most suitable for testing the extended operating range of the PAW engine. Modelling an extensive range of propellers was useful in guiding the selection of a few propellers which would be characterised for testing.

### 3.2.1. Modelling Philosophy

The PAW engine manufacturer suggested using a 12x6 (or equivalent) propeller for normal model-flying operation, but testing the engine outside its conventional operating range required insight into the performance of a much larger range of propellers. It was beneficial to the design of the propeller testing rig to know in advance which propellers would likely provide a suitably large operating range.

It also showed the likely limits of the engine testing-range based on the available propellers and it also prevented the purchasing of unnecessary propellers.

The only known properties of the Master Airscrew K-series propellers were those which were easily measured (using a representative sample propeller); for example: pitch, diameter, taper ratio, general shape etc.

The desired outcomes of the model were the torque coefficients for all of the propellers. From these coefficients it was possible to generate the speed vs torque characteristics of all the propellers.

### 3.2.2. Model Formulation

The model formulation of Glauert Blade Element Theory followed instructions provided by Auld and Srinivas [3], and can be found in appendix 1. These instructions were then transformed as directed into MATLAB programming code (A copy of the code with comments may be found in appendix 2). Within MATLAB the data was tabulated to generate a full set of torque coefficients for the set of simulated propellers by manually iterating the model through the different propellers.

### 3.2.3 Modelling Results

The chosen method of analysis provided satisfactory results. The exact physical dimensions of only some of the propellers were known (as the others had not been purchased yet) and as such only these propellers were used to estimate the physical characteristics of a "generic" propeller. It was assumed that any other propellers would not have substantially different proportions (as they were of the same type and therefore assumed to have similar proportions). As a result, all the propellers were modelled using the same taper ratio and chord section with each blade being split into ten discreet sections of equal length.

All propellers were modelled using the same environmental factors (ambient pressure and temperature to determine density). These were chosen sensibly (as standard atmospheric pressure and temperature), but had no effect on the value of dimensionless torque coefficient. This means that a different set of environmental conditions will yield different performance characteristics (higher density requiring a greater torque at a given speed for example), but not a different torque coefficient, which is a unique descriptor of each propeller.

The calculated torque coefficient was used to calculate the torque required by the propeller (for specific operating conditions) at a particular speed according to equation 1. It was possible to use this data to calculate the power and also the BMEP for the PAW engine using a particular propeller at a given rpm.

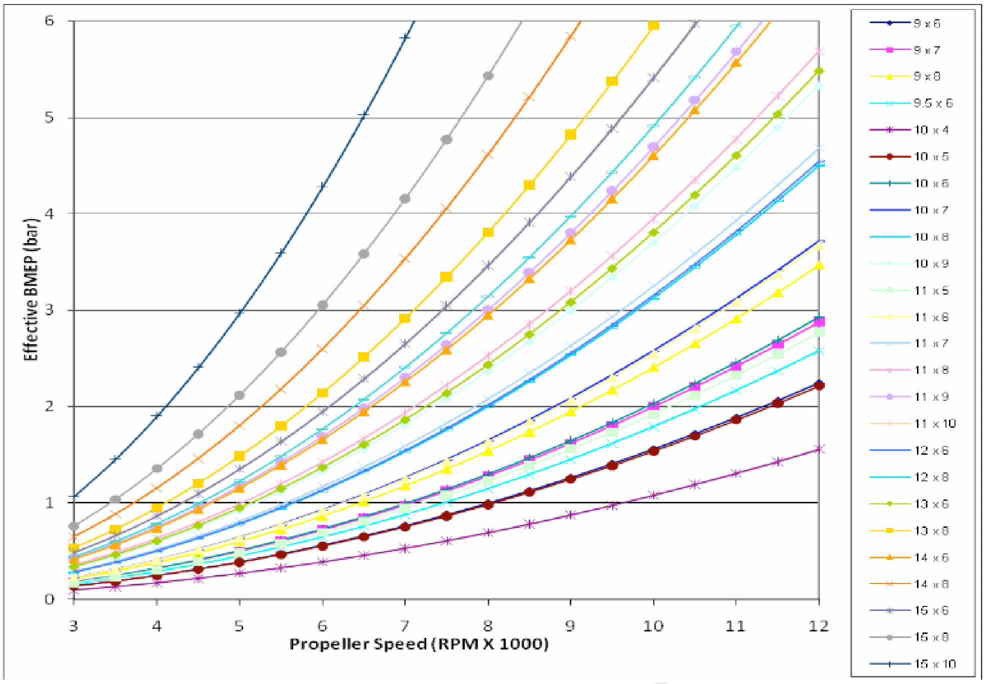

**Figure 4:** The modelling results of the full range of Master Airscrew K-Series Propellers

Note that the specifications provided by the manufacturer for the PAW-40 engine rate maximum output as 708W (or ~5.8 bar BMEP) at 11000rpm and limit the maximum running speed at 11500rpm.

Evaluation of the model results resulted in the following selection of propellers: 11x5, 11x6, 12x6, 13x8, 15x8 and 15x10. Figure 4 showed that using a smaller propeller (than the 11x5) would have resulted in a larger speed-load envelope, but the manufacturer limited the smallest propeller size to 11x5 (or equivalent) presumably to avoid over-speeding the engine and provide a suitably large flywheel effect. The above graph is given in Watts as this provided a more useful guide for choosing an electrical motor for the propeller testing rig.

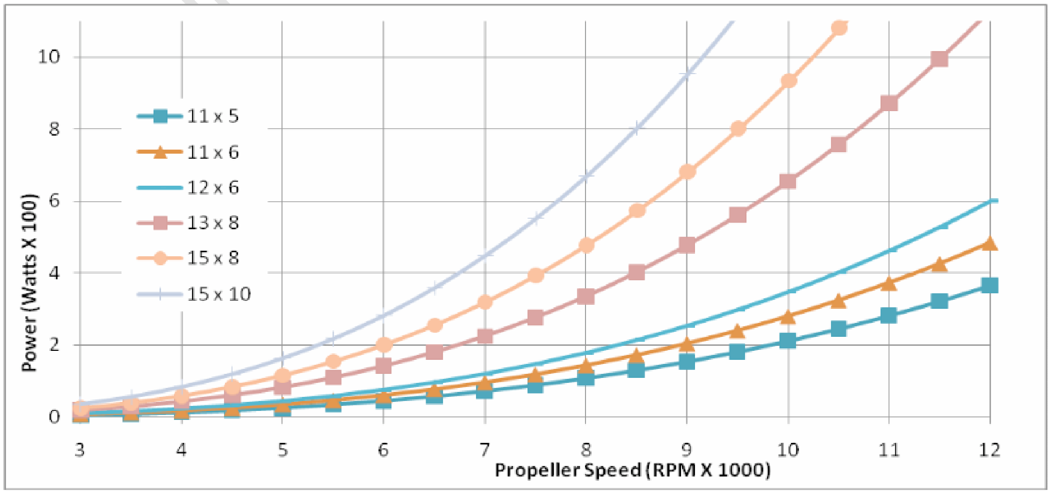

**Figure 5**: Expected operating range using the modelled propellers.

## 3.3. EXPERIMENTAL DETERMINATION OF THE MODEL-AERO PROPELLER CHARACTERISTICS

### 3.3.1. Method and Apparatus

The premise behind the propeller experiments was that each propeller had a unique torque coefficient as described by equation 1. Once determined, this performance coefficient could be used to calculate the torque required to drive the propeller at any speed (for any environmental operating conditions). The results from the propeller testing rig would also show the operating envelope for a given set of propellers thus defining the possible test boundaries of the engine using those propellers.

The requirements for the design were straightforward; measure the different torque values required to spin the propeller at a variety of speeds thus allowing suitably accurate calculation of the torque coefficient for each propeller. It required a means of varying the speed of the propeller within a suitable range and a means of measuring the torque required at that speed. Note that the torque-coefficient should not vary for different measurements.

The rig was constructed using a conventional woodworking router motor (with a power and speed range to match the model-aero engine) to drive the propellers. This motor was mounted on trunion bearings so that any applied torque caused it to rotate freely. A balance beam was then attached to the motor and weights were hung from the beam in order to counteract the torque supplied by the motor. The layout of the rig is shown in Figure 6 and Figure 7 and is similar to the setup used to calibrate larger engine dynamometers. A given combination of weights and the associated lever arm distances of those weights resulted in a known torque value for a particular configuration.

The speed of motor was measured using a photo-tachometer thus generating data points of torque vs. speed from which the propeller torque coefficient could be calculated. The original speed controller for the motor was also retained. Test temperature and air-pressure were both measured.

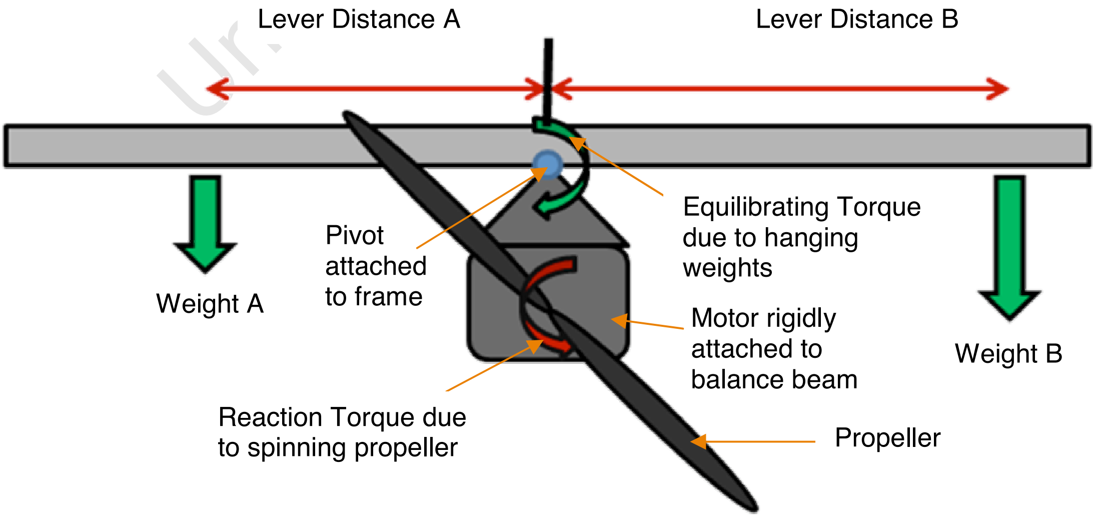

**Figure 6**: Layout of propeller test rig.

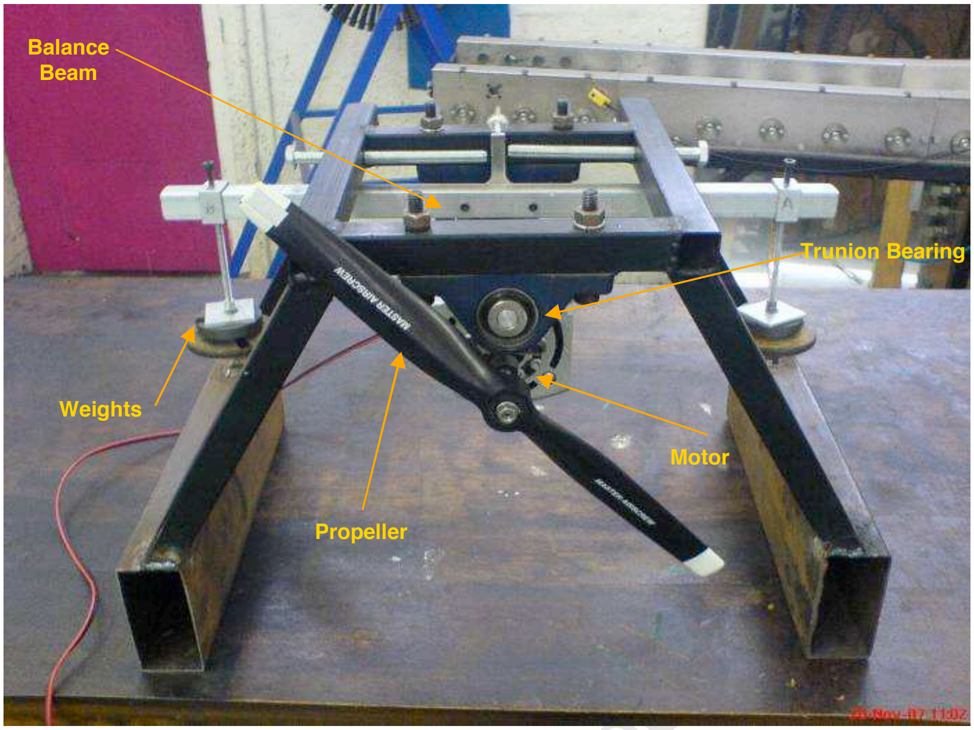

**Figure 7:** Propeller test rig

### 3.3.2. Experimental Results

Each propeller was tested over at least ten speed points to obtain an averaged torque coefficient over the tested range. It was possible to use the averaged torque coefficient to calculate the rpm required for each tested load point as a check. This provided a useful method of evaluating the quality of the data by observing the scatter for each data set.

The data showed very little scatter for all the tested propellers. By using the averaged torque coefficient it was possible to calculate the speed vs. load characteristics for each propeller and extrapolate their behaviour beyond the tested range using the torque coefficient and the aforementioned relationship between propeller torque and speed. Figure 8 shows all the data points superimposed onto the extrapolated characteristic speed vs. load curves (calculated from the averaged Ct) of all the tested propellers.

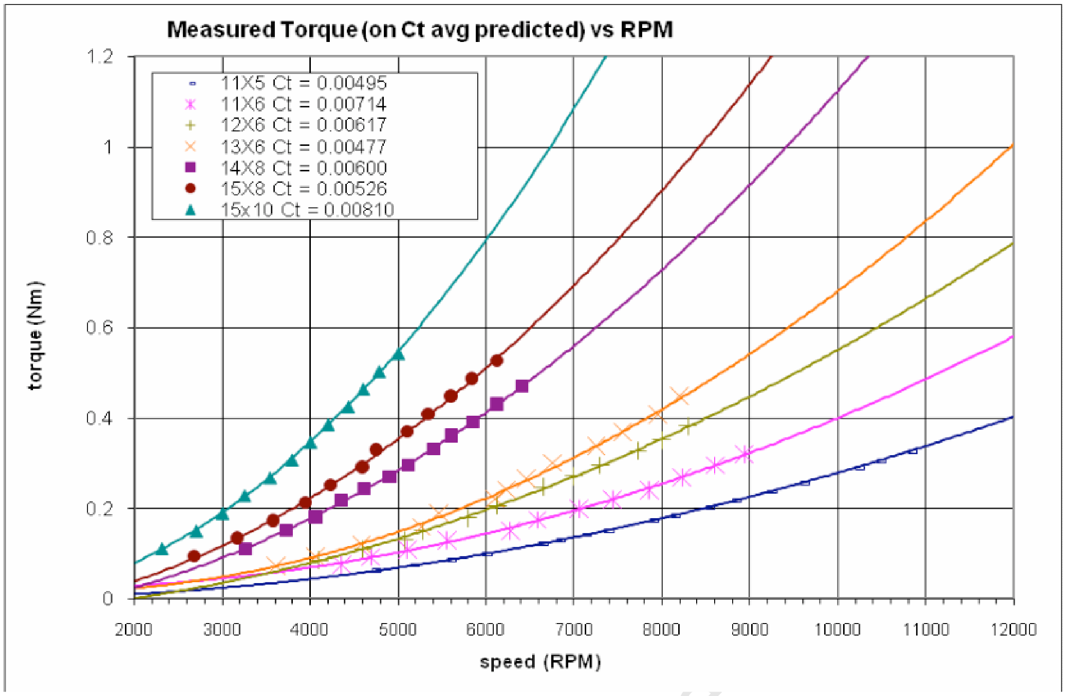

**Figure 8:** Test points superimposed onto the extrapolated load vs. speed behaviour for all the tested propellers.

The averaged values for the torque coefficients (Ct) are also provided in the legend of figure 8.

## 3.4. DISCUSSION OF PROPELLER CHARACTERISTICS

The MATLAB model provided a useful guide for the design of the experimental testing rig, but lacked absolute accuracy. The numerical model under-predicted the torque coefficient (compared to measured results) by between 29% (11x5) and 44% (15x10). The model was expected to under-predict the torque coefficient, but this large discrepancy meant it was not possible to substitute experimental testing with only numerical modelling.

The disagreement between modelling and the experimental results was attributed to oversimplification of the model and incorrect estimation of the physical dimensions of some of the propellers (which had not been purchased at the time of modelling). At the time of modelling it had been assumed that all the propellers would have similar proportions based on only a few measurements. After purchasing the propellers, subtle differences were noted such as: taper ratio, twist ratio and chord length. These factors could have caused the discrepancy, but it was of no value to re-evaluate the model after experimental testing was completed.

The experimental rig produced useful results and clearly showed the expected trends for all the tested propellers. The data from the experimental testing was used to determine the possible testing range for the engine tests and allowed for the precise evaluation of engine load at a particular speed.

# 4. FUEL-RELATED TESTING

## 4.1. MODEL-AERO FUEL:

An investigation into the auto-ignition characteristics of the standard model-aero fuel was carried out due to the largely unknown combustion characteristics of this blend. The basic purpose of each fuel-component could be estimated based on their general properties (eg. diethyl-ether improving vaporisation due to its high volatility), but the specific auto-ignition behaviour of the unique fuel blend required some form of characterisation.

**Table 3:** D1000 formulation

| D1000 blend | |
|---|---|
| **Component** | **Vol %** |
| Kerosene | 35 |
| Diethyl-Ether | 35 |
| Castor Oil | 28 |
| Isopropyl-Nitrate | 2 |

This analysis took two forms: fuel component testing in an Ignition Quality Tester (IQT$^{TM}$) and comparative blended-fuel testing in a Ricardo E6 test engine. A rapid compression-type fuel tester would have been more appropriate due to its homogeneous, compression-initiated combustion, but unfortunately one was not available.

### 4.1.1. IQT$^{TM}$ Testing

The Ignition Quality Tester is a type of combustion bomb commonly used for industrial fuel ignition-quality testing. It is used to test the ignition delay of a fuel by comparing the ignition delay of the test fuel to the known ignition delay of n-heptane. A derived cetane number can then be obtained according to the ASTM method D6890 [23].

***4.1.1.1 Method and Apparatus:*** The IQT$^{TM}$ is used to evaluate diesel-like fuels (fuels prone to auto-ignition) in a non-homogeneous, diesel-like combustion environment. Fuel is sprayed through a high pressure injector into a hot, pressurized environment (in order to aid auto-ignition). The instrumentation in the IQT$^{TM}$ measures the ignition delay of the fuel for a fixed set of test conditions. The testing procedure involves first adjusting the test conditions so that the known ignition delay of n-heptane is achieved as a reference. The cetane rating of the fuel is then calculated based on ignition delay of the fuel relative to n-heptane over an average of thirty tests. [23]

Even moderate amounts of castor oil caused injector spray difficulties. Due to the sensitive nature of the test equipment it was decided not to test D1000 (with its high castor oil fraction) first in case it caused the injector to fail. Instead, the individual components were tested first so as to understand the individual combustion characteristics and their relative effect on the ignition quality of the fuel. Diethyl-ether and the kerosene were both tested neat.

Castor oil could not be tested neat (due to concerns about injector spray difficulties), but was blended with kerosene and tested as a mixture. Isopropyl-nitrate was thought to have an extremely high cetane due to its role as an ignition improver. The IQT$^{TM}$ has a limited range (33 to 6o DCN [23]) for which the derived cetane numbers meet the ASTM standard. Isopropyl-nitrate would presumably fall far outside this range so it was therefore also blended with kerosene and tested in a similar manner to the castor oil. Its purpose was also that of an ignition-improving blending agent so testing it neat was less relevant than testing it in a blend. The relative effects of the various blends were then compared to neat kerosene.

D1000 was not tested successfully in the IQT$^{TM}$. Attempted tests repeatedly caused injector difficulties with the IQT$^{TM}$ unable to achieve the required thirty successive tests. As a result, the cetane value for D1000 below was obtained from a previous study using the same formulation in the same IQT$^{TM}$ [24].

***4.1.1.2. Experimental Results:*** Testing in the IQT$^{TM}$ clearly showed the cetane effects of each fuel component. Table 4 shows the test matrix and the results of the tests.

**Table 4:** IQT$^{TM}$ test matrix showing blend compositions and results.

| **Percentage Blend by Volume** | | | | |
|---|---|---|---|---|
| **Ether** | **Kero** | **IsoPropNitro** | **Castor** | **Cetane** |
| 100 | 0 | 0 | 0 | **198.0** |
| 0 | 100 | 0 | 0 | **45.0** |
| 0 | 99 | 0 | 1 | **45.7** |
| 0 | 95 | 0 | 5 | **45.8** |
| 0 | 90 | 0 | 10 | **45.8** |
| 0 | 85 | 0 | 15 | **44.5** |
| 0 | 80 | 0 | 20 | **43.4** |
| 0.0 | 99.0 | 1.0 | 0.0 | **62.0** |
| 0.0 | 98.5 | 1.5 | 0.0 | **66.0** |
| 0.0 | 98.0 | 2.0 | 0.0 | **71.0** |
| 0.0 | 97.5 | 2.5 | 0.0 | **73.6** |
| 35 | 35 | 2 | 28 | **93.0** |

Note the certified test range for the IQT$^{TM}$ only provides accurate cetane rating 6o DCN [23].

The method for rating higher-cetane fuels in the IQT$^{TM}$ [25] was not utilised as the cetane values were only used to gain insight into the relative cetane contributions of each component.

Using 100% kerosene as a baseline for comparison, increased concentrations of castor oil showed very little effect on cetane number as shown in Figure 9. Increasing the fraction of castor oil would, however, lower the overall cetane of the fuel (due to it having the lowest cetane rating).

Once again using 100% kerosene as baseline, increased concentrations of isopropyl-nitrate (ignition improver) increased the cetane rating of the fuel significantly as shown in Figure 10. Isopropyl-nitrate had a significantly higher cetane than any other component and therefore had the single largest effect on the cetane of the blended fuel.

Pure diethyl-ether had higher cetane number than the average for D1000 while kerosene was found to have a lower cetane than the average for D1000 blend. This finding is significant for attaining appropriate combustion phasing under low-temperature conditions (such as cold-starting). The reason is that the highly volatile fraction of the fuel also has a high cetane so the effective cetane is improved under cold conditions as the diethyl-ether will evaporate first and thus "starts" its auto-ignition delay ahead of the kerosene.

In figure 9, note that blending even small amounts of isopropyl-nitrate resulted in a significant cetane improvement. Note also the approximately linear blending relationship.

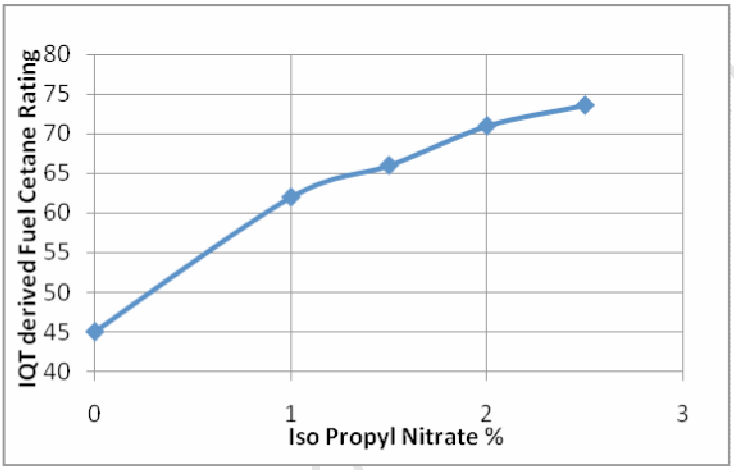

**Figure 9:** Effect of blending small percentages of isopropyl-nitrate with kerosene.

Noting the scale of the graph below, even large amounts of castor oil had very little effect on the cetane rating of the fuel.

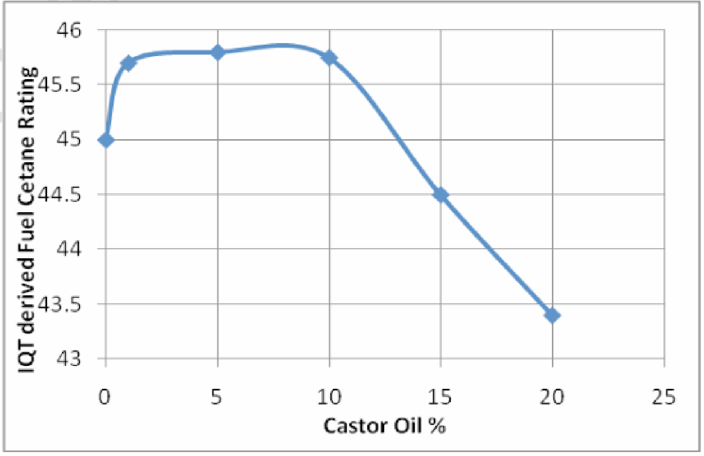

**Figure 10:** Effect of blending castor oil with kerosene.

Linear extrapolation of the test results for isopropyl-nitrate and castor oil allowed for the cetane value for those fuel components to be calculated as shown in Table 5.

Note that the extrapolated value for castor oil may appear to conflict with the graph in Fig 10, but it was calculated using linear extrapolation of the test points and (noting the slope of the graph for larger amounts of castor oil) suitably describes the behaviour of the fuel in larger blend-fractions (like in D1000).

**Table 5:** Fuel-component cetane Properties

| **Component** | **Cetane** |
|---|---|
| **Kerosene (measured)** | 45 |
| **Diethyl-Ether (measured)** | 198 |
| **Castor Oil** | ~25 |
| **Isopropyl-Nitrate** | ~1200 |
| **D1000 (measured)** | 93 |

### 4.1.2. Ricardo E6 Testing

***<u>4.1.2.1. Method and Apparatus:</u>*** As part of a parallel research project, Mr G. Floweday conducted some comparative fuel-blend testing in a Ricardo E6 single cylinder, variable compression ratio research engine.

**Table 6**: Ricardo E6 engine specifications

| | **Value** | **Unit** |
|---|---|---|
| **Displacement** | 507 | $cm^3$ |
| **Bore** | 76.2 | mm |
| **Stroke** | 111.1 | mm |
| **Compression Ratio** | Variable 4.5:1 to 20:1 | |
| **Speed range** | 1000-3000 | rpm |

**Table 7**: IQT derived cetane values for the test fuels

| Test fuel | IQT cetane number |
|---|---|
| D1000 | 93 |
| D1000 minus castor oil | 96.5 (estimated) |
| N-Heptane | 53 |
| LTFT GTL Naphtha | 43.8 |

There were two main questions which the tests were intended to answer:

1) Did D1000 show any unique characteristics which were known to be advantageous for HCCI operation [26]?
2) Did the castor oil reduce combustion heat release rates, or in any other way benefit HCCI operation?

Note that the castor-oil could not be removed from the fuel used in the model-aero engine due to the lubrication requirements of the 2-stroke PAW-40 engine.

The tests were conducted with a fixed heated inlet temperature of 400$^{o}$C. The compression ratio was then adjusted to achieve peak pressure at ~10 CAD ATDC. Three speeds were tested; 600, 1200 and 1800 rpm.

The following air fuel ratios were tested:
=1.5, 2.0, 2.5, 3.0 and 3.5. While the intended test matrix included four fuels, three speeds and five air-fuel ratios, many of the sixty possible test points could not be achieved due to either knocking intensity, instability related to misfire or inability to achieve sufficiently high fuelling due to the high viscosity of the test fuel (e.g. for D1000 at =1.5).

***4.1.2.1. Ricardo E6 Testing Results:*** The model aero fuel blend was found to have an extremely high ignition quality and thus enabled HCCI combustion at very low compression ratios. Using the D1000 formulation without castor oil allowed stable HCCI operation at compression ratio of only 4.5:1.

Removal of the castor oil increased the ignition quality of the fuel slightly which advanced the main heat release timing. Despite the significantly lower compression ratios allowed by the model-aero fuel (and the higher exhaust gas residuals associated with it), the noted trends for knock, speed and the stable air-fuel ratio limits were very similar to the other tested fuels. The conclusions from the tests were therefore as follows:

- D1000 did not show any unusual or particularly favourable HCCI combustion properties when compared to the other fuels
- The castor oil blending component did not significantly reduce heat release rates or in any other way significantly benefit HCCI combustion.
- Fig 11 shows D1000 exhibiting clear two-stage auto-ignition behaviour despite D1000 only showing single-stage auto-ignition in the model aero engine (which shall be described in the following section).

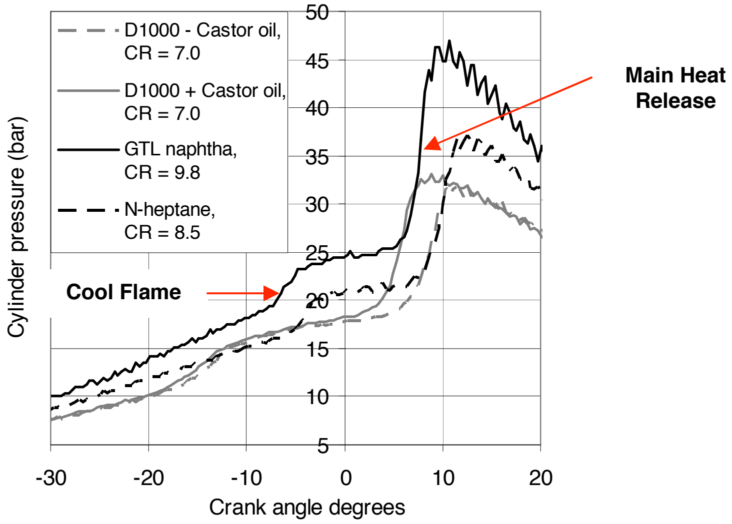

**Figure 11:** Pressure traces for the 4 test fuels at =2.5 (Incipient knocking conditions) indicating compression ratios required for indicated combustion phasing

### 4.1.3. Discussion of D1000 Fuel Testing

The IQT$^{TM}$ tests found D1000 to have an exceptionally high cetane rating which manifested itself as very advanced combustion phasing during engine testing in the E6. Testing the components of the fuel revealed isopropyl-nitrate to have an extremely high cetane number which made it a suitable "ignition improver".

It was reasoned that the castor oil in the fuel did not contribute significantly to the ignition quality of the fuel. It was noted that the castor oil was exhausted in the liquid phase and would significantly lower the performance of the engine as it would have to heat up the (relatively inert) castor oil without it contributing significantly to combustion heat release. The result was not surprising as castor oil was used primarily as a two-stroke lubricant.

While suitable for the model-aero engine, the D1000 fuel did not show any especially favourable HCCI characteristics.

# *5. ENGINE TESTING*

Controlled testing of the model-aero engine provided the most insight into the operating characteristics of the engine. The goals for testing were as follows:

- Define the operating range using the characterised propellers
- Investigate the limits of the operating range and which factors define these limits
- A general investigation of the engine's reaction to changes in operating conditions and physical setup (such as speed, load, CR, AFR etc.)
- Emissions measurement
- Investigate the engine's natural compensation for combustion phasing requirements at different points along the standard load profile
- Observe the effect (on combustion phasing) of changing speed at a constant load and then make similar observations based on changing load at a constant speed as a combination of these separate effects was thought to produce the engine's natural compensation for combustion phasing

## 5.1. EXPERIMENTAL RIG DESIGN AND PHILOSOPHY

By using the characterised propellers, it was possible to plot out the operational envelope of the engine and also analyse areas of irregular or undesirable combustion phenomena (i.e. knocking or misfiring). It was also possible to test the engine at specific load/speed points within the operational envelope provided those points lay along one of the load profile curves of the tested propellers. Testing the engine in this manner allowed for the investigation of the effects of different operating conditions on combustion characteristics.

The experimental rig (as inherited from a previous study) was originally fitted with an in-cylinder pressure transducer and a TDC marker (used to measure both engine speed and crank angle degrees). Due to the more extensive nature of this study, further instrumentation and modifications were required to understand factors known to influence HCCI operation as shown in Table 8. These test factors were limited to:

**Table 8:** Techniques used to measure factors which are known to influence HCCI operating [13, 27]

| Factor | Measuring Method |
|---|---|
| **In Cylinder conditions** | pressure transducer in cylinder |
| **Inlet Pressure** | pressure transducer in crank case |
| **Inlet Temperature** | thermocouple in crank case |
| **Air-Fuel Ratio** | lambda sensor in exhaust |
| **Compression Ratio** | measured geometrically |

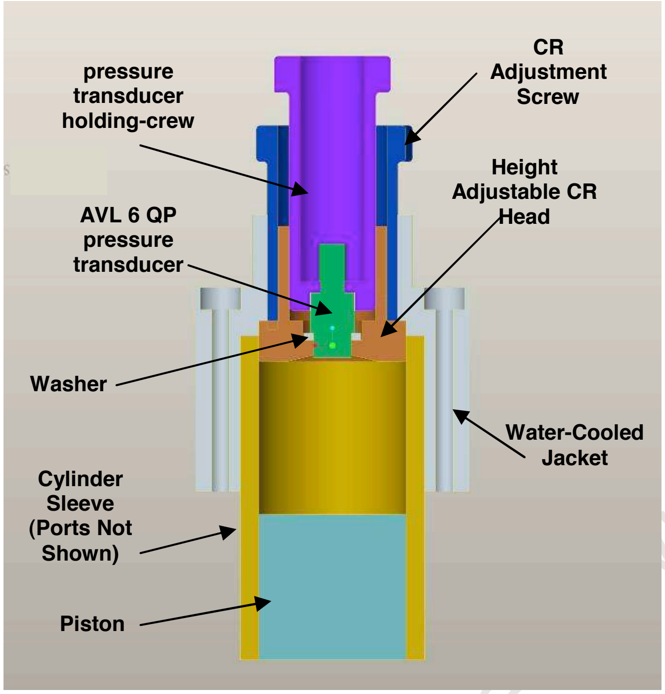

**Figure 12:** Engine Head and Cylinder Cross Section for use with AVL 6QP pressure transducer.

The engine was adjusted while running to achieve the maximum speed (and therefore power) for a given propeller. Table 9 shows the factors which were adjusted for maximum engine speed (and optimum phasing):

**Table 9:** Engine adjustments and effects

| **Adjustment** | **Intentional Control Effect** |
|---|---|
| **Throttle opening** | Air-Fuel Mixture Inducted, Exhaust Residuals |
| **Mixture Needle** | Air-Fuel Ratio |
| **CR screw** | Compression Ratio |

## 5.2. EXPERIMENTAL METHOD AND APPARATUS

Detailed engine testing required extensive instrumentation of the model-aero engine, but due to the engine's small size, not all instrumentation could be fitted to the engine at the same time.

The engine's air-cooled head was replaced by a water-cooled unit as shown in Figure 12 with temperature control to limit engine wear during prolonged testing and control the temperature conditions across different test conditions [28]. The water-cooled head was also used to cool the pressure transducer mounted in the cylinder head. The ability to vary the compression ratio was retained.

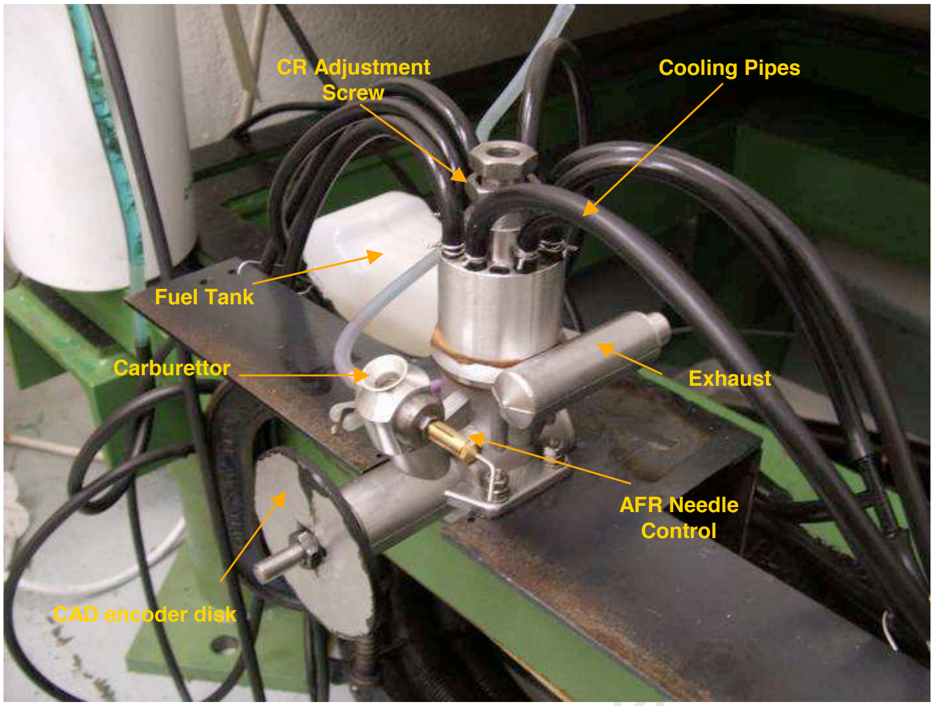

**Figure 13**: Un-Instrumented Model-Aero Engine

The engine was later modified such that a water-cooled pressure transducer or thermocouple could be placed inside the crank case. The motivation was that the pressure trace from the crank-case pressure and average temperature from the thermocouple could be used as an inlet port boundary condition in the Computational Fluid Dynamics (CFD) model of the engine. Readings from the absolute pressure transducer in the crank-case were also used as a means of calibrating the readings from the relative pressure transducer in the cylinder.

In order to improve the correlation between experimental and computational results a pressure transducer was placed in the wall of the exhaust silencer. Measurements of the exhaust back-pressure were used as boundary conditions to initialise the CFD simulation and as a means of improving the simulation's estimation of exhaust residual fractions.

After initial testing it became clear that relative air-fuel ratio measurements (as estimated by carburettor mixture needle setting) was not suitable for a detailed analysis of the engine. As a result, a lambda sensor was fitted into the exhaust stream. This posed a problem due to the liquid castor oil entrained in the exhaust stream. Therefore an oil trap was incorporated into the exhaust manifold as prolonged exposure to the liquid castor oil would have caused blockage of the porous ceramic coating on the electrode surface of the lambda sensor and subsequent failure of the sensor.

A filter system for the liquid castor oil in the exhaust would have compromised the exhaust scavenging system with too much back-pressure. A momentum/gravity-type trap was employed to avoid the back-pressure issue. Figure 14 shows a schematic of the design and Figure 15 shows a graphic rendering.

Despite the free-flowing nature of the castor oil trap, a small drop in performance was noticed with the new exhaust system fitted. A later modification also added an exhaust gas sampling probe next to the lambda sensor for emissions measurement (despite the high levels of condensation in the non-heated trap which would have an effect on the measured concentrations of soluble gasses).

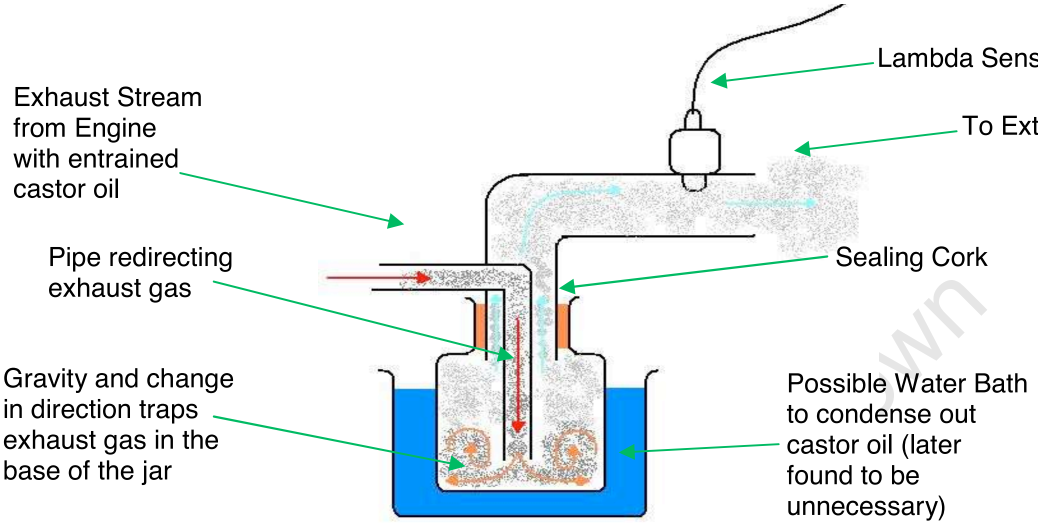

**Figure 14**: Schematic sketch of castor oil trap

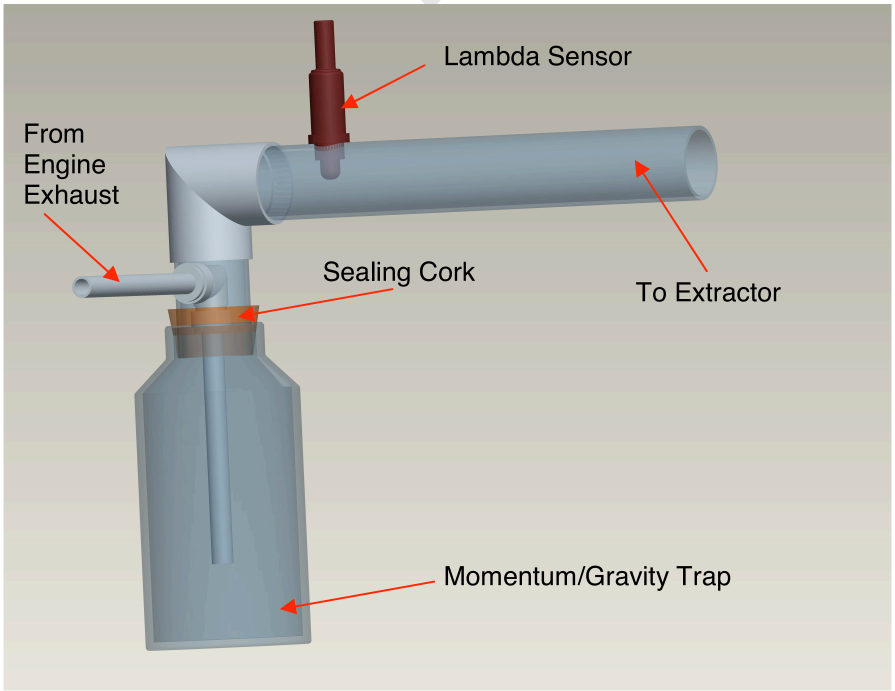

**Figure 15**: Graphic Rendering of castor oil trap design

A thermocouple was fitted next to one of exhaust ports of the engine to measure the exhaust gas temperature. In addition, a thermocouple probe could be placed in the head instead of the pressure transducer as a means of gaining insight into the average head temperature trends. These were also used as boundary conditions for CFD and as an input variable for modelling heat-loss in the combustion modelling.

Fuel was supplied using a conventional gravity feed model-aero fuel tank. The fuel was refilled to approximately the same level prior to each test as significant variations in the fuel level had a measurable effect on AFR as noted during some extended steady-state testing. The needle-type air-fuel ratio mixture control was retained along with the original barrel-type throttle valve.

A hand-operated electric model-aero starter motor was used to start the engine as well as to spin the engine while recording motored cylinder pressure-traces.

All maximum speed points were operated with the throttle wide open. Minimum speed points utilised whichever throttle and mixture combinations optimised stability at the compression ratio being tested. Intermediate points utilised whichever settings were required by each specific test.

Progressive evolution of the rig meant that particular features were only added as the need arose. In addition, the engine or test rig required repair at some stages. Testing was therefore split up into six distinct “batches” with the rig having the following instrumentation and configuration for each batch:

Batch 1:
- Rig in original condition with no added instrumentation
- pressure transducer in cylinder head
- CAD TDC encoder

Batch 2:
- No added instrumentation
- Different position for TDC marker (to improve TDC estimation)

Batch 3:
- New cylinder sleeve (due to scoring marks found inside the sleeve)
- New Piston with honed skirts (due to scoring marks on the piston skirts)
- Different type of pressure transducer in cylinder head (previous PT failed)
- New cylinder head for new PT with same combustion chamber geometry
- castor oil Trap added to exhaust
- Lambda sensor in exhaust stream
- Different position for TDC marker (due to full engine disassembly)

Batch 4:

- New thermocouple in cylinder head
- New cylinder head for thermocouple with same combustion chamber geometry
- Thermocouple placed in exhaust stream
- Thermocouple placed in crank case
- pressure transducer placed in crank case

Batch 5:

- Exhaust gas sampling probe placed in exhaust stream
- Carburettor modified to allow for leaner operation

Batch 6:

- pressure transducer placed in exhaust silencer

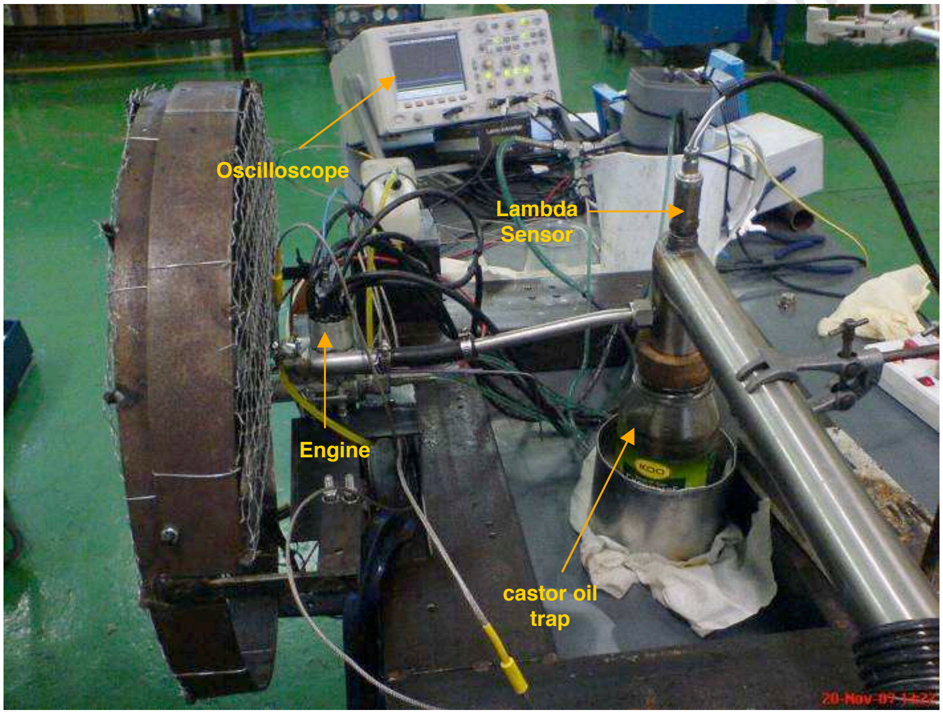

**Figure 16:** Model-Aero engine test rig (Batch 4 set up)

Note that the propeller is hidden from view in the above image by a protective safety-cover.

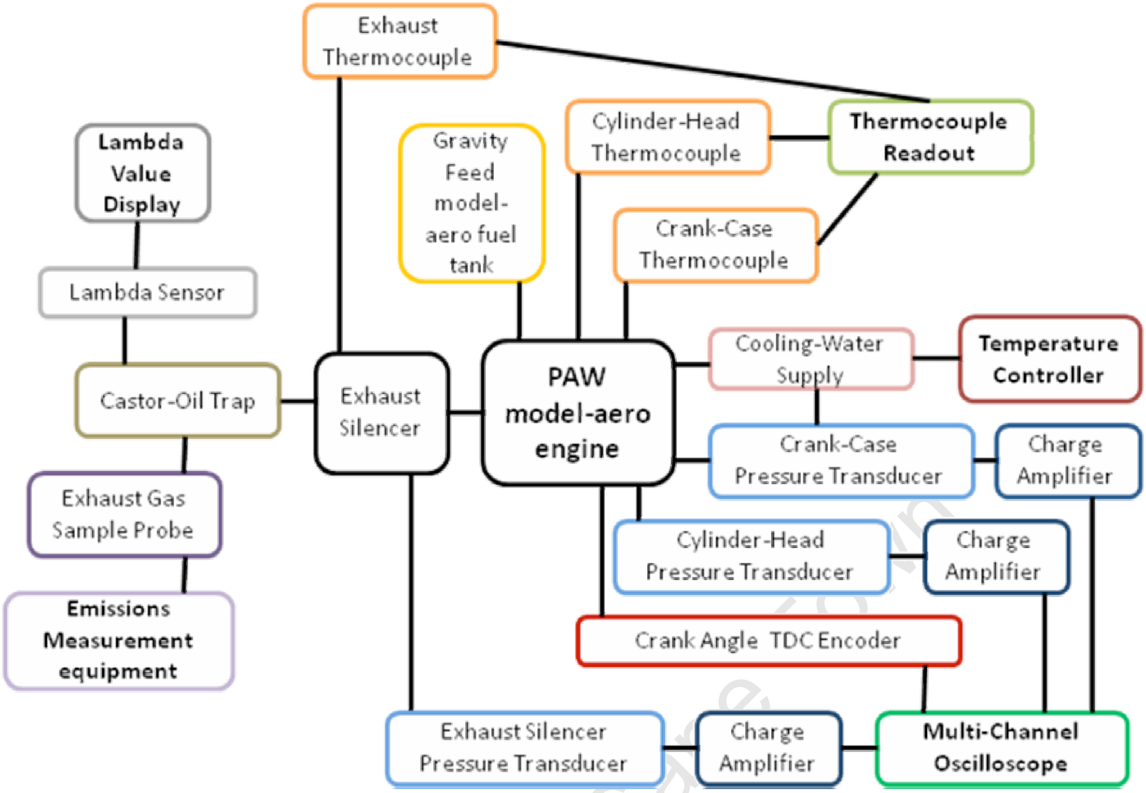

**Figure 17**: Conceptual Layout of Engine Test rig

In Figure 18 below note the valve timing. Note also that although there may appear to be cool flame combustion near TDC, analysis of the heat release data showed no such event. This peak just before TDC is due to compression with the location attributed to significant heat loss in the small model aero engine.

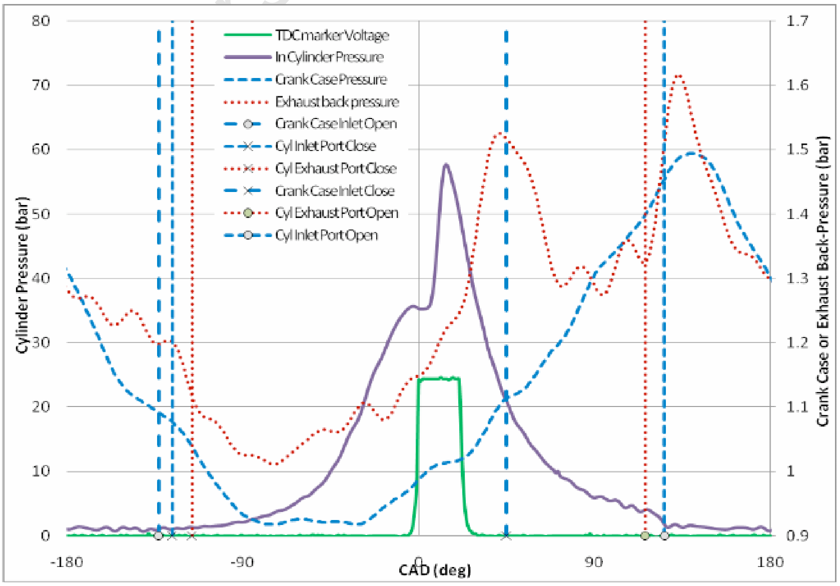

**Figure 18**: Illustration of data captured from the Oscilloscope while running the engine with the 12x6 propeller at 8596rpm

## 5.3. EXPERIMENT RESULTS AND ANALYSIS TECHNIQUES

### 5.3.1. TDC Marker and Correction

The TDC marker could only be used to estimate the true position of TDC and also required repositioning every time the engine was dismantled. Placement of the marker relied on visual inspection, but accurate analysis of Pressure Trace data required more accurate positioning of TDC than was possible by visual inspection. Incorrect positioning of TDC can result in significant errors in heat release analysis, work calculations and instantaneous volume calculation. As a result, computational TDC correction was applied to the TDC marker signal. The method of TDC correction utilised the polytropic compression relationship where:

$PV^k$ = constant (where k is the ratio of specific heats) (Equation 2)

It follows that:

$$k = \frac{\log\left(\frac{P_1}{P_2}\right)}{\log\left(\frac{V_2}{V_1}\right)} \quad \text{(Equation 3)}$$

Plotting k versus CAD for a motored trace should show asymptotic behaviour about TDC if the position of TDC is correct. If one analysed a plot of k vs. CAD without applying TDC correction then the position of the asymptote will be incorrectly positioned if TDC has been positioned incorrectly. Employing this technique, it was possible to shift the estimated TDC position to the true TDC position by matching the asymptote to the true TDC [29].

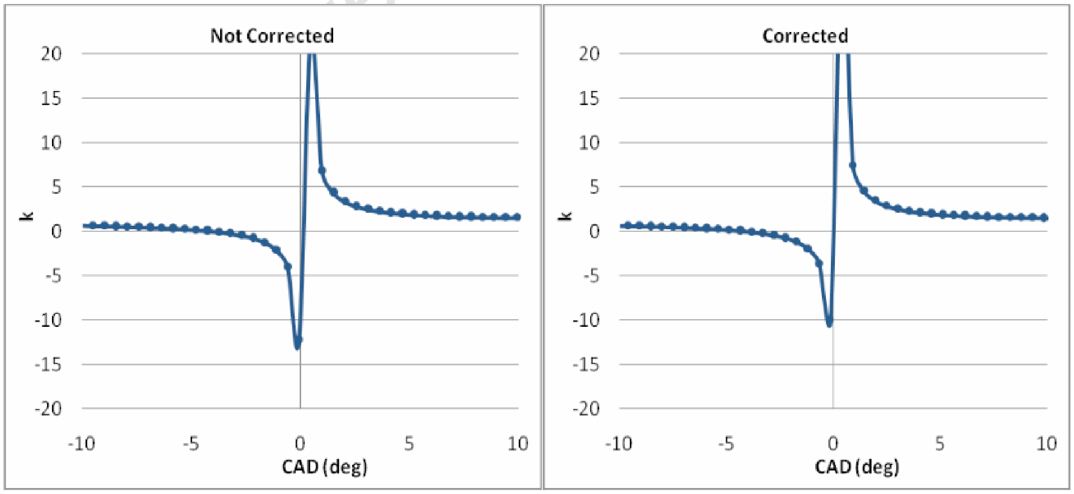

**Figure 19**: Plot of k (from smoothed P-trace sections) vs CAD shows the position of the asimptote change as TDC is offset

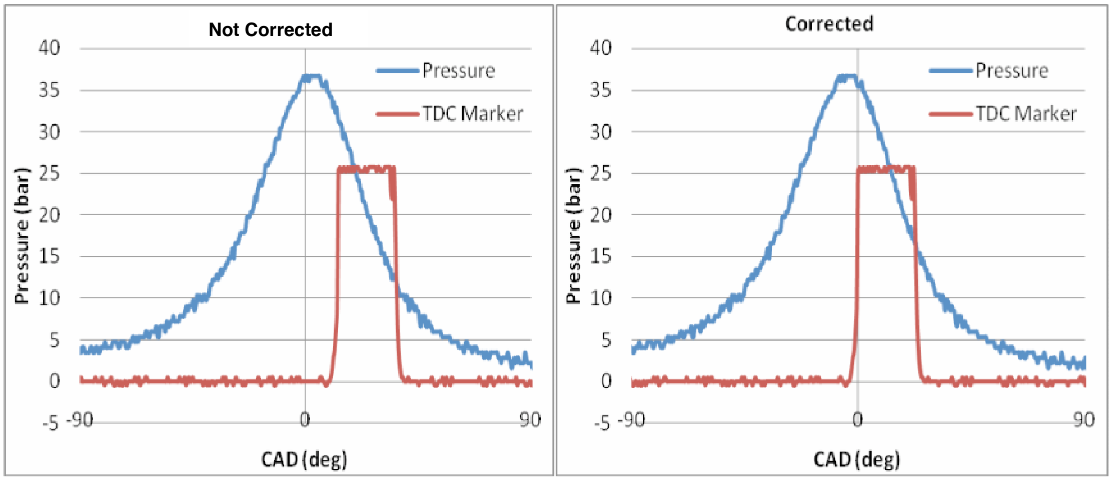

**Figure 20**: Plots of the (un-smoothed) motored pressure traces and TDC marker signal before and after correction (12x6 propeller with 14.8 CR at 4380rpm)

The closer the initial estimate the more effective the correction as changes in rotational velocity near TDC (deceleration due to compression and then acceleration due to expansion) cause changes in the step-size time-duration. For example, attempting to correct a misplacement of 40 CAD will yield errors on the magnitude of a few degrees for what appears to be the corrected position.

### 5.3.2. Operating Range and Limits

Careful adjustment of the throttle, mixture and compression ratio resulted in a much larger operating range than could be achieved using only the recommended propellers and the full operating range is shown in Figure 21. Within this area there was no evidence of knocking (at any of the high-load points) or misfiring (at any of the low-load points). High-load points were easily identified as the maximum speed for a given propeller.

Low-load points were harder to identify as the engine continued to run smoothly even when misfiring badly. Due to low-magnitude heat release (and subsequent pressure rise) at low load, combustion was difficult to identify on the oscilloscope even though three or more cycles were displayed at a time. Even though the engine could run at a slower speed with misfiring cycles, the low-load points were characterised by no misfiring cycles shown on the oscilloscope as a visible combustion pressure rise for all the displayed cycles. Allowing misfiring cycles as part of the acceptable operating criteria would have expanded the lower-end of the operating range significantly.

Exploratory testing showed that using just three propellers provided a suitably large operating range for the engine. The 11x5 propeller was chosen for low-load, high speed operation. The 12x6 propeller represented the normal load-speed profile for the engine and the 15x10 propeller was chosen for its high-load, low-speed characteristics.

In the image below showing the test points superimposed on the speed-load curves of the tested propellers; the discrepancy between the speed-load curves and the test points is due to the speed-load curves being calculated using a constant air density whereas the test points were calculated using the actual air density for each test. A full table of all the test points can be found in Appendix 4.

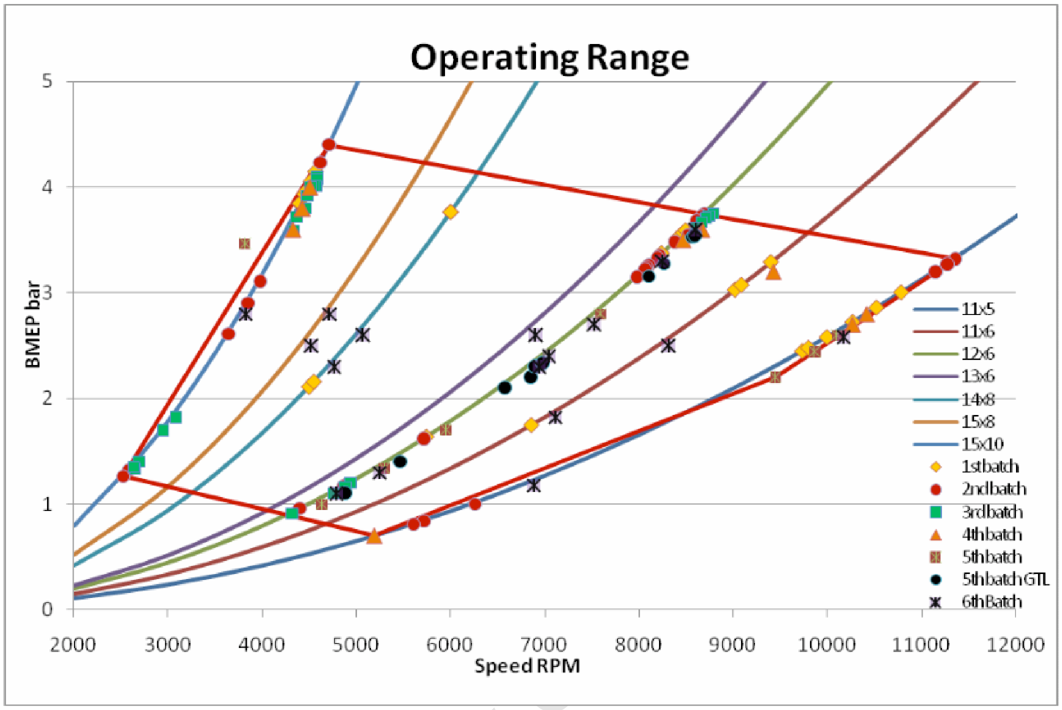

**Figure 21:** Full model-aero operating range

The following pages first show the data for maximum speed points and then the data for the minimum-speed points.

Maximum Speed Limits:

**Table 10**: The maximum operating speeds for the tested propellers and the associated operating conditions

| Prop | RPM | BMEP bar | CR | Lambda | T amb °C |
|---|---|---|---|---|---|
| **15x10** | 4706 | 4.4 | 9.2 | ~1.4 | 17 |
| **12x6** | 8797 | 3.8 | 14.8 | 1 | 20 |
| **11x5** | 11363 | 3.3 | 17 | ~0.95 | 16 |

The following graph in figure 22 shows the pressure traces for the points described above – note the similar phasing. Similarly, table 11 shows the combustion behaviour for the maximum speed points.

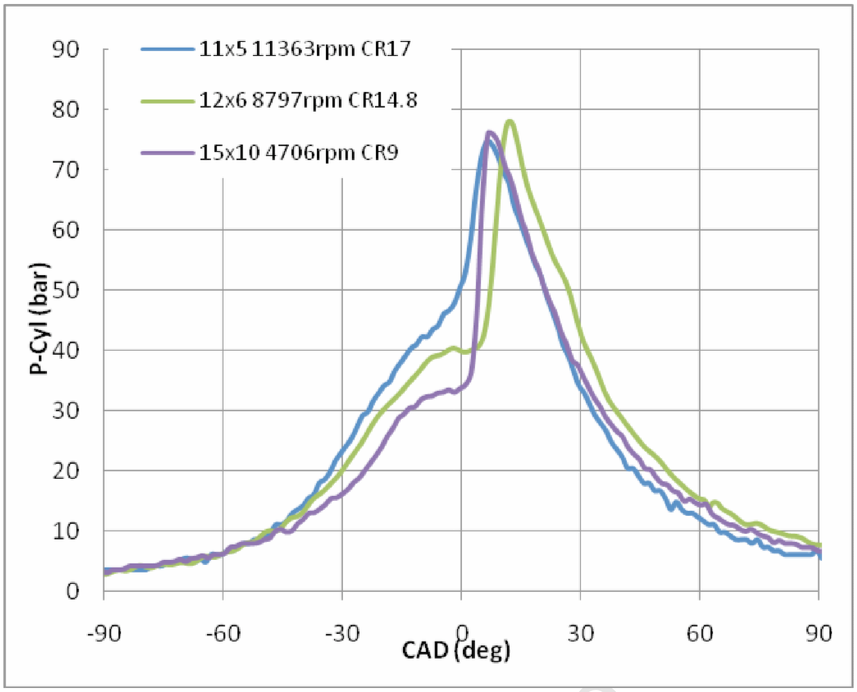

**Figure 22:** Overlay pressure traces of the maximum speed points for each propeller.

**Table 11:** Combustion behaviour at the maximum-speed limits of the model-aero engine. Note the conservative maximum pressure rise rates (PRR)

| **Combustion Behaviour** | | | | | | | | | |
|---|---|---|---|---|---|---|---|---|---|
| **Prop** | **Speed** | **CR** | **Lambda** | **MFB (SOC)** 1% | **MFB (burn duration)** 10-90% | **Max PRR** bar/deg | **@CAD** deg | **Pmax** bar | **@CAD** deg |
| **11x5** | 11363 | 17 | ~0.95 | -2 | 7.3 | 5.1 | 3.5 | 74.8 | 6.2 |
| **12x6** | 8797 | 14.8 | 1 | 2.5 | 7 | 8.1 | 9.4 | 78 | 11.5 |
| **15x10** | 4706 | 9.2 | ~1.4 | 1 | 4.3 | 12 | 5 | 76 | 6.4 |

The following graph in figure 23 shows the pressure traces for the points described above. Similarly, table 12 shows the combustion behaviour for the maximum speed points.

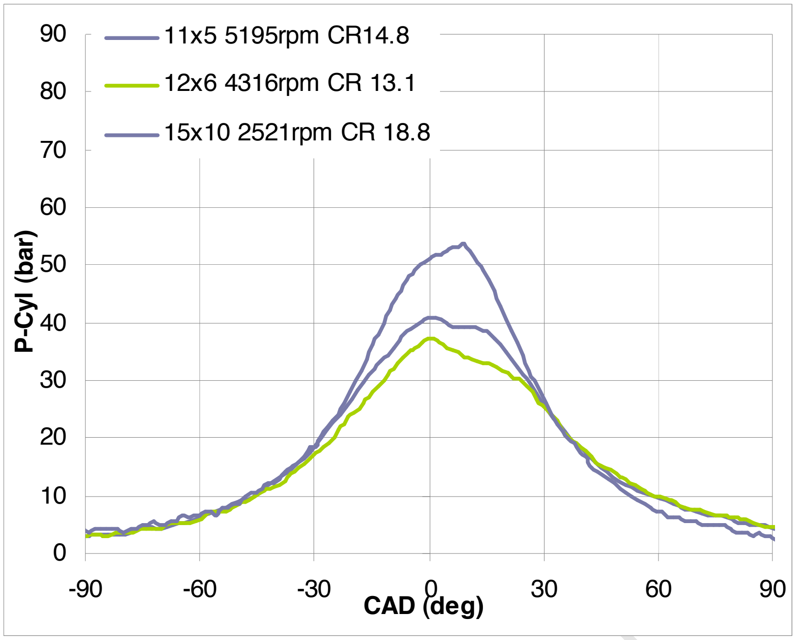

**Figure 23**: Overlay Pressure Traces of minimum-speed operating points

**Table 12**: The minimum operating speeds for the tested propellers and the associated operating condition

| **Combustion Behaviour** | | | | | | | |
|---|---|---|---|---|---|---|---|
| **Prop** | **RPM** | **BMEP (bar)** | **CR** | **Lambda** | **T amb °C** | **MFB 1%** | **MFB 10-90%** |
| **15x10** | 2521 | 1.3 | 18.8 | ~0.93 | 17 | 0 | 20 |
| **12x6** | 4316 | 0.9 | 13.1 | 0.98 | 20 | 5 | 20.3 |
| **11x5** | 5195 | 0.7 | 14.8 | 1 | 22.5 | 5 | 21.2 |

Testing the engine in the manner required for determining the operating range meant it was difficult to isolate the factors which most affected the combustion behaviour of the model-aero engine (as numerous factors were varied simultaneously to try and achieve the optimum engine setup).

Analysis of the pressure traces showed the maximum pressure rise rates and maximum pressures at the upper operating extremes were relatively conservative [14] and did not result in knock. The pressure rise rates due to combustion at lower operating extremes were even lower than the pressure rise rate due to compression.

A notable characteristic of all the maximum-speed operating points is that they showed similar phasing for the start-of-combustion, $P_{max}$ and burn duration. This suggests that the optimum engine setup at those points required a configuration which took full advantage of the combustion characteristics of the fuel. A similar trend was also noted for the low-speed operating limits.

### 5.3.3. Heat Release and Mass-Fraction Burned (MFB) analysis

The rate of heat release (HRR) and mass-fraction burned (MFB) were calculated in the following manner: [30]

HRR:

$$\frac{dQ}{dt} = \frac{\gamma}{\gamma - 1} P \frac{dV}{dt} + \frac{1}{\gamma - 1} V \frac{dP}{dt} \qquad \text{(Equation 4)}$$

A constant value of 1.33 was used as an approximation of $\gamma$ (the ratio of specific heats) during combustion [30].

MFB:

The mass-fraction burned was related directly to the combustion heat release. The MFB was calculated as a cumulative fraction of the total heat release.

$$MFB = \frac{\sum_{0toCAD} Q}{\sum_{total} Q} \qquad \text{(Equation 5)}$$

Analysis of the heat release data obtained from the pressure traces was difficult due to significant noise even after Fourier Transform smoothing. Despite the noisy signal it appeared as if there was no significant cool flame reaction at any of the test points. Two examples of the heat release data at the limits of the operating range of the engine are shown in Figure 24 and Figure 25. The signal noise was attributed to heat flux in the pressure transducer as it was not directly water-cooled. Engine vibration could also have contributed to the noisy signal. Note the large amount of signal noise in the image below:

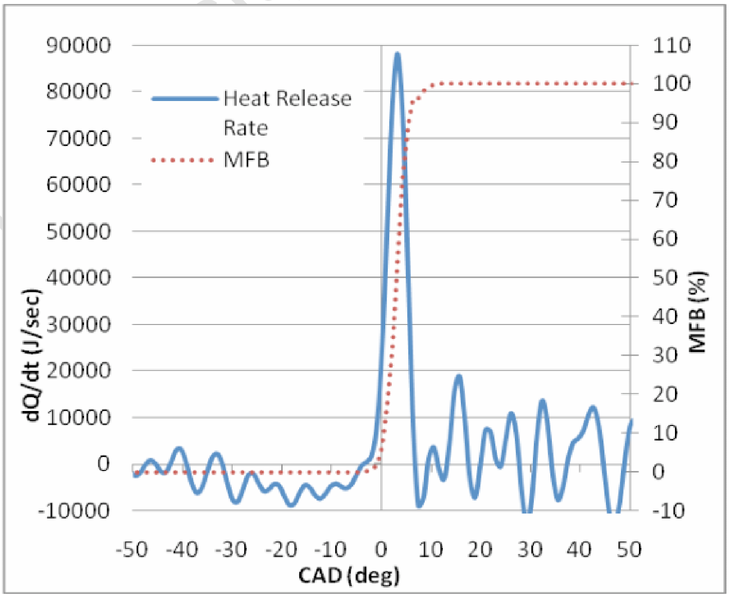

**Figure 24:** Example of maximum power heat release with no cool flame component (12x6 prop at 8646rpm).

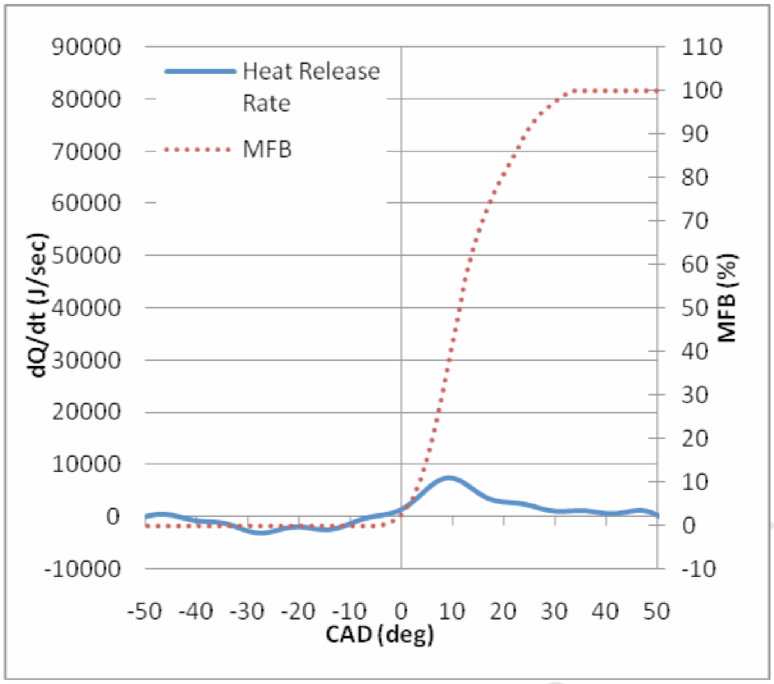

**Figure 25:** Example of minimum stable speed heat release example with no cool flame (12x6 prop at 4898rpm). Shown on the same scale as maximum speed point above in Figure 24

## 5.4. GENERAL INVESTIGATION

This investigation sought to determine the general behaviour of the engine to changes in operating parameters such as compression ratio, speed, load and air-fuel ratio. Of specific interest were the combustion phasing and the resultant performance of the engine. What follows are examples of the trends observed during this investigation.

Figure 26 shows the speed effect on combustion phasing which was advanced as speed was decreased for the maximum speed points using different propellers and a fixed compression ratio of ~17:1.

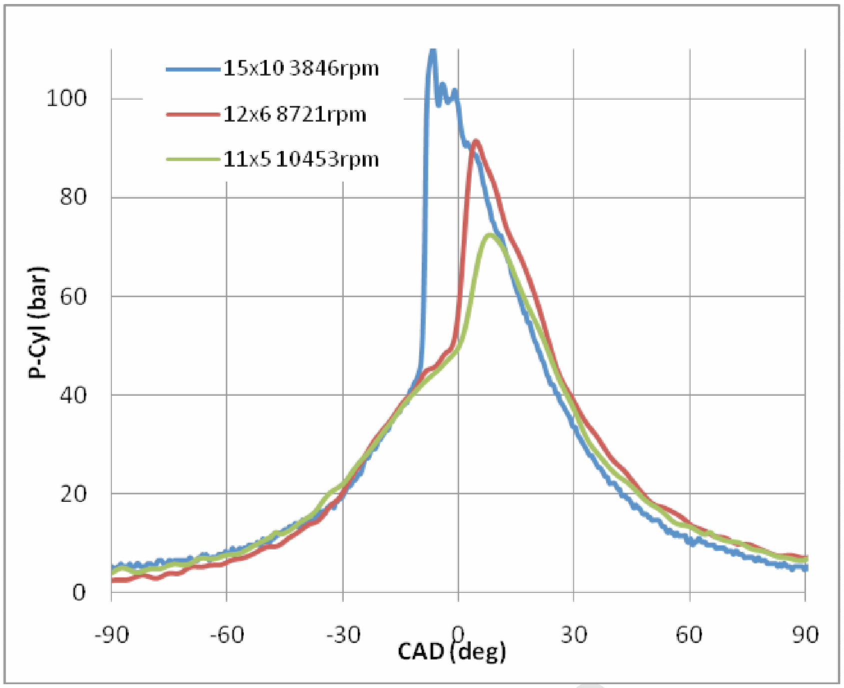

**Figure 26**: Overlay pressure traces of the maximum speeds achieved using a CR of 17 on the various propellers.

Combustion phasing was advanced as speed decreased (to the point of knocking on the 15x10 propeller). Note: The “spikes” near the peak of the 15x10 trace do not resemble regular high pressure oscillations (indicating knock) due to the resolution of the captured pressure trace (typically 1000 points will cover ~3 traces or more and over 1200CAD to ensure the analysis of representative traces).

Table 13 and Figure 27 are examples of the effect of varying the compression ratio while keeping the speed, throttle and mixture relatively constant. With increasing CR; one would expect the burn duration (10-90% MFB) to decrease, SOC (1% MFB) to advance and max PRR to increase.

**Table 13:** CR Effect on Combustion using 12x6 Prop

| **CR** | **RPM** | | **MFB** | **MFB** | **Max PRR** | **at CAD** |
|---|---|---|---|---|---|---|
| | | | 1% | 10-90% | bar/deg | deg |
| **17.3** | 8670 | ~1 | -1.5 | 5 | 9 | 2.8 |
| **13.3** | 8620 | ~1 | 1 | 6.1 | 5.3 | 6.2 |
| **10.8** | 8522 | ~1 | 2.5 | 7.3 | 4.2 | 11 |

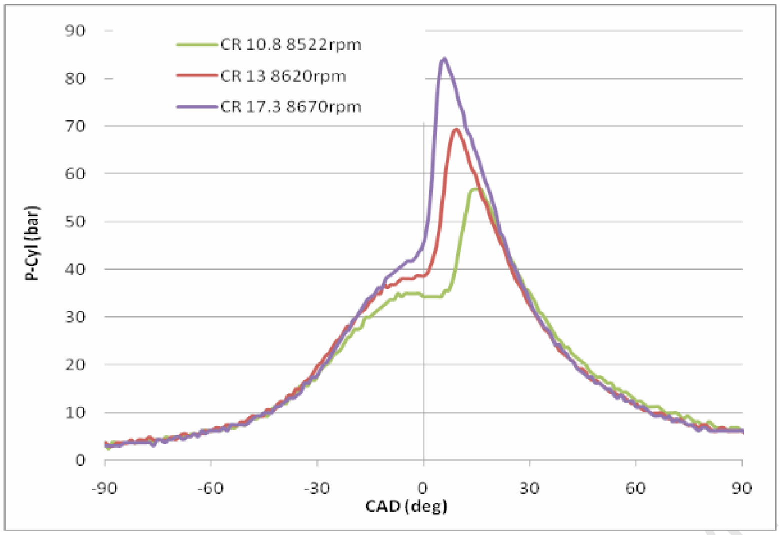

**Figure 27:** Overlay pressure traces of varying CR effects using the 12x6 propeller

Investigating the operating range using a fixed CR (in this case 15:1) showed the upper-speed limits of the operating range were significantly reduced as shown in Figure 28. The effect on the lower speed limits of the operating range was negligible. The 15x10 propeller was limited by undesirable knock due to the higher than optimum compression ratio. Better performance could be achieved by using a lower CR for the same air-fuel ratio and throttle setting. A CR of 15:1 was practically identical to optimum setting for the 12x6 propeller and therefore no loss in performance was detected. The 11x5 propeller showed the opposite behaviour to the 15x10 propeller and ran better with a higher compression ratio than the test conditions as a higher compression ratio would have better matched the phasing required by higher speeds. The new upper limits of the operating-range are shown superimposed onto the full operating range below:

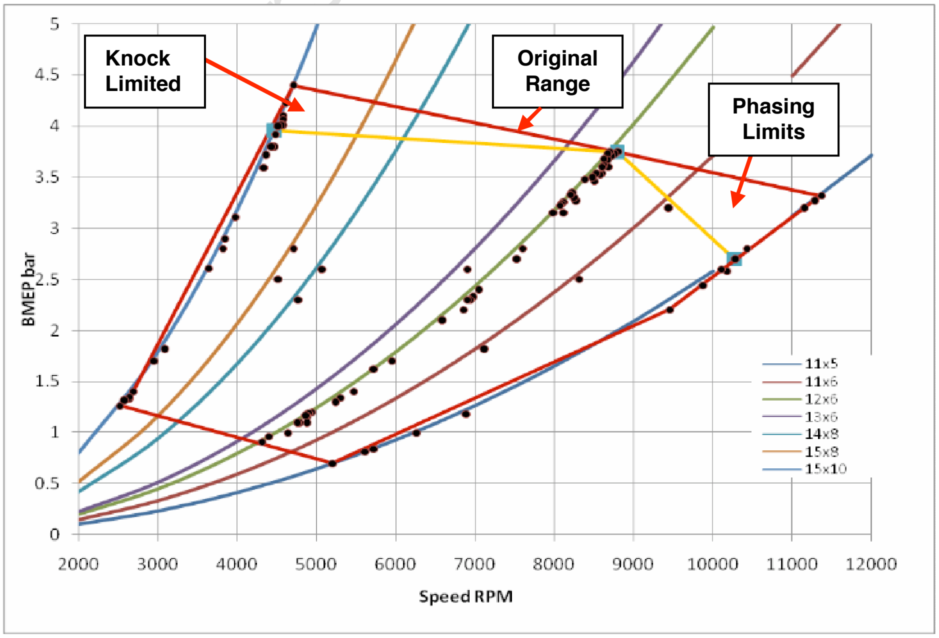

**Figure 28:** Effect on operating range of using a fixed compression ratio of 15:1

It was found that the engine could be made to knock under certain conditions. Unlike any of the other tested propellers, the 15x10 and 15x8 propellers could not run with the throttle wide open (WOT) at the same engine settings used for low speed operation. The higher compression ratios required for optimum low speed operation on the 15x10 propeller caused knock when the throttle was opened from low speed. This was the reason the engine required a much lower compression ratio at maximum power using the 15x10 propeller than at low loads.

In the most severe case of over advanced timing (15x10 prop, 3845 rpm at CR=17.3) the maximum pressure rise rate reached approximately 44bar/deg while 10-90% MFB was completed in approximately 2.6CAD.

The knock manifested as high pressure oscillations on the pressure trace and also as an audible noise (which was not present at other operating conditions). Despite the negative effect on performance, the engine ran without misfire while knocking and with no noticeable engine damage.

In figure 29 below, note the highly advanced timing and high pressure rise rate. Note also that this particular trace was captured on the oscilloscope using an increased resolution equivalent to 1000 sample points for ~300 CAD. This was not suitable for regular data-capture which required two or more traces to calculate engine speed and ensure a representative data sample.

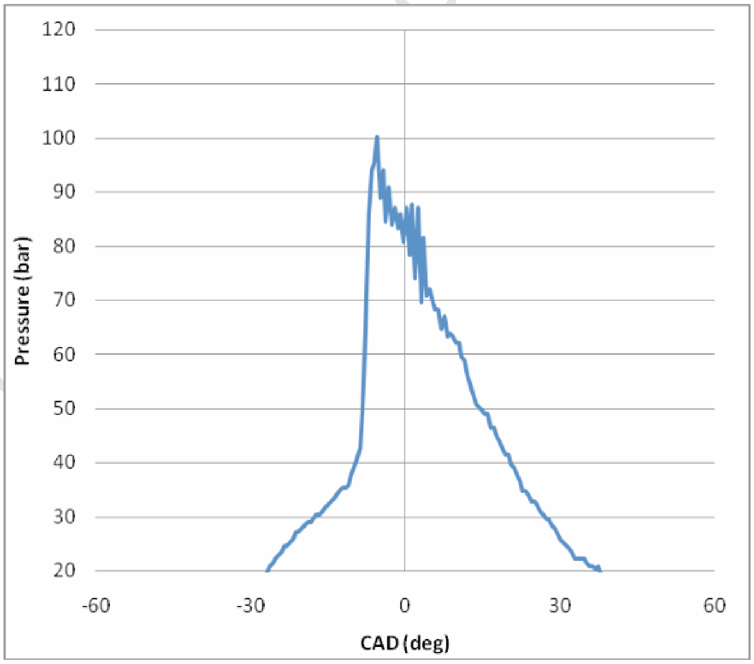

**Figure 29:** Pressure trace showing knock-related high pressure oscillations using the 15x8 propeller and a compression ratio of 12.3.

Below is a table describing the operating conditions associated with the knocking pressure trace in figure 29.

| **Severe Knocking Conditions** | |
|---|---|
| **Propeller** | 15x8 |
| **Compression Ratio** | 12.3 |
| **Lambda** | 0.9 |
| **Ambient Temperature** | 25 $^{o}$C |
| **Speed** | 4706 rpm |
| **Maximum PRR** | 16.4 bar/deg |
| **at CAD** | -8 deg |
| **Maximum Pressure** | 97 bar |
| **at CAD** | -5 deg |
| **Burn Duration 10-90% MFB** | ~5deg |
| **1% MFB** | -11 deg |

**Table 14:** Operating Conditions for knocking pressure trace.

## 5.5. EMISSIONS MEASUREMENT

The exhaust gas emissions (after the castor oil trap) were measured using Horiba emissions equipment (specifications to be found in appendix 5). The hydrocarbon (HC or THC) and $NO_x$ emissions for the model aero-engine were expected to be high considering the engine operated on a two-stroke cycle and used a nitrate-based additive. Two-stroke engines pass some unburned fuel into the exhaust due to short-circuiting of the fresh charge which causes high HC emissions. Nitrate-based fuel additives increase nitrous-oxide emissions due to increased amount of nitrogen available to synthesize nitrogen compounds during the high-temperature combustion reactions.
The HC emissions were shown to be close to or over the measurable limit (~50 000ppmC) of the testing equipment.

It was planned to test the full range of emissions for the engine at the maximum power points of each propeller and then do a comparative test between LTFT GTL-based fuel blends and D1000 using the standard propeller.

Unfortunately this plan was abandoned after tests showed that it was not possible to measure THC emissions as they were beyond the measurable limit of the test equipment. In addition, it was not possible to lean out the mixture to stoichiometric (or lean) conditions for the GTL-based fuels (GTL-A and GTL-B in the table below) due to the adjustment limits of the carburettor. Below is a table showing the preliminary tests:

**Table 15**: Exploratory emissions test results using the 12x6 propeller

| | | | | | **EMISSIONS** | | | | |
|---|---|---|---|---|---|---|---|---|---|
| **Speed** | | **CR** | **Fuel** | **Lam** | **CO** | **CO2** | **O2** | **NOx** | **THC** |
| | | | | | Vol% | Vol% | Vol% | ppmC | ppm |
| max | 8500 | 15 | D1000 | 1 | 2.2 | 9.1 | 6.7 | 830 | ~50000 |
| max | 8600 | 15 | GTL-A | 0.9 | 5.5 | 15 | 5.0 | 290 | >50000 |
| max | 8570 | 15 | GTL-B | 0.85 | 11.3 | 4.0 | 4.3 | 209 | >50000 |

## 5.6. COMBUSTION PHASING ALONG THE NORMAL LOAD-SPEED PROFILE (12X6 PROPELLER)

During engine testing it was noted that the engine displayed approximately constant phasing as the throttle was closed from maximum speed for a given propeller. As explained earlier, closing the throttle lowers the speed (advances timing), decreases fuelling (and hence, load which retards timing) and increases exhaust residuals (which retards timing). It should be noted that increased exhaust-residuals can shorten burn duration and combustion delay by increasing the in-cylinder temperature, but it can also increase burn duration by lowering the concentration of fresh charge inducted into the cylinder.

It was suspected that the engine possessed some natural compensation to control what would otherwise be changing combustion phasing which allowed it to operate comfortably at various loads and speeds using a fixed engine configuration – a characteristic not usually associated with classic HCCI engines. With the engine optimised for maximum power using a given propeller it was possible to lower the speed (and hence load) of the engine by closing the throttle. This investigation sought to ascertain whether the engine showed natural compensation and which factors (due to throttle-position) dominated the combustion phasing.

The engine was first set up for maximum speed on the 12x6 propeller and then the throttle was closed progressively (while adjusting the mixture for constant AFR and also keeping CR constant) until the stable speed was reached at each point.

Below are the operating points superimposed onto the load profile of the 12x6 propeller as shown below in figure 30. Each point varied load, speed and throttle position while keeping CR and AFR (nominally) constant.

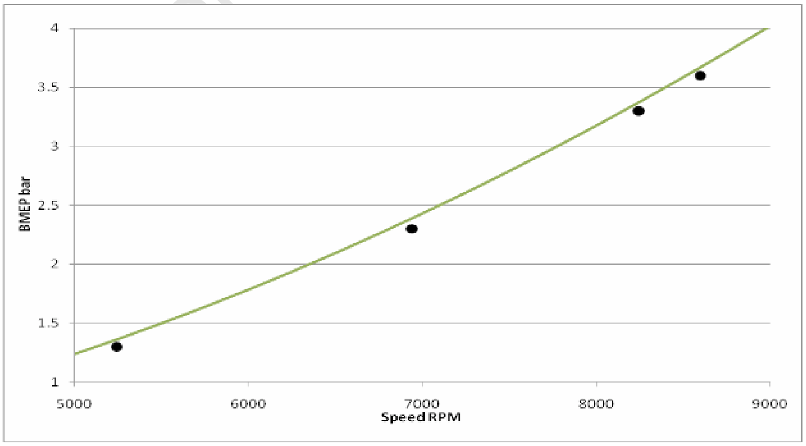

**Figure 30**: Test points along 12x6 speed-load profile. The speed-load profile was calculated at a different air density to the engine tests causing the apparent misalignment.

In Figure 31 below, note the very similar combustion phasing. It was not clear why the slightly slower point, 8242 rpm, should showed slightly more advanced timing than the 8596rpm point as the 8596 rpm point required a marginally wider throttle opening.

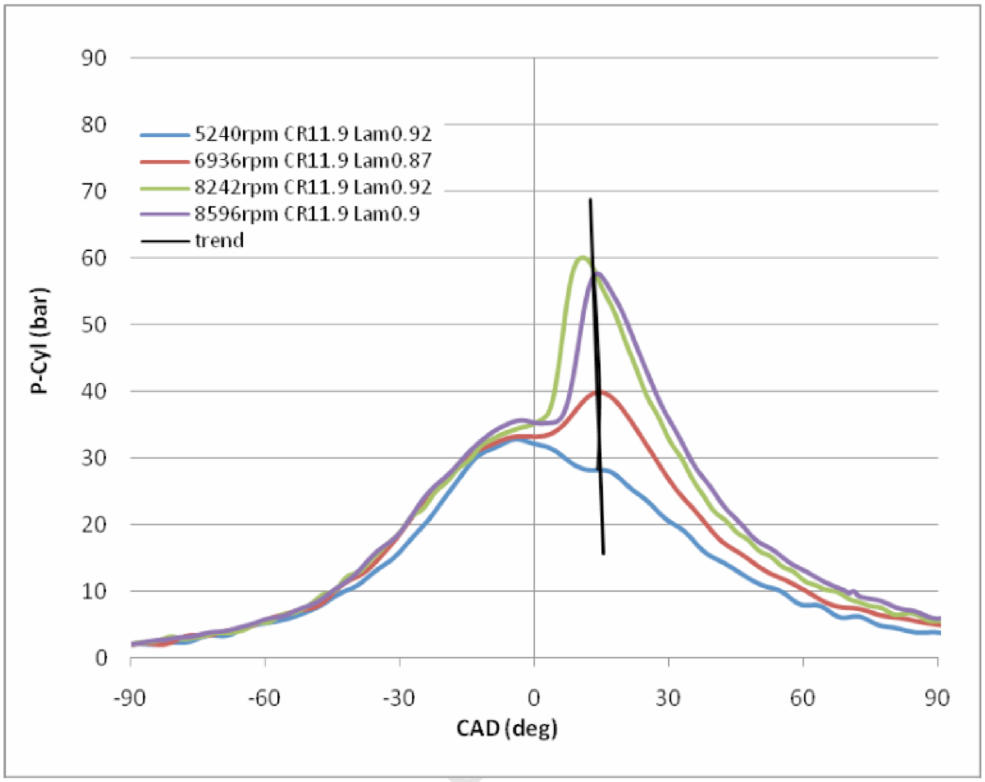

**Figure 31:** Overlay pressure traces of points along standard load-profile.

Note that the slowest-speed point achieved such late, low-magnitude heat release (due to highly throttled operation) resulting in peak pressure near TDC and not during combustion. The value provided for pressure peak in its case is due to combustion and does occur at a similar CAD when compared to the other test points.

**Table 16**: Combustion Characteristics of points along standard load-profile

| Speed rpm | BMEP bar | Lambda | Combustion Pmax Bar | at CAD deg | 10-90% MFB (burn duration) Deg |
|---|---|---|---|---|---|
| 5240 | 1.3 | 0.92 | 28.3 | 14 | 19.2 |
| 6936 | 2.3 | 0.87 | 40 | 14.5 | 14.3 |
| 8242 | 3.3 | 0.92 | 66.7 | 8.2 | 6.7 |
| 8596 | 3.6 | 0.9 | 57.6 | 13.4 | 8.3 |

By observing the combustion phasing it appeared as if the engine possessed some natural compensation for maintaining optimal combustion phasing. Although the AFR was kept constant during the investigation is was found that the engine actually ran smoother without any adjustment from the point of maximum power.

Classic HCCI engines (as described in Section 2.2) struggle with low load operation due to the low temperatures conditions which retard combustion phasing. In the PAW engine, load is decreased by throttling the engine and it was found that the AFR leaned out as the throttle closed (if one did not adjust the AFR needle).

Exhaust temperature measurements during engine-testing consistently showed that temperature increased as the AFR was leaned out (as occurred when throttling the engine). This suggests that the engine uses AFR adjustment when throttling to keep enough heat in the trapped residuals to achieve appropriate phasing (by opposing the effect of low-load, low-temperature conditions). This characteristic suggests the carburettor was correctly tuned to provide good transient operation and a wide operating range for a fixed (but correctly tuned) engine setup.

## 5.7. COMBUSTION PHASING AT CONSTANT LOAD AND THEN AT CONSTANT SPEED

Isolating the effects of varying speed and separately varying load required two separate sets of tests.

In the first test, the load was kept approximately constant while the speed was varied. This was accomplished by running the engine at specific speed points along the calibrated propellers. Each of these points corresponded to a similar load, but due to the different propellers, each point required a different speed (achieved by varying throttle position while independently adjusting the mixture to achieve constant AFR). In this manner it was possible to isolate the load and observe the speed-effect on combustion phasing (or factors affecting combustion phasing as exhaust residuals were also thought to vary with varying throttle positions).

In the second test, speed was kept constant while load was varied (as each propeller would have a different load for the same speed). This was accomplished in a similar manner to the previous tests by running the engine on different propellers, but this time at the same speed. It was therefore possible to isolate the speed-effect and observe only the effect of load (achieved by varying throttle position while independently adjusting the mixture to achieve constant AFR) on combustion phasing.

Both tests were carried out using a variety of propellers with a constant CR of 12.3:1.

Figure 32 illustrates the tests using various propellers at specific operating points to achieve constant speed and constant load operation.

It should be noted that while it was theoretically possible to pass through six points of constant speed at approximately 4750rpm, this was found to be extremely difficult in practice considering that two points sat at the extremes of the operating range and required different air-fuel ratios and compression ratios than the setup being tested.

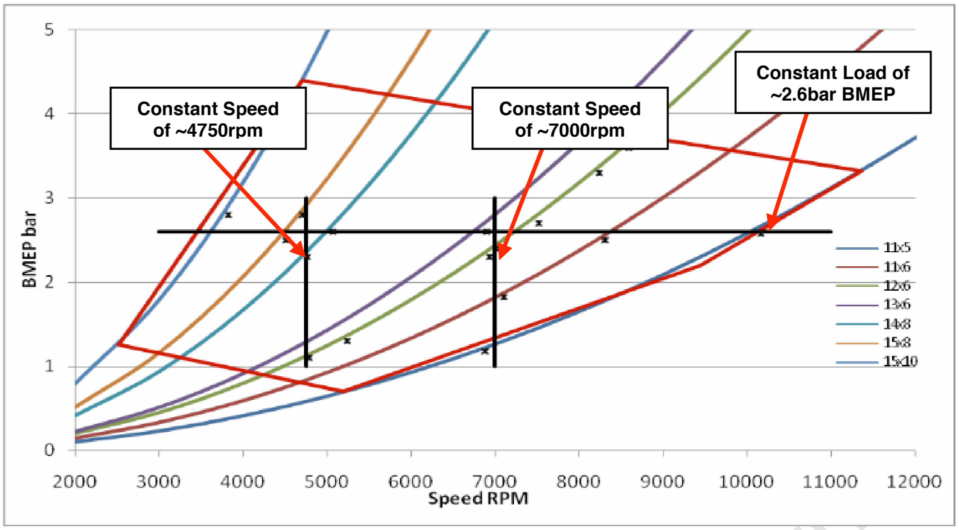

**Figure 32**: Graph of full operating range showing two lines of constant speed and a single line of constant load

Decreasing speed at a constant load advanced the combustion phasing and shortened the burn duration as can be seen in figure 33 and table 17. The observed trend agreed with classic HCCI engine characteristics and was attributed to the longer residence times of the reactants due to the slower speeds.

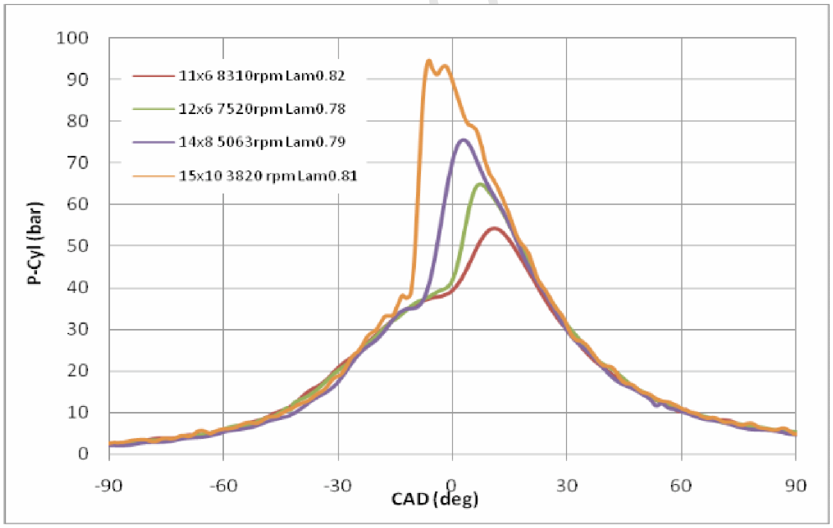

**Figure 33**: Overlay Pressure Traces of constant load points. Note the combustion phasing which advanced as speed decreased to the point of knocking on the 15x10 propeller

**Table 17**: Combustion characteristics of constant load points

| Prop | Speed | BMEP | Lambda | Max PRR | at CAD | 10-90% MFB burn duration | Pmax | at CAD |
|---|---|---|---|---|---|---|---|---|
| Xpitch | rpm | bar | | bar/deg | deg | deg | bar | Deg |
| 11x6 | 8310 | 2.5 | 0.82 | 2 | 5.2 | data lost | 54.4 | 11.2 |
| 12x6 | 7518 | 2.7 | 0.78 | 4.75 | 3.5 | 7 | 65 | 7.1 |
| 14x8 | 5063 | 2.6 | 0.79 | 5.3 | -2.9 | 6.1 | 75.4 | 3.2 |
| 15x10 | 3822 | 2.8 | 0.81 | 18.1 | -8.7 | 2.5 | 94.6 | -6.4 |

Testing the engine at a constant speed was more difficult as there were fewer points intersecting the speed-load profile of the calibrated propellers. Therefore two different speeds were tested to achieve sufficient data points to accurately observe any trend. Figure 34 and table 18 refer to the first set of tests while figure 35 and table 19 refer to the second set.

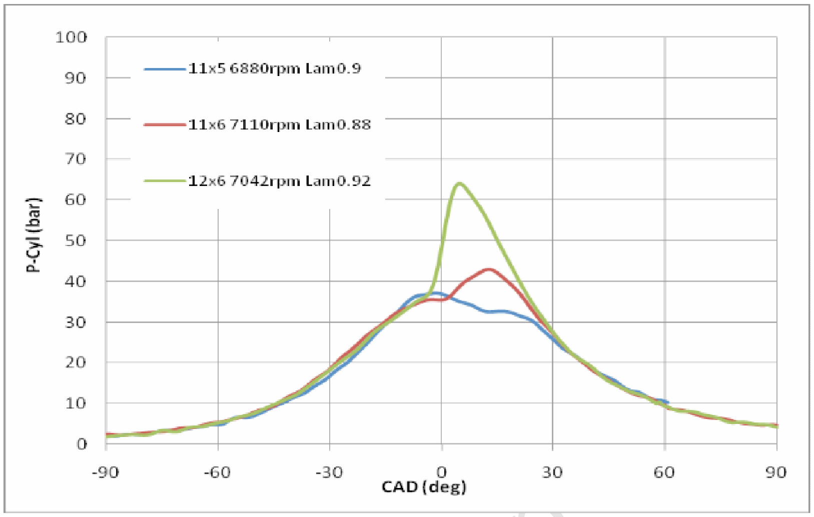

**Figure 34:** Overlay Pressure Traces of constant speed points. Note the combustion phasing which advanced as load increased.

**Table 18:** Combustion characteristics of constant speed points

| Prop | Speed | BMEP | Lambda | Burn duration 10 to 90%MFB | 50% MFB |
|---|---|---|---|---|---|
| Xpitch | rpm | Bar | | deg | CAD deg |
| 11x5 | 6881 | 1.18 | 0.9 | 16.1 | 18.6 |
| 11x6 | 7110 | 1.82 | 0.87 | 15.4 | 10.6 |
| 12x6 | 7042 | 2.4 | 0.92 | 5.7 | 1.1 |

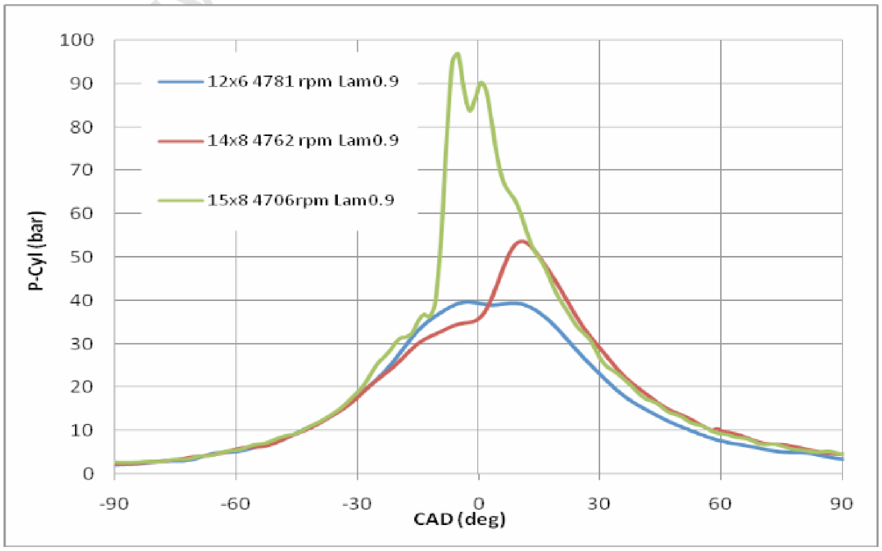

**Figure 35:** Overlay Pressure Traces of constant speed points. Note the combustion phasing which advanced as load increased to the point of knocking on the 15x8 propeller.

| Prop | Speed | BMEP | Lambda | Burn duration 10 to 90% MFB | 50% MFB |
|---|---|---|---|---|---|
| Xpitch | rpm | Bar | | deg | CAD deg |
| 12x6 | 4781 | 1.1 | 0.9 | 16.3 | 14 |
| 14x8 | 4762 | 2.3 | 0.9 | 11 | 7.3 |
| 15x8 | 4706 | 2.8 | 0.88 | 5 | -7.5 |

**Table 19:** Combustion characteristics of constant speed points

At both test-speeds, increasing the load at a constant speed advanced the combustion phasing and shortened the burn duration. This trend also agreed with classic HCCI operation and was attributed to the lower residual exhaust fraction and higher mass-fraction of inducted reactants at higher loads affecting the auto-ignition delay.

## 5.8. DISCUSSION OF EXPERIMENTAL RESULTS

The extended operating range and characteristics revealed by the experimental work showed the versatility of the model aero engine. The extended operating range of the engine exceeded high-load, low-speed limits recommended by the manufacturers. The BMEP values achieved during testing also exceed those found in the literature for similar (model aero) engines although the rated output of the engine could not be achieved. It was suspected that this was due to the fuel. D1000 provides better engine durability at the cost of performance when compared to the D3000 “racing” formulation. D3000 was recommended by the manufacturers for “high performance” and from its composition (which has a lower castor oil volume fraction and more isopropyl-nitrate) one would expect it to have a higher ignition quality than D1000. Table 20 below shows the composition of D3000.

**Table 20:** D3000 fuel specifications

| D3000 Fuel Composition | |
|---|---|
| Component | % |
| Kerosene | 47.5 |
| Di-Ethyl-Ether | 30 |
| castor oil | 20 |
| Isopropyl-Nitrate | 2.5 |

All the observed trends were inextricably linked to the auto-ignition delay of the fuel under the particular operating conditions. There was a general trend showing that as the engine speed increased, the CR required for maximum power increased (to achieve optimum phasing). This was due to the increased CR compensating the shorter residence time of the combustion gasses at higher speeds and the required shorter ignition delay for optimum timing. For low speeds (at maximum power) the maximum CR was knock-limited. This was attributed to the longer residence time due to slower speeds resulting in an ill-matched ignition delay which was too short (for the allowed residence time).

Compression ratio was found to have the single largest effect on combustion phasing and combustion duration with higher compression ratios advancing the timing and shortening the combustion duration.

Running the engine at maximum power using a fixed compression ratio (of ~15:1) showed that the engine was knock limited at low-speed conditions of maximum power on the 15x10 propeller. Conversely, the compression ratio was too low at higher speed conditions (of maximum power) on the 11x5 propeller to maintain optimum combustion phasing.

Adjusting the compression ratio also had the largest effect on the high-load limits of the operating range of the engine. Achieving maximum power required a CR which was high enough to avoid misfire, but not so high as to negatively affect combustion phasing and represented a delicate balance of compression ratio and air-fuel ratio. Utilising a leaner air-fuel ratio (if possible) without adjusting the compression ratio caused the engine to run into the lean-misfire limits due to overly retarded phasing. Similarly, adjusting the engine to a lower compression-ratio without changing the air-fuel ratio had a similar effect where the air-fuel ratio was too lean and caused misfire.

In certain cases the engine couldn't run any leaner due to a limitation imposed by the carburettor. In those cases the available leanest AFR was therefore unable to properly compliment a higher compression ratio. This suggests that the carburettor was not tuned by the manufactures to allow for the range of adjustment required by the type of varied speed/load operation that was being tested.

While accurate analysis was made difficult due to a noisy signal from the in-cylinder pressure transducer, no cool-flame was observed during the analysis of the heat-release data from any of the engine tests. This suggests that the fuel exhibits single-stage (ie. No cool-flame) auto-ignition behaviour under those operating conditions even though it showed two-stage behaviour in the E6 engine tests. It is likely that the operating conditions utilised by this engine (high speed and relatively high CR compared to the E6 tests) do not facilitate cool-flame reactions due to the shortened ignition delay of the bulk heat release. Although unlikely, it is also possible that a very low-magnitude or very early cool-flame heat release could have been masked by signal noise from the pressure transducer.

The overall engine setup was found to be inherently well suited to transient, broad-range operation on the standard load-speed profile of the 12x6 propeller. Closing the throttle from the point of maximum power with the AFR kept constant showed that the combustion phasing remained approximately constant. This suggests that the effect of speed and throttle opening (load, exhaust residuals, reactant mass fraction) are balanced resulting in approximately constant timing.

Independently testing the effects of load and speed found that increasing load advanced combustion phasing and shortened combustion duration due to a wider throttle opening causing an increase in reactant mass fraction and lowering the exhaust residuals. Increasing the speed had the opposite effect of retarding timing due to the shorter residence time of the reactants affecting the auto-ignition delay of the mixture.

The single greatest weakness of the experimental rig was the measurement of the compression ratio. Compression ratio was calculated based on the measurement of the exposed height of the compression adjustment screw. The cumbersome position of the adjustment screw meant that reliable and repeatable readings were extremely difficult to attain as even a difference of 0.01mm had a significant effect on the resultant compression ratio calculations. This introduced a large uncertainty as to the accuracy of some of the readings and may explain a lack of correlation in some of the experimental data. For example, in the last few experiments testing the “natural compensation” of the engine the compression ratio was determined from measurement to be ~12:1. The pressure values at the end of compression from the analysed pressure traces suggest the CR should be closer to ~15:1 (based on polytropic compression estimates). This particularly large discrepancy is the most extreme case, but only represents a measurement discrepancy of ~0.2mm.

# 6. ENGINE MODELLING

Experimental testing of the engine's response to changes in operating conditions showed interesting trends. The effects of speed, AFR, exhaust residuals and fuelling on combustion phasing are well known [12, 13] and the model-aero engine appeared to use a combination of these effects to achieve a naturally compensating system which maintains constant optimum combustion phasing over a variety of load and speed points (along the normal load-speed profile of the 12x6 propeller). A numerical model was used as a means of investigating of the underlying reasons for this natural compensation:

- Speed affects on the time-dependence of the auto-ignition delay
- Throttling (as a means of load and speed control) effects on cylinder temperature, exhaust residuals and the associated effects on the auto-ignition delay

A computational fluid dynamics (CFD) model was set up to investigate the engine's unique breathing system due to a suspicion that the two-stage breathing had a substantial effect on exhaust residual fraction and as a result, the overall performance characteristics of the engine. In addition, the CFD model was used to investigate the thermal distribution of the cylinder gasses as well as spatial concentration of the inducted fresh charge. The CFD model was also used to investigate the in-cylinder flow conditions from EVO to the end of compression (at TDC). As combustion usually occurred close to TDC, understanding the in-cylinder conditions at TDC helped understand the underlying reasons for the observed combustion characteristics of the engine.

As the CFD model was already set up to evaluate the breathing characteristics of the engine, it was used again to model the gas-exchange section of the combustion model.

The engine modelling was split into two sections:

- CFD model of breathing related flow characteristics and effects from EVO to TDC.
- A Microsoft Excel numerical combustion model which used data generated by a modified CFD simulation (running from EVC to EVO)

The combustion model was used to calculate the auto-ignition behaviour in response to changes in operating conditions. Data from the engine tests was used as input conditions for both models where appropriate.

## 6.1. CFD FLOW CHARACTERISATION AND THERMAL PROFILE MODELLING

### 6.1.1. CFD Modelling Philosophy

A CFD model was formulated by Mr O. Metcalfe to simulate the in-cylinder conditions from exhaust valve opening (EVO) to the end of compression (at TDC). It predicted the spatial in-cylinder temperature distribution and showed the flow dynamics of freshly inducted reactants entering the cylinder through the unique port arrangement and the effects of trapped residual gasses.

Results from this model were then used as an appropriate guide for aspects of the combustion model (such as exhaust residual fraction). In addition, it was also used to show the flow field inside the engine to provide a means of investigating the flow characteristics and effect of the engine's unique valve layout.

### 6.1.2. CFD Modelling Methodology

Fluent 6.3 was used for modelling the breathing characteristics of the engine. Temperature and pressure data (crank-case, exhaust and in-cylinder) from an engine test at EVO were used in the CFD program as inlet boundary conditions. The model ran from EVO to TDC when modelling flow effects (but only running from EVO to EVC when exclusively modelling the gas exchange process for the combustion model).

In order to simulate the gas-flow effects on the in-cylinder conditions at TDC, a single representative data point was selected and modelled.

**Table 21:** CFD data point operating conditions

| **CFD Data Point Test Conditions** | |
|---|---|
| **Propeller** | 11x6 |
| **Compression Ratio** | 15:1 |
| **Lambda** | 0.97 |
| **Ambient Temperature** | 22 $^{o}$C |
| **Speed** | 9433 rpm |
| **Coolant Temperature** | 65 $^{o}$C |
| **Exhaust Temperature** | 290 $^{o}$C |
| **Avg Head Temperature** | 158 $^{o}$C |
| **Crank Case Temperature** | 55 $^{o}$C |

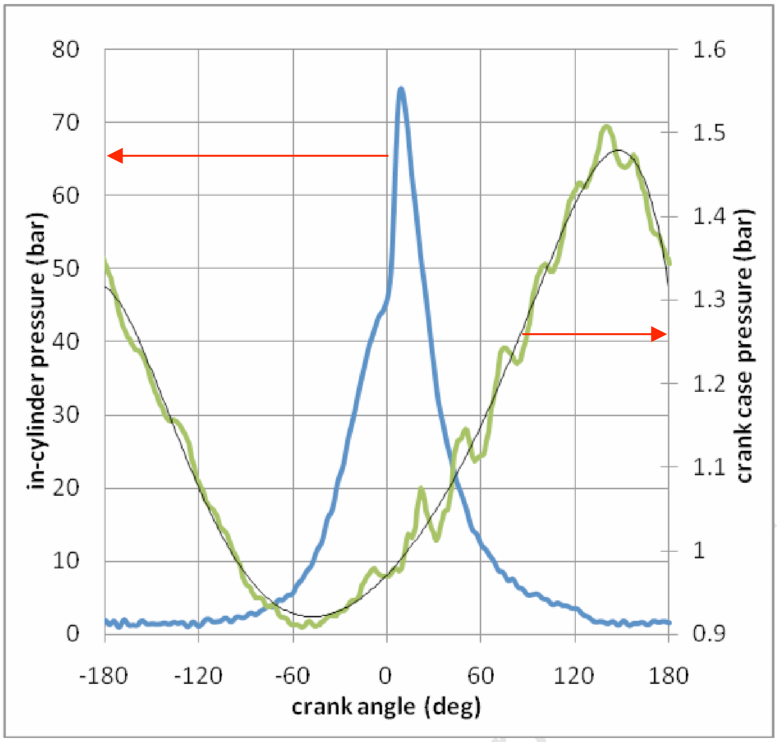

**Figure 36:** Pressure trace associated with the data point used in CFD simulation and the 6th order polynomial curve-fitting used to approximate the crank-case pressure trace.

This point was chosen as it represented the maximum power for one of the propellers recommended by the manufacturers. That specific propeller was chosen as its point of maximum power was achieved near a compression ratio which gave the widest overall operating range for the engine (representative of the most versatile engine setup).

Initially just one point was modelled due to limited CFD resources. As the investigation progressed further resources became available so the CFD simulation was allowed to play a greater role in the engine-modelling process. It was reasoned that running the CFD breathing simulation (only from EVO to EVC) for the full number of combustion simulations was more important than running a reduced number of points from EVO to TDC (as would be required due to the limited CFD resources).

Running a full simulation from EVO to TDC required approximately 4 hours per point on a 2.3GHz Dual-Core PC with 2 gigabytes of DDR2 RAM.

Running a single simulation from EVO to EVC required approximately half the time of running from EVO to TDC. Therefore, while not ideal, only a single point was modelled fully from EVO to TDC as a means of gaining some insight into the flow regimes and spatial temperature and mixture distributions. This compromise allowed the CFD simulation to be used for a wider range of modelling investigations.

### 6.1.3. CFD Modelling Results

The CFD model indicated a heterogeneous temperature distribution and residual exhaust gas fraction inside the engine. The CFD model showed a definite thermal boundary layer at the wall for the simulated data point as shown in Figure 37.

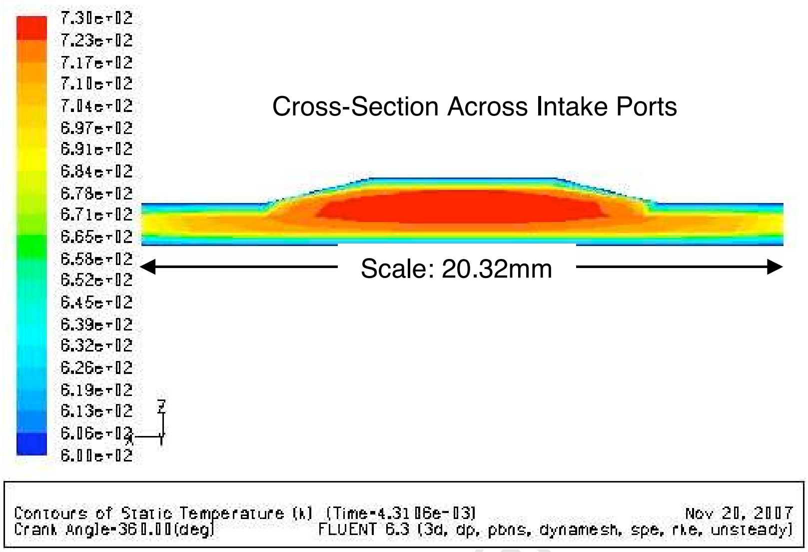

**Figure 37:** TDC (with clipped temperature scale)

Note the definite thermal boundary layer. The full thermal scale has been clipped to show better definition.

The thermal boundary layer predicted by the CFD simulation was found to be between 0.3mm and 0.4mm; approximately double the value found in the literature [14, 30]. It was found that the thermal boundary layer occupied approximately 40% of the cylinder volume at TDC (as calculated by visual inspection of cross section thermal profile data). Pronounced thermal stratification (as shown in this engine) is known to greatly affect the peak pressure rise rate and potentially improves the HCCI operating range [31, 32, 33, 34]

Figures 38 to 40 show the distribution of fresh charge in the cylinder as these gasses are compressed up to TDC. All three images clearly show the concentration of fresh charge around the intake ports. The images also show fresh charge near the exhaust ports which indicates short circuiting of the fresh charge. At the start of compression there is a significant difference between the areas of highest and lowest concentration of exhaust gas residuals.

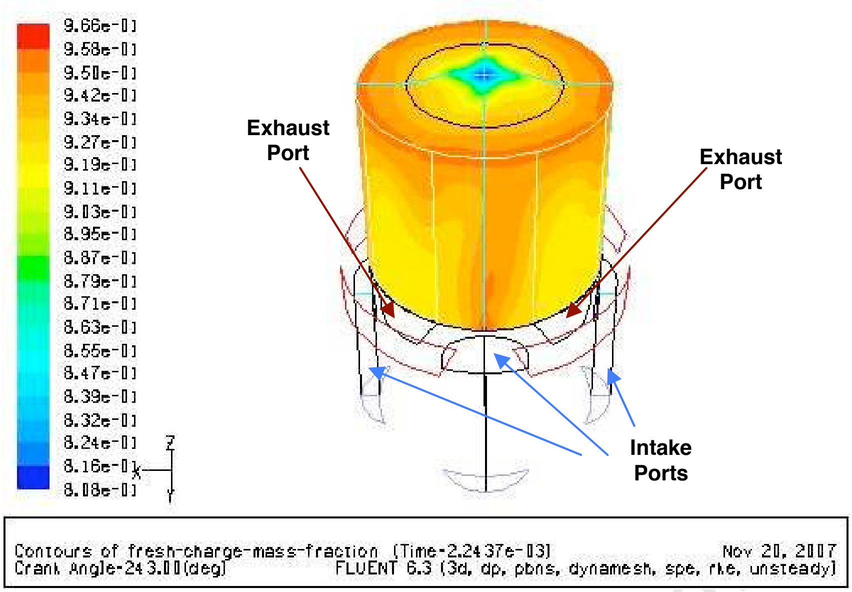

**Figure 38:** 243 ° ATDC: In-cylinder fresh-charge mass fraction at EVC. Note the symmetrical intake and exhaust port layout

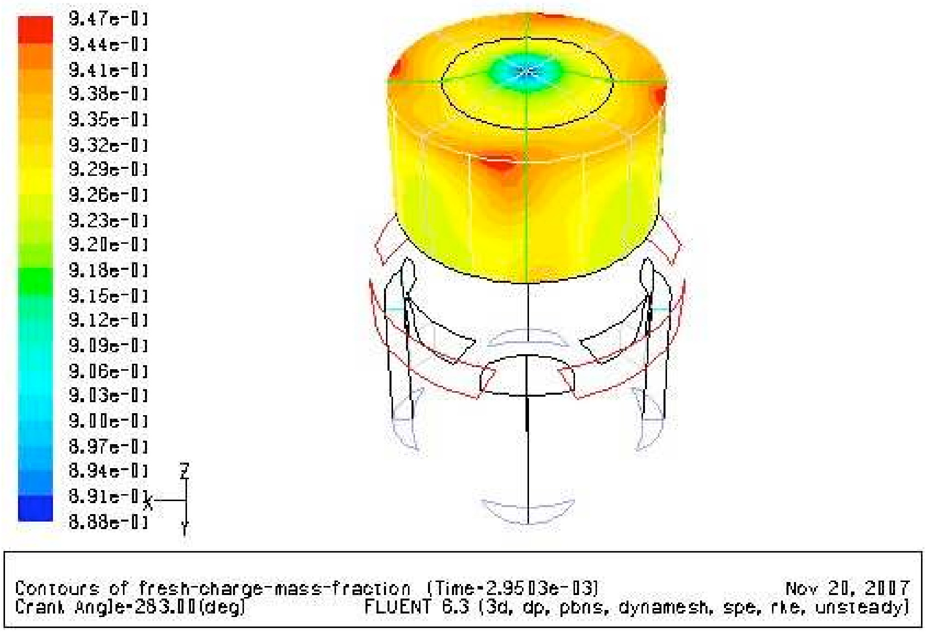

**Figure 39:** 283 ° ATDC

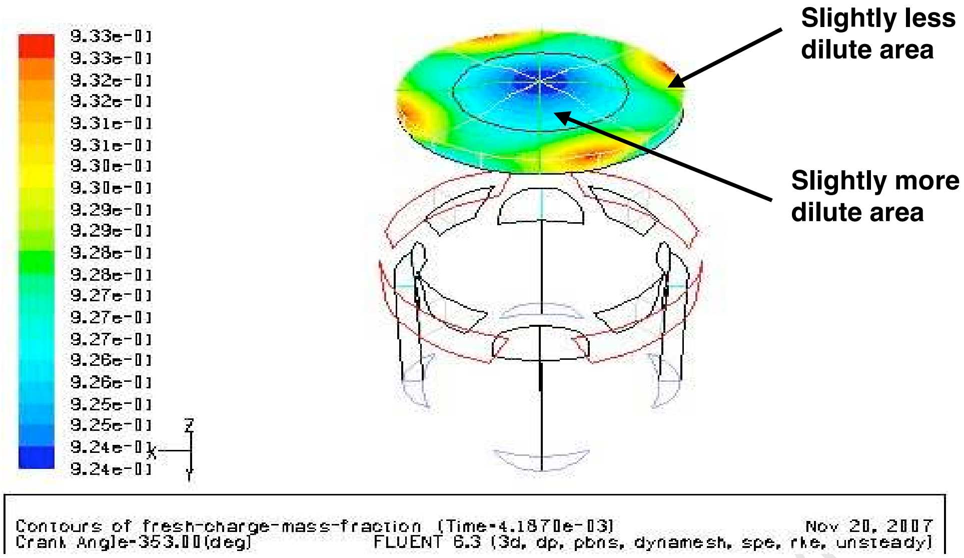

**Figure 40:** 353 ° ATDC

The images 41 to 45 show the flow-field visualisation from blow-down, through the gas exchange process into the compression of the aspirated fresh charge. Each image is coloured by the concentration of fresh charge (with red indicated the highest concentration). The length of the arrows indicates the magnitude of the gas velocity.

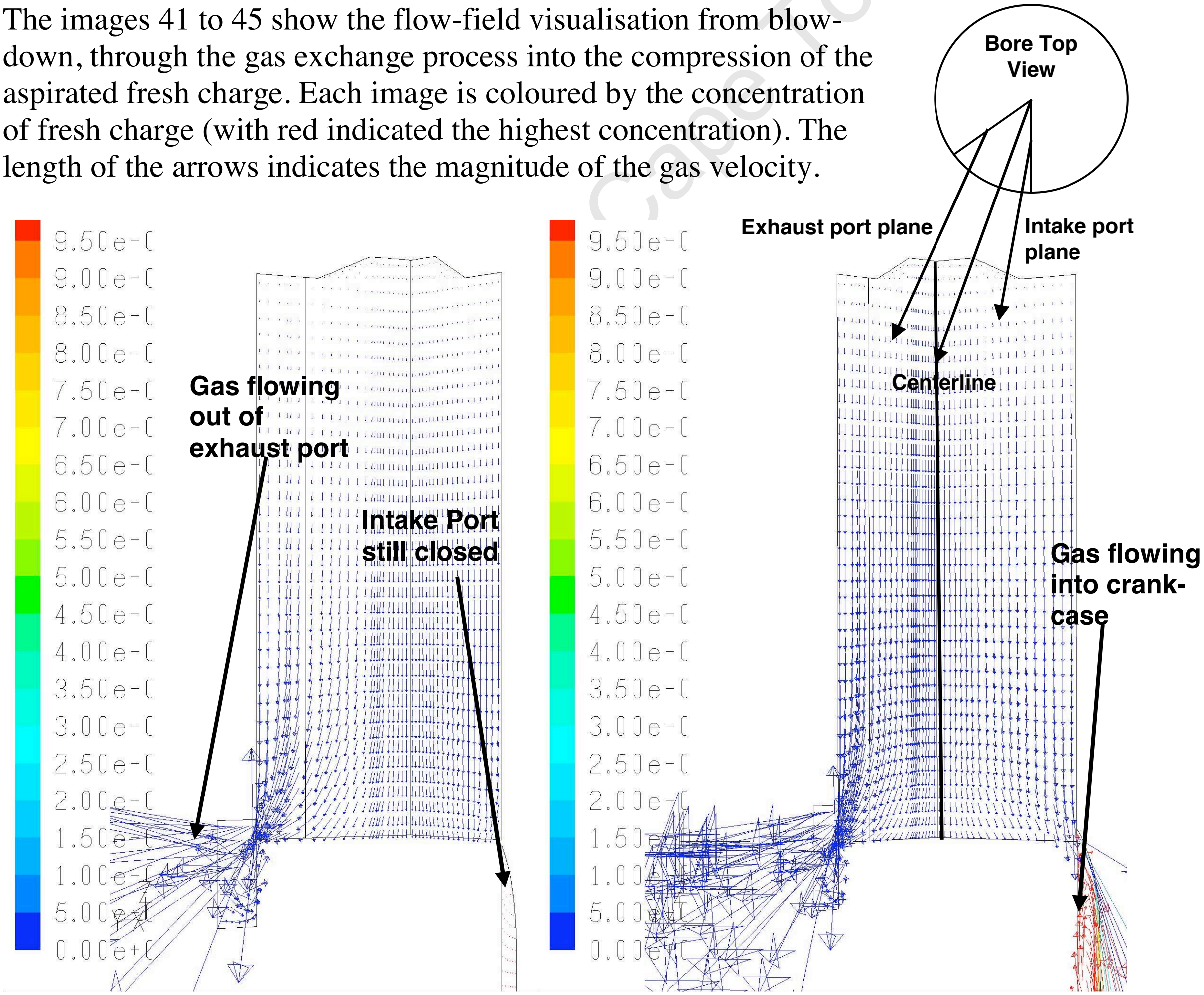

**Figure 41**: From left to right – 121° ATDC, 126° ATDC

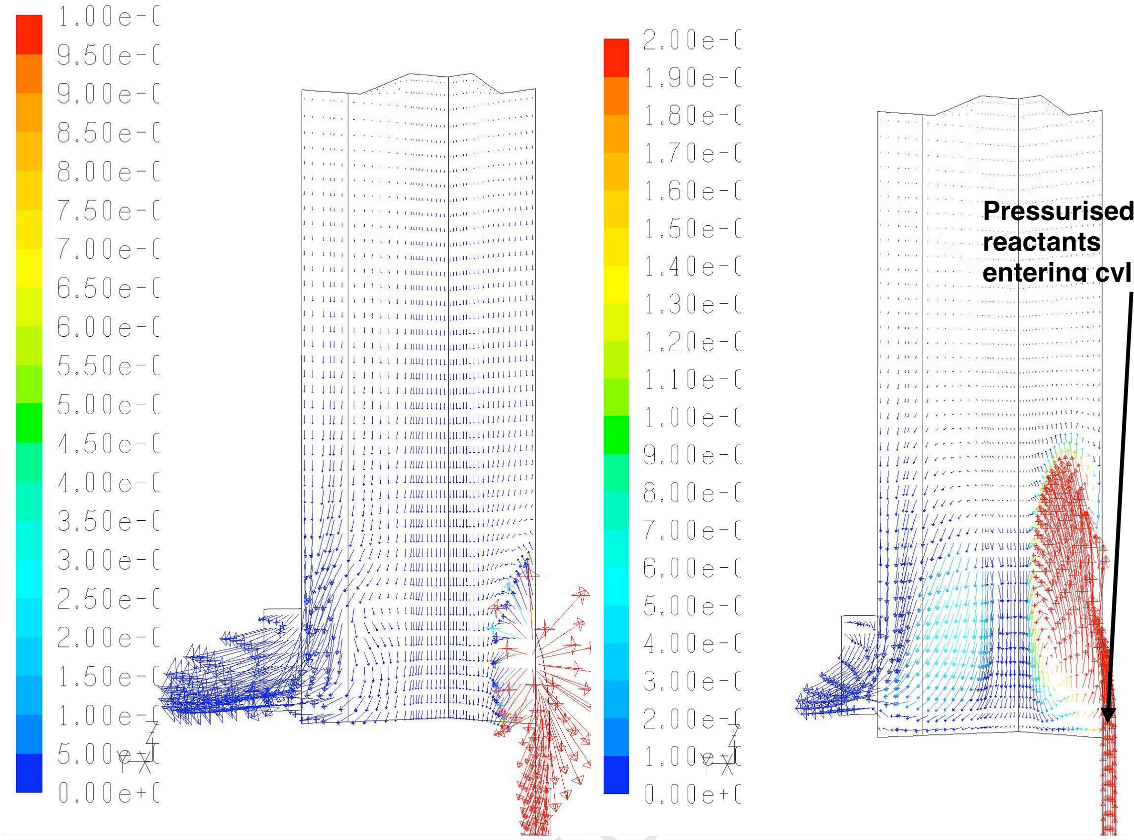

**Figure 42**: From left to right – 161° ATDC and 181° ATDC

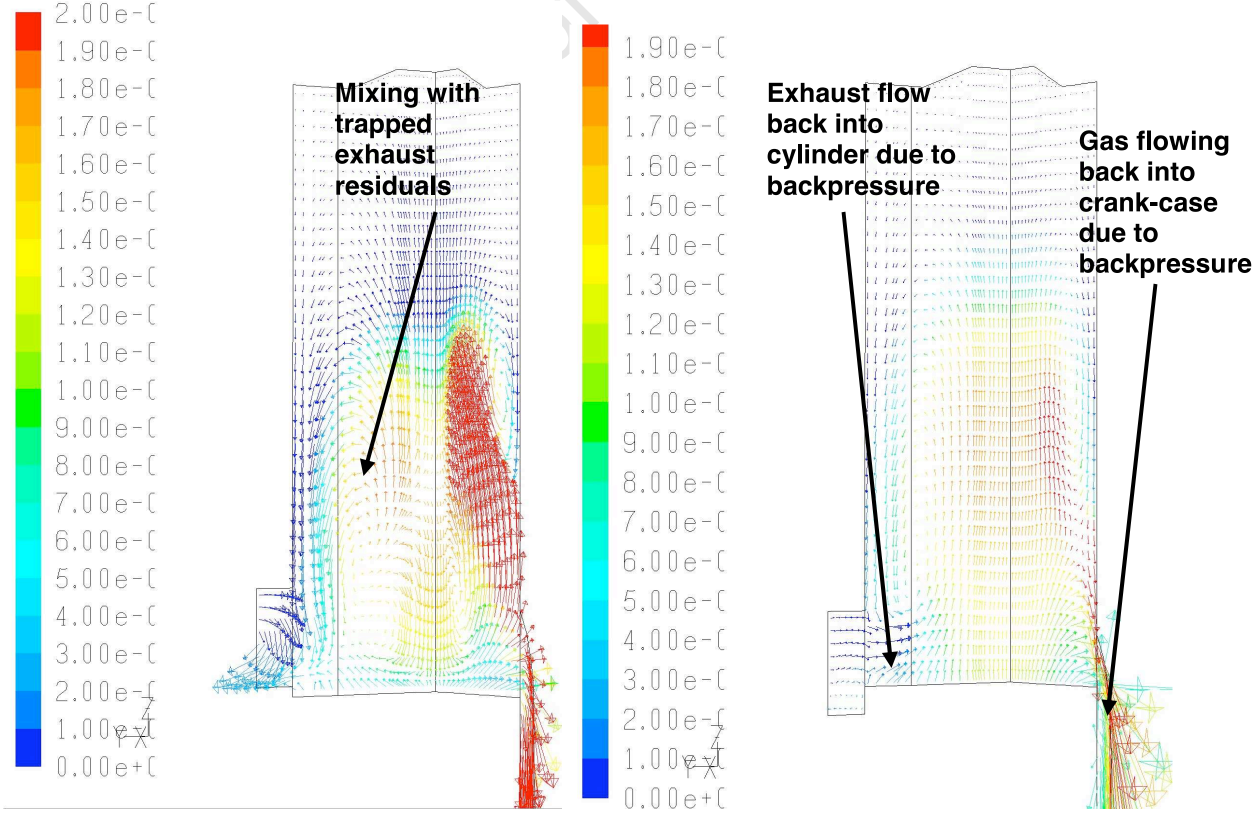

**Figure 43**: From left to right – 201° ATDC, 221° ATDC

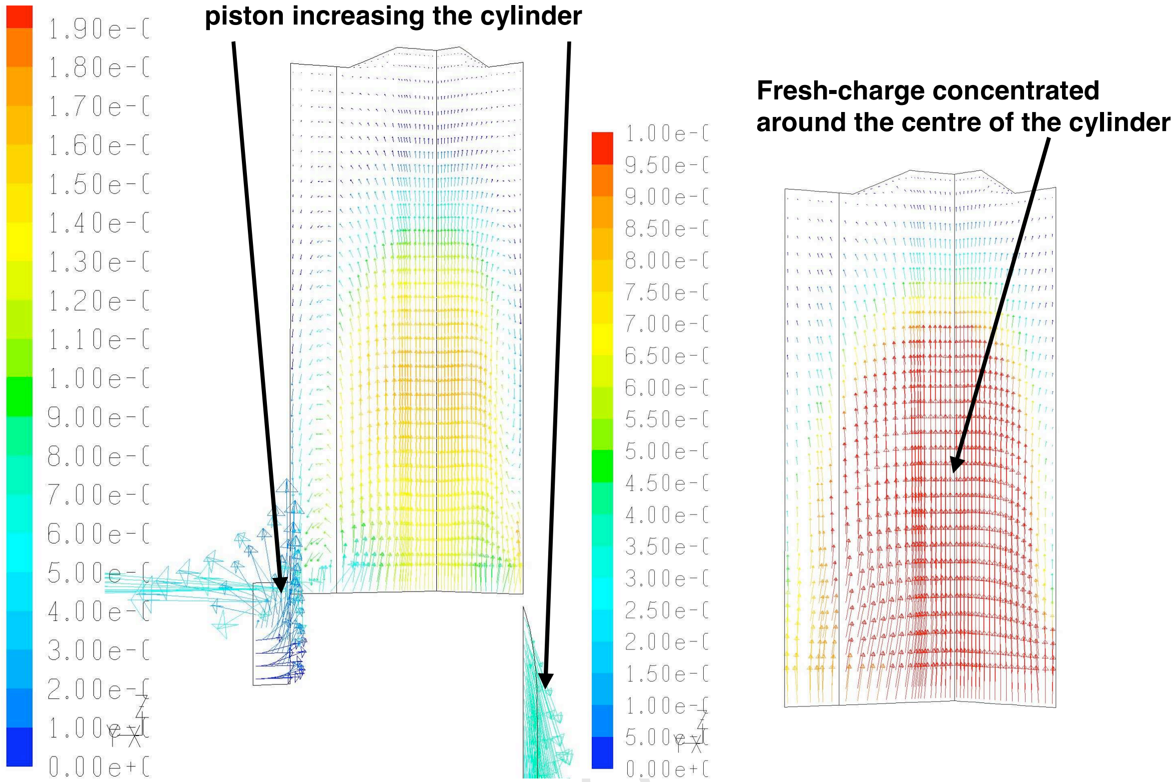

Full flow reversal due to ascending piston increasing the cylinder

Fresh-charge concentrated around the centre of the cylinder

**Figure 44**: From left to right – 241° ATDC and 261° ATDC

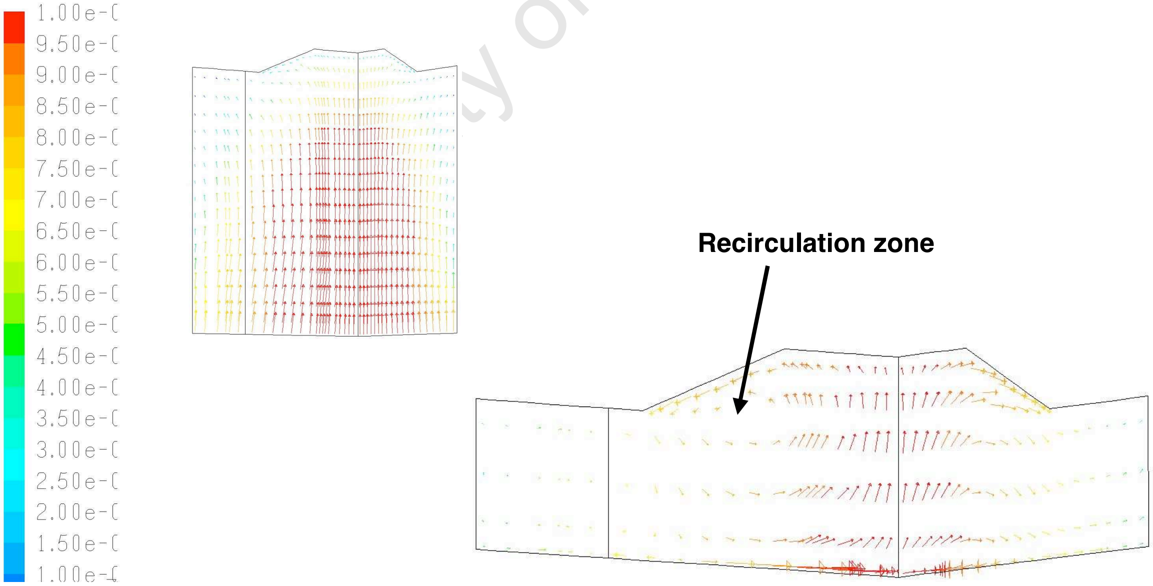

Recirculation zone

**Figure 45**: 301° ATDC and Flow conditions and mixture concentration at TDC

### 6.1.4. Discussion of CFD Modelling Results

The CFD findings as shown in Figures 28 to 40 matched the non-uniform burn patterns which were found on the cylinder head as shown in Figure 46. This pattern of four dots suggested a non-uniform temperature and mixture distribution in the cylinder most likely as a result of the engine's intake and exhaust port layout. The formation of these deposits was attributed to zones of slightly higher fresh-charge concentration and possibly liquid fuel droplets impinging on the cylinder head (due to castor-oil's high boiling point).This burn pattern was observed in the same location regardless of speed or load and was observed every time the engine was dismantled. Subsequent investigation showed the markings were aligned with the intake ports of the engine.

It's likely that this level of mixture in-homogeneity, however slight, resulted in similarly inhomogeneous burning as shown in figure 46 with combustion being initiated in the four zones of higher fresh charge concentration.

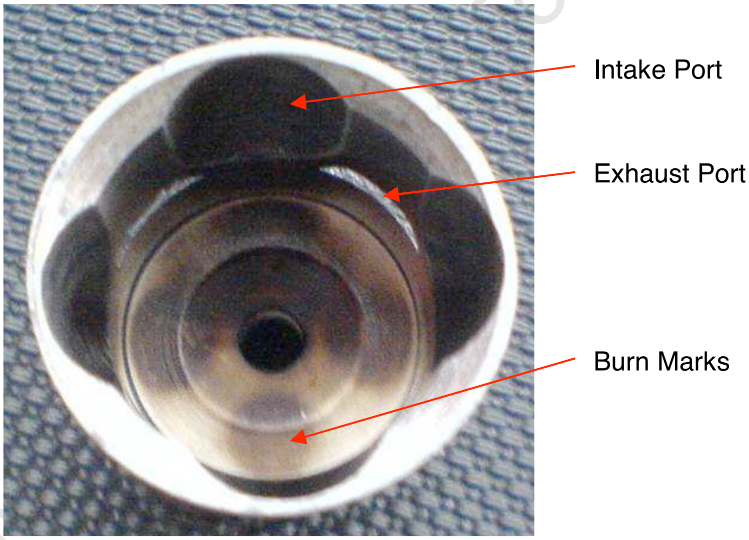

**Figure 46:** Burn pattern on the head of the model-aero engine aligned with intake ports

It appeared as if this engine might exhibit four distinct auto-ignition zones with possibly "cascading auto-ignition" propagating through the remaining mixture [35]. Depending on the levels of dilution, maximum heat release rates may be tempered as combustion proceeds towards the centre of the combustion chamber which has a lower fresh-charge concentration.

The concentrated zone of exhaust residuals combined with the four auto-ignition-initiation zones are likely one of the causes of the conservative peak pressure rise rates and knock resistance of this engine.

The flow dynamics observed in the CFD simulation showed that once blow-down was complete, a tumbling motion due to the incoming fresh charge dominated the in-cylinder flow conditions. These tumble zones were aligned with the intake ports and resulted in no swirl-mixing. It was also noted that the simulation indicated some short-circuiting of the fresh charge as gasses with a high concentration of fresh-charge were observed to be leaving the exhaust ports after exhaust blow-down (near EVC).

The CFD breathing and flow-dynamics model, while limited in its scope, provided valuable insight into the flow characteristics of the model-aero engine. Based on the results of the gas-flow simulation it appeared that the port configuration of the engine and the resultant flow regimes in the engine contributed to the observed combustion characteristics. The exhaust gas residual distribution may have a damping effect on the pressure rise rate.

The observed thermal boundary layer also appeared to be larger than previous studies had suggested. A possible explanation is the large port cross section which would lower turbulence and thus increase the boundary layer size. This phenomenon is of particular importance in very small engines as excessive heat loss may lower the peak compression-temperature sufficiently to prevent auto-ignition (and thus cause the engine to misfire or stall).When coupled to the heterogeneous mixture distribution, the large boundary layer significantly decrease heat loss (and thus affect the engine’s spatial reactivity distribution).

The magnitude of trapped exhaust residuals observed in all the CFD simulations indicates that the engine utilises residual exhaust gas as means of controlling combustion phasing. High levels of exhaust residuals maintain a sufficiently high temperature at the start of compression for the following cycle as this is known to have an effect on auto-ignition delay, although increased concentrations of exhaust residuals were found to retard timing in engine tests.

## 6.2. MICROSOFT EXCEL COMBUSTION MODELLING

### 6.2.1. Combustion Model Philosophy

The combustion model comprised a single-zone, implicit, discrete, pseudo-dimensional simulation and was set up in Microsoft Excel to model in-cylinder conditions from EVC to EVO. This model was used to investigate the auto-ignition behaviour of the engine at various operating points in the hope of investigating the following:

- Speed effect on combustion phasing
- Load effect (throttle controlled) on combustion phasing
- A combination of these two and their effect on combustion phasing (as balancing these two conflicting effects is paramount to maintaining constant combustion phasing)

Initialising the Microsoft Excel simulation required a breathing model to provide data about the cylinder conditions at EVC. As such, the same CFD model (as used in the gas flow investigation) was used to estimate the in-cylinder conditions at EVC. The outputs from the CFD model were then used to initialise the numerical simulation in Microsoft Excel. The combustion model was therefore split into two sections:

- CFD breathing model from EVO to EVC
- Microsoft Excel combustion model from EVC to EVO

The response of the engine model to changes in operating conditions provided insight into the engine's means of natural compensation for maintaining constant combustion phasing despite changing (transient) operating conditions. Modelling the same test-conditions provided a means of directly comparing the simulation to real test-data and evaluating the performance of the simulation.

The greatest handicap in formulating a realistic auto-ignition and combustion-chemistry model was a lack of sufficient data about the characteristics of the D1000 fuel blend. The closest fuel with an appropriately full data-set was n-heptane (even though the known cetane of n-heptane was lower than the measured value for D1000). n-heptane was also known to show definite two-stage auto-ignition behaviour in other engine tests while D1000 had shown no such behaviour in the model-aero engine.

Wiebe function burn-models with fixed cool flame and main heat release burn duration were used to model combustion. Engine tests with D1000 had shown different burn-durations depending on the operating conditions; varying from as short as $5^o$ to over $30^o$ CAD. Formulating an empirical model to describe the burn duration from experimental data had not yielded useful results in a related study [36]. Therefore developing a model for describing burn duration was abandoned in this case as there was no experimental data for n-heptane in the model-aero engine which could be used to develop such a model. As such, the burn duration for the cool-flame reaction was fixed at 2 CAD while the main peroxide-based burn duration was fixed at 15 CAD. While no cool flame component was observed in engine testing (with D1000), n-heptane is a two stage fuel and required a suitably short cool-flame burn-duration estimate. The main heat-release burn-duration value was based on averaging values observed during engine testing (albeit with a different fuel).

It was therefore not possible to accurately model the auto-ignition and combustion characteristics of D1000 when using n-heptane as the fuel for the simulation. It was possible to investigate the effects of engine speed as well as the associated effects of throttling and the role of these variables on the start of combustion and phasing.

Nine points were modelled to investigate changes in combustion phasing: three points to test the response to changes in speed, three points to test the response to changes in load (as a result of different throttle openings) and three points to test the combined response of those two conflicting factors. All nine points were modelled using a constant compression ratio of 12: 1 despite the test data being captured for slightly different conditions (11.9:1 and 12.3:1 depending on the data set).

A fixed compression ratio was chosen in an attempt to isolate its effect as well to ease the formulation of the CFD simulation. Modelling the two slightly different compression ratios would have required a new CFD mesh for the compression ratio; this would have required significant time while being of little benefit.

The engine test data describing the nine points can be found in Table 22 which includes the measured temperatures used as boundary conditions for the CFD simulation. The analysed pressure traces (in-cylinder, crank-case and exhaust back-pressure) were also supplied for use in initialising the CFD model (which required information such as cylinder pressure at EVO). The cylinder pressure at EVC was also included as it was used an initial condition for the combustion simulation.

Note that the expected trends for exhaust residual mass-fraction were not observed. This was attributed to the high sensitivity of the CFD simulation to exhaust back-pressure and the relative uncertainty of the accuracy of the back-pressure values (due to the smoothing techniques applied to the back-pressure trace when setting up the CFD simulation).

**Table 22**: Input data describing the test points as well the useful results from each CFD simulation.

| **CFD Data Point Test Conditions (from engine-test data)** | | | | | | | | | |
|---|---|---|---|---|---|---|---|---|---|
| **Test Set** | **Constant Speed** | | | **Constant Load** | | | **Natural Compensation** | | |
| **Prop** | **11x5** | **11x6** | **12x6** | **12x6** | **14x8** | **15x10** | **12x6** | **12x6** | **12x6** |
| **CR** | 12.3 | 12.3 | 12.3 | 12.3 | 12.3 | 12.3 | 11.9 | 11.9 | 11.9 |
| **Lambda** | 0.9 | 0.92 | 0.9 | 0.78 | 0.79 | 0.81 | 0.92 | 0.87 | 0.9 |
| **Amb Temp (°C)** | 25 | 25 | 25 | 25 | 25 | 25 | 25 | 25 | 25 |
| **Speed (rpm)** | 6880 | 7110 | 7042 | 7520 | 5063 | 3820 | 5240 | 6936 | 8596 |
| **Coolant Temp (°C)** | 65 | 65 | 65 | 65 | 65 | 65 | 65 | 65 | 65 |
| **Exhaust Temp (°C)** | 130 | 205 | 250 | 223 | 182 | 187 | 166 | 220 | 290 |
| **Avg Head Temp (°C)** | 95 | 113 | 127 | 117 | 107 | 85 | 96 | 108 | 137 |
| **Crank Case Temp (°C)** | 53 | 52 | 50 | 53 | 52 | 43 | 54 | 56 | 51 |
| **Input Data for Microsoft Excel model obtained from CFD simulation** | | | | | | | | | |
| **Cylinder Mass (kg)** | 8.3E-06 | 6.8E-06 | 6.3E-06 | 7.1E-06 | 7.0E-06 | 6.7E-06 | 7.0E-06 | 6.7E-06 | 7.2E-06 |
| **Ex Residual Mass (%)** | 27 | 24 | 25 | 22 | 25 | 26 | 23 | 22 | 24 |
| **Cyl Temp @ EVC (°C)** | 39 | 90 | 118 | 72 | 70 | 89 | 73 | 97 | 104 |
| **Cyl Press @ EVC (bar)** | 1.22 | 1.17 | 1.17 | 1.17 | 1.13 | 1.14 | 1.15 | 1.17 | 1.3 |

## 6.2.2. Combustion Model Formulation

The gas exchange process from EVO to EVC was modelled in an identical fashion to the gas-flow CFD simulation although this time the period of interest was from EVO to EVC (instead of all the way to the end of compression). The combustion model was initialised using the Exhaust Residual Mass Fraction (ERF), EVC temperature and EVC pressure from the CFD breathing simulation. All other factors were either measured on the engine directly (like geometric relationships) or obtained directly from engine test-data. Measurements of the average head-temperature were also used for estimating the heat loss.

A fundamental component utilised extensively throughout the model was Microsoft Excel Solver; a tool used to find a solution which satisfies a complex relationship using iterative numerical methods. Solver attempts to achieve a desired solution to a complex function (based on multiple, inter-dependent equations) by changing input variables in a user-defined manner until a satisfactory level of accuracy is attained. Microsoft Excel Solver is used to solve a system of equations which would otherwise be extremely difficult (but not impossible) to solve. It should be noted that the Solver module used in this study was based on Newton's Method and thus does not guarantee a solution as the iterative methods used are unstable. Solver is similar to Microsoft Excel Goalseek although Goalseek only allows for the variation of a single input-variable and does not facilitate as much user-control over the mechanisms of the module (such as accuracy, trial-solution limits etc). Therefore Goalseek, while simpler, was not suitable for this study.

During the formulation process there was often no means of calculating an instantaneous value for a particular variable, but only to use a relationship which involved values from a previous calculation step. For this reason, the subscript notation "1" refers to a variable in the previous step whereas the subscript notation "2" refers to that variable in the current or "active" step. Each calculation step comprised an active row of cells which contained formulae relating to the current CAD step and a passive row which contained the values calculated in the previous CAD step. The description of the Microsoft Excel combustion simulation is best split up into the following sections and will be described as such:

- The Control Volume Energy Balance
- Input Data, and General Methodology
- Calculating Thermodynamic Properties Using JANAF derived Data Tables
- Heat Loss and the Compression Cycle Energy Balance
- Combustion Chemistry Kinematics and Thermodynamics
- Arrhenius form Auto-ignition Integral Method

***6.2.2.1.The Control Volume Energy Balance:*** Each step of the model relied on the following implementation of the 1st law of thermodynamics holding true between any two calculation steps:

$$Q_{2-1} - W_{2-1} = \Delta U_{2-1} \qquad \text{(Equation 6)}$$

Where the heat added to the system minus the work leaving the system is equal to the change in internal energy of the system (other energy descriptors such as kinetic or potential energy were regarded as negligible in this simulation). All the relevant changes in the thermodynamic properties of the in-cylinder gasses were tracked and calculated based on the aforementioned energy equation. Knowing or calculating each particular element of the above equation became what defined each section of the combustion model. Each element of the control-volume energy balance is described as follows:

Heat Transfer

$$Q = h_c \times A \times (T_{cyl} - T_{wall}) t_{step} \qquad \text{(Equation 7)}$$

The combustion chamber area exposed to the in-cylinder gasses is geometrically linked to the crank position and the time step was calculated as function of engine speed and calculation step size. The heat transfer coefficient, $h_c$, was derived using the Woschni method [37], which itself was also based primarily on the constantly changing $P_{cyl}$ and $T_{cyl}$.

Work

$$\underset{2-1}{\Delta W} = \underset{2-1}{P_{AVG}} \times \underset{2-1}{\Delta V} \qquad \text{(Equation 8)}$$

Instantaneous volume was calculated using the geometric relationship between CAD and the proportions of the engine [38]. The in-cylinder pressure was related to the in-cylinder temperature through the ideal gas law:

$$PV = mRT$$

In which case one needed to know the in-cylinder mass and the specific gas constant of the cylinder gas mixture.

Internal Energy

$$U = H - mRT_{cyl} \text{ or } U = H - P_{cyl}V \qquad \text{(Equation 9)}$$

The first part of the equation, Enthalpy (H), is a property of the thermodynamic state of the cylinder gasses and was dependent on the temperature of the gasses. The second part of the equation is interchangeable using the ideal gas law, but again required knowledge of either the in-cylinder pressure or temperature.

As the cylinder represented a closed volume between EVC and EVO it was possible to calculate the cylinder mass at EVC using the ideal gas law and use that value throughout the simulation.

***6.2.2.2. Initialising the Model and General Methodology:*** In addition to factors derived from or used for the CFD model, the following physical properties of the engine served as the obvious foundation for the model as well as most geometry-based relationships:

- Bore (measured)
- Stroke (measured)
- Con-rod/Crank radius (measured)
- Speed (test-point dependant)
- Compression Ratio (measured )
- CAD at EVC (measured)
- CAD at EVO (measured)
- Calculation step size (chosen as 0.5 CAD to provide suitable accuracy)

In addition various other aspects of the model also required data in the form of:

- JANAF-derived thermodynamic data tables (appendix 6)
- Fuel properties related to auto-ignition delay modelling (appendix 7)
- Woshni Heat release model coefficients (appendix 8)

The formulae used to determine the three elements of the energy equation required values for the following variables over two calculation steps:
- in-cylinder temperature
- in-cylinder pressure
- properties relating to the thermodynamic state of cylinder gasses (R, H, Cp, Cv etc.)

The thermodynamic state of a gas is given by the ideal gas law: PV=mRsT so for a given trapped mass (m) of known composition (Rs) in a known volume (V), a change in pressure can be directly related to a change in temperature.

The input conditions (measured or from CFD) at EVC were used to initialise the first calculation step of the simulation (at EVC). It was possible to calculate cylinder-pressure from in-cylinder temperature using the ideal-gas law and the properties describing the energy state of the gasses were formulated as a function of the in-cylinder temperature. As most of the formulae used temperature directly, this was chosen as the dependent variable to solve at each calculation step.

The effect of exhaust gas residuals were incorporated into the model in the following manner:
- Composition of the exhaust residual mass fraction (ERF) and the associated thermodynamic properties were based on cylinder gas composition at EVO (up until the start of combustion, after which the combustion reactions govern the composition of the in-cylinder gasses)
- ERF displaced (and thus reduced) the fresh-charge mass at EVC
- The effect of ERF on the thermodynamic properties of the cylinder gasses was included as a proportionate change in the thermodynamic properties at EVC

During compression, the model utilised Microsoft Excel Solver to solve for the temperature of the unburned gasses so as to satisfy the energy balance. During combustion and expansion Microsoft Excel was required to solve for the temperature of the combusting components as well as the molar ratios of the gas components in order to satisfy both the energy balance and the combustion reactions.

The combustion simulation is a single-zone combustion model due to the assumed homogeneity of the mixture in an HCCI engine. As a result, the entire contents of the cylinder is always at the same pressure and temperature. During combustion the homogeneous mixture evolves in composition from all reactants (at the start of combustion) to mixed reactants and products (during combustion) to all products (after combustion). As such it did not account for the mixture and temperature in-homogeneities observed in the CFD simulation (although the Woschni method of heat transfer accounts for the effects of the boundary conditions at the cylinder wall).

***6.2.2.3. Calculating Thermodynamic Properties:*** The planned energy balance-based simulation required accurate values for a variety of related thermodynamic properties, namely: The gas constant (R) and enthalpy (H). In addition to these values, the combustion chemistry section of the model required values for Entropy (S) and Gibbs free energy (G) where the derivation of both relied on a variation of the same property-tables based method described below.

Enthalpy was calculated using the following technique:

$$\bar{h} = \int Cp\,dT \qquad \text{(Equation 10)}$$

As enthalpy is a function of temperature only, it was possible to calculate Cp and h using the following relationships for each component of the gaseous mixture inside the cylinder:

$$Cp(T) = a + bT + cT^2 + dT^3 + eT^4 \qquad \text{(Equation 11)}$$

Where a, b, c, d and e are constants (found using JANAF derived thermodynamic property tables in appendix 6) specific to a particular compound and a particular temperature range (hence the high and low temperature values given in the appendix).

The calculation for Enthalpy therefore takes on the following form:

$$\text{note: } \mathrm{h}_{\text{state,(T)}} = \mathrm{h}_{\text{formation, (T=0K)}} + \mathrm{h}_{\text{sensible, (T)}} \qquad \text{(Equation 12)}$$

$$Cp = \left(\frac{\partial h}{\partial T}\right)_p \quad \therefore\ \mathrm{h}_{\text{sensible, (T)}} = \int_0^T C_{p,(T)}\ dt \qquad \text{(Equation 13)}$$

$$\text{empirically, } \mathrm{C_P} = a + bT + cT^2 + dT^3 + eT^4$$

$$\therefore\ \mathrm{h}_{\text{sensible, (T)}} = \left| aT + \frac{b}{2}T^2 + \frac{c}{3}T^3 + \frac{d}{4}T^4 + \frac{e}{5}T^5 + \text{constant} \right|_0^T \qquad \text{(Equation 14)}$$

$$\therefore\ \mathrm{h}_{\text{sensible, (T)}} = aT + \frac{b}{2}T^2 + \frac{c}{3}T^3 + \frac{d}{4}T^4 + \frac{e}{5}T^5 \qquad \text{(Equation 15)}$$

but : $\mathrm{h}_{\text{formation}}$ given at 298K and not 0K

and : $\mathrm{C_P}$ coefficients only valid in particular ranges of T

$$\text{from} \quad \mathrm{h}_{\text{state,(T)}} = \mathrm{h}_{\text{formation, (T=0K)}} + \mathrm{h}_{\text{sensible, (T)}}$$

$$\text{reformulate: } \mathrm{h}_{\text{state,(T)}} = \left(\Delta \mathrm{h}^0_{\mathrm{f}_{298}} - \mathrm{h}^0_{\text{sensible}_{298}}\right) + \mathrm{h}_{\text{sensible, (T)}} \qquad \text{(Equation 16)}$$

At a specific temperature this became:

$$\mathrm{h}_{\text{state,(T)}} = \left(\Delta \mathrm{h}^0_{\mathrm{f}_{298}} - \mathrm{h}^0_{\text{sensible}_{298}}\right) + \mathrm{h}_{\text{sensible, (T)}} \qquad \text{(Equation 17)}$$

$$\text{where: } \mathrm{h}_{\text{sensible, (T)}} = aT + \frac{b}{2}T^2 + \frac{c}{3}T^3 + \frac{d}{4}T^4 + \frac{e}{5}T^5 \qquad \text{(Equation 18)}$$

$$\text{and: } \mathrm{u}_{\text{state,(T)}} = \mathrm{h}_{\text{state,(T)}} + R_u T \qquad \text{(Equation 19)}$$

The gas constant at a particular composition and temperature was found using:

$$R_{overall} = \frac{R_{universal} * (1 - mfb)}{(molecular.weight)_{reac\tan ts}} + \frac{R_{universal} * (mfb)}{(molecular.weight)_{products}} \qquad \text{(Equation 20)}$$

The gas constant only changed during combustion when the reactions changed the composition of the cylinder gasses.

In addition, Cv was found using the following relationship:

$$Cv = Cp - R \qquad \text{(Equation 21)}$$

***6.2.2.4. Heat Loss and the Compression Cycle Energy Balance:*** As mentioned previously, heat loss was modelled using the widely accepted Woschni method to estimate a bulk heat transfer coefficient. Following is a figure showing the complex temperature profile as heat is transferred from the cylinder gasses to the coolant liquid.

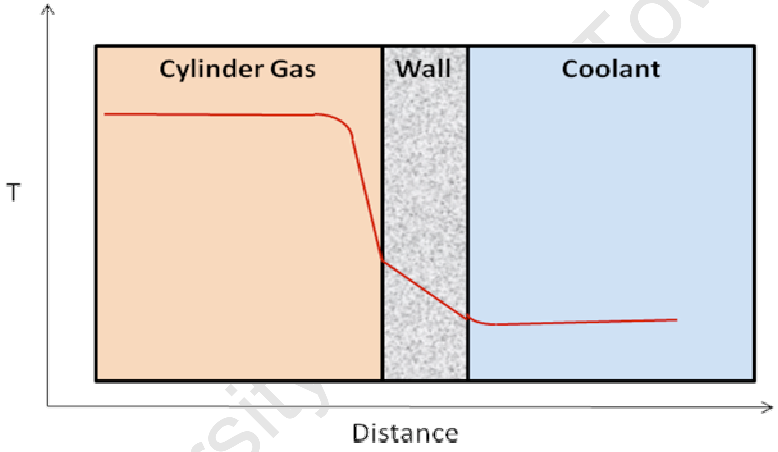

**Figure 47**: Temperature drop (not to scale) as a function of distance from the in-cylinder gasses to the coolant.

Note the constant in-cylinder temperature which only drops once it reaches the boundary layer at the wall. Once at the wall, temperature drops according the heat transfer coefficient of the wall material until it reaches the boundary layer at the transition between wall and coolant fluid. Once past that boundary layer, the temperature assumes the constant value of the coolant fluid. Woschni combined discreet heat-transfer mechanisms into a single convective heat transfer coefficient, $h_c$ [39]. The measured average temperature of the cylinder-head was used to estimate the wall temperature ($T_{wall}$) as required by the heat-loss model. This value likely under predicted the actual value for $T_{wall}$ due to the temperature drop across the wall as shown in Figure 47.

Woschni's method relates the heat transfer coefficient, $h_c$, to in-cylinder average gas velocity, *w* using the following two equations:

$$h_c = 3.26 Bore^{-0.2} \times P_{cyl}^{\ 0.8} \times T_{cyl}^{\ -0.55} \times w^{0.8} \qquad \text{(Equation 22)}$$

$$w = \left[ 2.28 S_P + C_2 \frac{V_d T_{ref}}{P_{ref} V_{ref}} (P_{cyl} - P_{motored}) \right] \qquad \text{(Equation 23)}$$

Where:
$S_p$ is the piston speed
$V_d$ is the displaced volume
$T_{ref}$,$V_{ref}$ and $P_{ref}$ are arbitrary reference conditions (BDC)
$P_{motored}$ is the motored pressure at the same CAD as $P_{cyl}$
$C_2$ is 0 for the compression period and 3.24 x $10^{-3}$ for combustion and expansion [39]

The motored pressure was calculated from the motored temperature using the ideal gas law while the motored temperature was calculated using the following polytropic relationship:

$$T_2 = T_1 \times \left(\frac{V_1}{V_2}\right)^{\gamma - 1} \qquad \text{(Equation 24)}$$

Where:

$$\gamma = \frac{Cp}{Cv} \qquad \text{(Equation 25)}$$

As the composition of the in-cylinder gasses did not change during compression, the relevant thermodynamic properties of the gasses were a function of temperature only.

Wherever in-cylinder pressure was required (to calculate work for example) it was calculated using the ideal gas law from $T_{cyl}$ (recall that thermodynamic properties also depend on $T_{cyl}$).

Through these inter-related set of equations, Microsoft Excel solver was able to solve for an in-cylinder temperature which satisfied the energy balance.

***6.2.2.5. Combustion Chemistry Kinematics and Chemical Equilibrium:*** A full formulation of this method can be found in Heywood JB, Internal Combustion Engine Fundamentals, McGraw-Hill Singapore, 1988 from page 86. What follows below is a brief summary:

During compression the model has to solve for temperature as all the other gas-properties are a function of temperature only as the composition of the mixture does not change.

During combustion reactants evolve to products and even after combustion the composition continues to evolve until a low-temperature threshold is reached. In addition to balancing the energy equation during combustion, the model also had to solve for the evolving mixture composition and as such required a discreet section to evaluate the combustion chemistry.

Consider the main combustion reaction:
$HC + (O_2 + 3.77N_2) \rightarrow CO_2 + H_2O + 3.77N_2$ (Equation 26)

In this form there is no way to account for the effects of non-stoichiometric air-fuel ratios or two other important dissociation reactions which slightly lower the temperature rise due to combustion.

Namely, the water gas shift (WGS) and the $CO_2$ dissociation reactions:

WGS: $H_2O + CO \Leftrightarrow H_2 + CO_2$ (Equation 27)
$CO_2$ Dissociation: $CO_2 \Leftrightarrow {}^1\!/_2 O_2 + CO$ (Equation 28)

The inclusion of these two dissociation reactions results in a lower combustion temperature rise due to the interaction between the three reactions [40]. Including these two equations also results in extra variables to solve when considering the molar ratios of the resulting combustion reaction in its entirety.

The consideration of these two reactions resulted in a combustion reaction of the following form (with n-heptane as the fuel):

$C_7H_{16} + n(O_2 + 3.77N_2) \rightarrow aCO_2 + bH_2O + cCO + dH_2 + eO_2 + n(3.77)N_2$ (Equation 29)

Where *n* is the molar air-fuel ratio and *a, b, c, d* and *e* are the molar concentrations of the other reaction species. The effects of Nitrous Oxide formation were not modelled.

The molar air-fuel ratio was determined based on the stoichiometric molar air-fuel ratio and the actual equivalence ratio, but this still left the five coefficients describing molar concentration which could not be solved without extra information (as there were more unknowns than systems of equations with which to solve them).

Using the second law of thermodynamics and the concept of Gibbs free energy, it was possible to calculate the molar concentrations of the combustion reaction species in the following manner:

The second law of thermodynamics states that any heat transfer will always increase the entropy of a system:
$\frac{dQ}{dT} \leq dS$ (Equation 30)

The rate and direction of any reaction is dependent upon the available energy and the concentration of the species involved [41]. Both these characteristics are incorporated into the reaction rate coefficient $K_p$ which describes the direction a reaction will proceed based on the environmental conditions of the reaction.

The concept of Gibbs free energy implies that the value for the "Gibbs free energy" in a system predicts how a reaction will occur [42]. $K_p$ was related to Gibbs free energy through the following equation:

$$K_p = \exp\left(\frac{-\Delta G^*}{R_{universal} T_{cyl}}\right) \qquad \text{(Equation 31)}$$

Where $\Delta G^*$ is a measure of Gibbs free energy in a system.

Interpreting this relationship yields three possible values for $K_p$ (depending on the temperature of the system and the value of $\Delta G$):
$K_p >> 1$ – forward reaction is favoured
$K_p << 1$ (but $>0$) - reverse reaction is favoured
$K_p = 1$- reaction is at equilibrium because at equilibrium $\Delta G = 0$

$\Delta G$ is related to the second law of thermodynamics through the following equation:

$$\Delta g = \Delta h - T_{cyl} \Delta s \qquad \text{(Equation 32)}$$

The change in entropy ($\Delta S$) was calculated in a similar fashion to $\Delta H$ using the thermodynamic data tables mentioned earlier but using the following integral:

$$S = \int \frac{Cp}{T} dT \qquad \text{(Equation 33)}$$

$\Delta S$ is therefore also is also a function of $T_{cyl}$. A full derivation of the method used to determining $\Delta S$ can be found in appendix 9.

Due to the small time steps (and temperatures and pressures) being considered it was not possible to assume the reactions had reached equilibrium so one cannot assume $K_p$= 1[40].

$K_p$ may also be described in terms of the partial pressures and molar ratios of a reaction [42]. The full derivation of this method can also be found in appendix 10. In the case of each reaction, the specific forms were as follows:

CO2 Dissociation: $K_p CO_2 = \frac{\sqrt{e_{O_2}} \times c_{CO}}{a_{CO_2}} \times \sqrt{P_{cyl}}$ and also $K_p CO_2 = \exp\left(\frac{T_{cyl}\Delta S + \Delta H}{R_{universal} T_{cyl}}\right)$

Water Gas Shift: $K_p WGS = \frac{d_{H_2} \times a_{CO_2}}{b_{H_2O} \times c_{CO}}$ and also $K_p WGS = \exp\left(\frac{T_{cyl}\Delta S + \Delta H}{R_{universal} T_{cyl}}\right)$

Where *a, b, c, d* and *e* represent the molar concentration of each species. In addition, $\Delta S$ and $\Delta H$ are calculated using only the species involved in each reaction.

Recalling the original combustion equation:

$$C_7H_{16} + n(O_2 + 3.77N_2) \rightarrow aCO_2 + bH_2O + cCO + dH_2 + eO_2 + n(3.77)N_2$$

The molar concentrations *a, b, c, d* and *e* have to be consistent for both sets of equations.

Balancing the moles of carbon, hydrogen and oxygen (in the global combustion equation) adds three equations to the two equilibrium equations and the original energy equation.

This totalled six systems of equations which Microsoft Excel Solver could use to determine the six unknown variables (the molar concentrations and in-cylinder reaction temperature).

It should be noted that while heat-release may finish at the end of combustion, the composition of the cylinder gasses continue to evolve for some time due to the high temperature. A check was built-in so the composition of the gasses ceased to evolve only when the temperature dropped below 1750K [40] and the dissociation reactions ceased to play a major role. After which Microsoft Excel solver switched to solving for temperature only in much the same way as for the compression cycle.

In this manner the composition and thermodynamic properties of the combustion gasses were determined at each calculation step from the start of the combustion all the way to EVO.

***6.2.2.9. Arrhenius Form Livengood and Wu Auto-Ignition Integral Method:*** It is not possible to accurately determine the auto-ignition delay of a combustible mixture using an empirical formula without accounting for the pressure and temperature history of the mixture. Instantaneous evaluation of ignition delay results in grossly overestimated ignition delay times [43].

The widely accepted Livengood and Wu method of calculating ignition delay involves the instantaneous evaluation of the aggregated values from an integral form of an Arrhenius type equation (describing the auto-ignition behaviour of the fuel in question). This integral is evaluated over the specific period and once the aggregated values have reached unity auto-ignition is said to occur [43].

The auto-ignition model was split into two separate Arrhenius equations [14], one to describe the cool-flame (OH radical-based) and another which described the main heat release (Peroxide based). Separate Wiebe functions were also used to control the burn-rate of both the cool-flame and main heat release. A cool flame component was required for n-heptane despite the fact that no cool flame was observed in engine testing with D1000. A table detailing the coefficients used for this analysis (relating to n-heptane) can be found in Appendix 7.

Cool-Flame

The first step for evaluating ignition delay was to calculate the ignition delay of the cool flame as follows:

$$\tau_{CF} = \Phi^{B_1} \times A_1 \times P_{cyl}{}^{n1} e^{\frac{B_1}{T_{cyl}}} \qquad \text{(Equation 34)}$$

Apart from the equivalence ratio (   ) and the instantaneous in-cylinder conditions ($T_{cyl}$, $P_{cyl}$), all other variables are empirical constants.

Auto-ignition of the cool-flame occurs when the following integral reached unity as evaluated from EVC to the current CAD step:

$$\int_{t_{EVC}}^{t_{current}} \frac{dt}{\tau_{CF}} \rightarrow 1 \qquad \text{(Equation 35)}$$

At which point the temperature rise due to the cool-flame heat release was calculated using the following formula:

$$\Delta T_{CF} = \omega(T_{cyl} - T_{EQ} \times P_{cyl}{}^{k} \times \Phi^{\mu}(\frac{100}{99+\Phi})^{\sigma}) \qquad \text{(Equation 36)}$$

It was then necessary to calculate the mass burned during the cool-flame which would achieve the appropriate temperature rise as calculated previously:

$$m_{CF} = m_{cyl}(\frac{Cv_{reac}T_{cyl}}{U_{reac}} - \frac{Cv_{prod}(T_{cyl} + \Delta T_{CF})}{U_{prod}}) \qquad \text{(Equation 37)}$$

Where Cv and U for the reactants were calculated at the cylinder temperature prior to the cool-flame temperature rise. Cv and U for the products were calculated at the cylinder temperature after the cool flame temperature rise; in essence using the heating value of the fuel to calculate the temperature rise per unit of mass burned.

Controlling the burn rate of the cool-flame reaction required a Wiebe function of the following form:

$$1 - \exp(-a(\frac{\theta - \theta_i}{\Delta\theta})^{m+1}) \qquad \text{(Equation 38)}$$

Where *a* and *m* are constants,  is the current CAD, $_i$ is the CAD at which the cool-flame auto-ignition occurs and Δ  is the burn duration. Literatue indicates a = 5, m =2 [42] while a burn duration (Δ ) of 2 CAD was chosen as an appropriately short burn duration.

A value for cool-flame burn-duration could only be estimated as there was no cool flame observed during experimental testing and no literature was found describing the cool-flame burn duration in such an engine using n-heptane. The same problem was encountered in estimating the burn duration of the main heat release. In this case the burn duration was set based on values observed during engine testing.

A Wiebe-function mimics the shape of the curve describing mass-fraction burned during combustion as cylinder contents proceed from reactants to products. To validate the suitability of a Wiebe-function, the actual mass-fraction burned curves from experimental data were compared to the shape of the Wiebe-function described by equation 38. It was found that using a=5 and m=2 fitted the burn characteristics well so long as an appropriate burn duration was used.

Below is a trace comparing a Wiebe function to calculate mass-fraction burned and data from a real engine test (constant load point, 14x8 5063rpm):

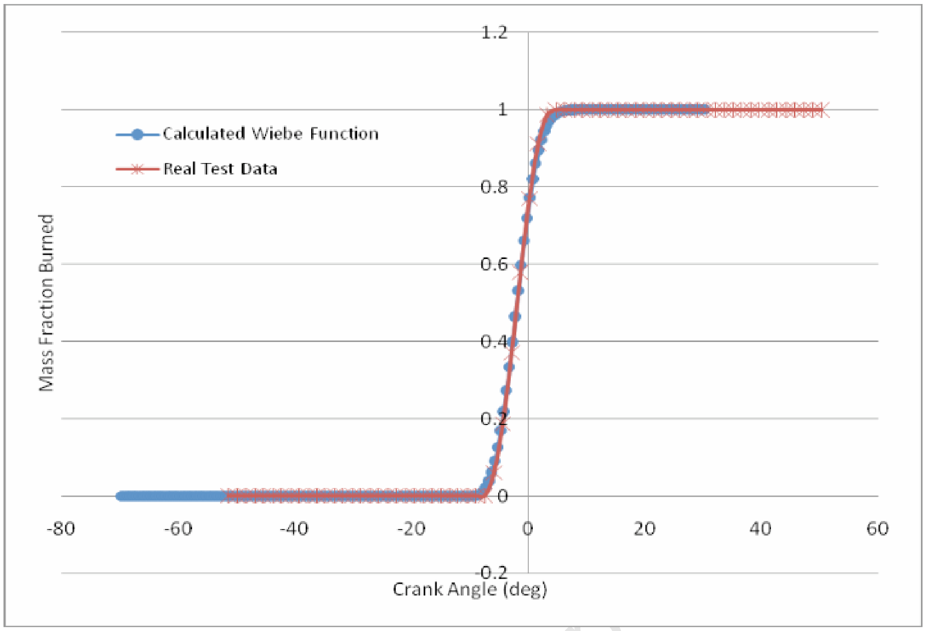

Figure 48: Wiebe-function vs real test-data.

## Main Heat Release

The ignition delay of the main heat-release was calculated in a similar fashion to the cool flame heat release although there is some modification to its form during the cool flame (to account for the cool-flame temperature rise). In addition, the empirical constants used for the main heat-release analysis are different to those for the cool-flame evaluation.

Pre cool-flame: $\tau_{MAIN} = \Phi^{B_h} \times A_h \times P_{cyl}{}^{n_h} e^{\frac{B_h}{T_{cyl}}}$ (Equation 39)

At cool-flame: $\tau_{MAIN} = \Phi^{B_h} \times A_h \times P_{cyl}{}^{n_h} e^{\frac{B_h}{T_{cyl}+X\Delta T_{CF}}}$ (Equation 40)

Where X = 1.5 for the cool flame enhancement factor [14]

Similarly, the main heat release begun once the following integral reached unity as evaluated from EVC to the current CAD step:

$$\int_{t_{EVC}}^{t_{current}} \frac{dt}{\tau_{MAIN}} \rightarrow 1 \qquad \text{(Equation 41)}$$

The formulation of the model allowed for the possibility where the main heat release could begin without any prior cool-flame taking place due to the fact that the main ignition delay runs parallel to the cool-flame ignition delay (as required by the auto-ignition model anyway).

A Wiebe function of the same form as described previously was used for the main heat release with the burn duration modified to $15^{\circ}$ CAD.

## 6.3. COMBUSTION MODELLING RESULTS

None of the simulated points achieved auto-ignition running with the same operating as those achieved during engine testing. This was not surprising and partially attributed to the significantly lower cetane rating of n-heptane compared to D1000. While this result was expected, a combustion model without combustion could not provide any insight into the auto-ignition responses of the engine to varying operating conditions.

It was also noted that the end-of-compression pressures for the simulated points were much lower than for the engine test-data. Upon further examination, it appeared that the compression ratio might have been measured incorrectly resulting in an underestimation of the actually compression ratio. Supporting this theory were the measured values of the end-of-compression pressures, which these averaged approximately 35bar depending on the operating conditions. Based on the EVC conditions and a polytropic compression model, it was estimated that the actual compression ratio should have been approximately 15:1 instead of ~12:1 as measurements had indicated. Using a compression ratio of 15:1 yielded more realistic end-of-compression pressure values for the combustion simulation.

Therefore it was decided that using a CR of 15:1 would provide a better representation of the pressure and temperature history of the in-cylinder gasses (and more accurately reflect their effect on the auto-ignition delay) even if it meant slightly compromising the accuracy of the CFD results (which were based on a compression ratio of 12:1) as it was not possible to run the CFD data points again.

Like the engine testing, the numerical modelling was split up into three sections with three points modelled for each section:

- Constant Speed: to test the effects of load on combustion phasing
- Constant Load: to test the effects of speed on combustion phasing
- Natural Compensation Abilty: to test the combined effect on combustion phasing of simultaneously varying the load and speed along a fixed speed-load profile

### 6.3.1. Constant Speed

Below is a graph showing the pressure traces of the simulated points and a table showing the start of combustion, the peak pressure and its location.

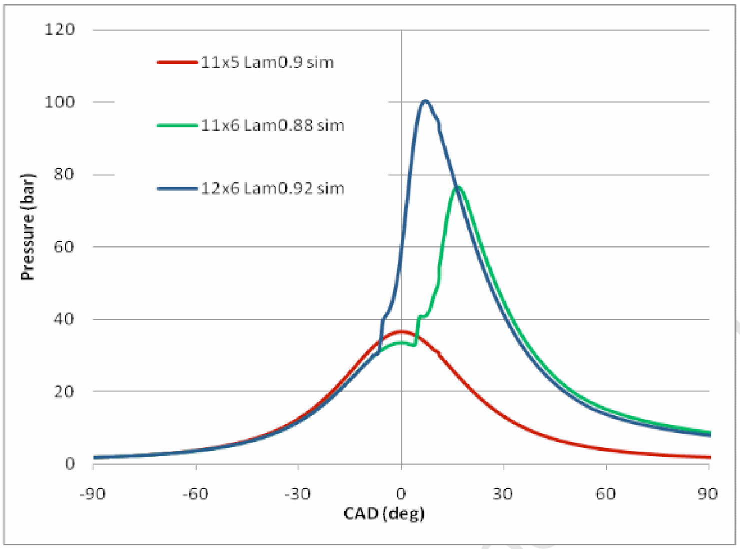

**Figure 49:** Pressure traces of Constant Speed simulations. Larger sized propellers indicate large loads.

Note how combustion phasing is retarded as load decreases to the point where the lowest-load point (red trace) did not achieve auto-ignition. Note also how all combusting traces show a clear cool flame-related pressure rise preceding the main heat-release pressure rise.  The data from the simulation follows the same trend in combustion phasing as the engine test data.

**Table 23**: Results from the "Constant-Speed" simulation compared to engine test-data.

| **Propeller** | **11x5** | | **11x6** | | **12x6** | |
|---|---|---|---|---|---|---|
| **Speed (rpm)** | **6880** | | **7110** | | **7042** | |
| **Fuel** | n-heptane | D1000 | n-heptane | D1000 | n-heptane | D1000 |
| **MFB 1% (CAD)** | - | 3.7 | ~3.5 | ~1.5 | ~-7 | ~3.5 |
| **Max Cyl Pressure** | 36.7 | 37.1 | 76.6 | 43.1 | 100 | 64.5 |
| **50% MFB (CAD)** | - | 18.6 | 11 | 10.6 | 0.5 | 1.1 |

The simulated point, 11x5 – 6880rpm, did not achieve combustion and thus has no combustion data from the simulation. It was found that the n-heptane followed the trends observed in the engine tests in that combustion phasing was retarded as load decreased (to the point of misfire for the lowest load-point). The simulation also showed a much greater sensitivity to load than the real engine with the low load point showing more retarded phasing (to the point of not combusting) and the high load point showing greatly advanced timing.

### 6.3.2. Constant Load

Below is a graph showing the pressure traces of the simulated points and a table showing the start of combustion, the peak pressure and its location. Note how combustion phasing is advanced as speed decreases. Note also how the traces show a clear cool flame-related pressure rise preceding the main heat-release pressure rise. Note also that the simulated data follows the same trend for combustion phasing as the engine test-data.

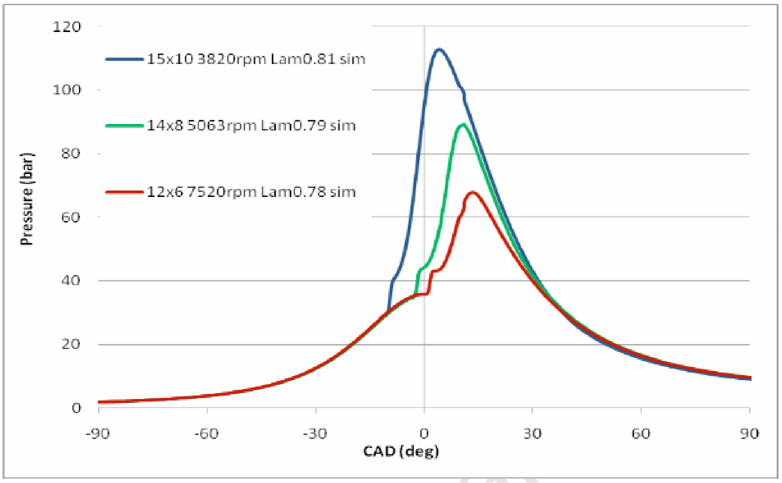

**Figure 50:** Pressure traces of Constant Load simulations where EVC $\Delta T = +30^oC$.

**Table 24**: Results from the "Constant-Load" combustion simulation (EVC $\Delta T = +30^oC$) compared to engine test-data.

| **Propeller** | **12x6** | | **14x8** | | **15x10** | |
|---|---|---|---|---|---|---|
| **Speed (rpm)** | **7520** | | **5063** | | **3820** | |
| **Fuel** | n-heptane | D1000 | n-heptane | D1000 | n-heptane | D1000 |
| **MFB 1% (CAD)** | ~0.5 | ~0.9 | ~-3 | ~-7 | ~-10.5 | ~-12 |
| **Max Cyl Pressure** | 67.8 | 65.0 | 89.2 | 75.4 | 112.8 | 94.6 |
| **50% MFB (CAD)** | ~7.5 | ~4 | ~4 | ~-2 | ~-3 | ~-8.5 |

The "Constant-Load" simulation showed the same trends in combustion phasing as observed in the engine-tests. This simulation initially posed a problem in that the simulated points displayed greatly retarded timing compared to the engine tests and were of little use as an investigation. Increasing the EVC cylinder temperature by a fixed amount, ΔT, for all the test points provided a means of artificially shortening the ignition delay. This method also artificially introduced energy (in the form of heat) into the system and therefore compromised the accuracy of the results predicted by the simulation. This was deemed acceptable as the model was being used to investigate trends in combustion phasing which were not compromised by the constant EVC ΔT modification. In this case the simulation also lacked the phasing sensitivity displayed in the other simulations (perhaps because the ΔT modification was not used in the other simulations).

### 6.3.3. Natural Compensation Ability

Below is a graph showing the pressure traces of the simulated points and a table showing the start of combustion, the peak pressure and its location. Note the combustion phasing which is virtually identical for two of the points (blue and green traces). Note also how the traces show a clear cool flame-related pressure rise preceding the main heat-release pressure rise.

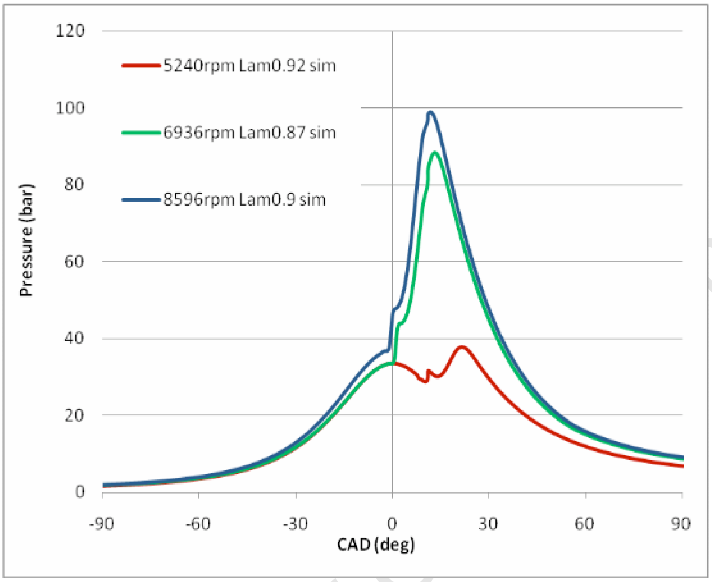

**Figure 51:** Pressure traces of Natural Compensation Ability simulations.

**Table 25**: Results from the "Natural Compensation Ability" combustion simulation compared to engine test-data.

| Propeller | 12x6 | | 12x6 | | 12x6 | |
|---|---|---|---|---|---|---|
| Speed (rpm) | 5240 | | 6936 | | 8596 | |
| Fuel | n-heptane | D1000 | n-heptane | D1000 | n-heptane | D1000 |
| MFB 1% (CAD) | ~9,5 | 8.7 | 0 | 2.5 | -1.5 | 3.1 |
| Max Cyl Pressure | 37.8 | 32.9 | 88.3 | 40 | 98.9 | 57.6 |
| 50% MFB (CAD) | ~16.5 | ~19 | ~7.5 | ~13 | ~6 | ~11 |

The final investigation showed that even when using a different fuel, n-heptane, the engine does indeed have some natural-compensation ability. The slowest, lowest-load, point did not show similar phasing to the other two points and again the simulation showed greater phasing sensitivity than the real engine.

## 6.4. DISCUSSION OF COMBUSTION MODELLING RESULTS

Unfortunately the available fuel data only allowed for the modelling of the combustion behaviour of n-heptane. Apart from the differences in cetane, burn duration and cool-flame behaviour, not much else was known about the differences in combustion performance. The largest discrepancies in the performance of the simulation were attributed to the different auto-ignition properties of the fuels.

For example:
- n-heptane showed consistently higher peak-pressures
- n-heptane's burn characteristics were fixed whereas D1000 had varying burn-characteristics depending on the operating conditions.
- n-heptane also showed a greater combustion-phasing sensitivity to changes in operating conditions than D1000

The higher peak pressures of n-heptane were attributed to a lack of modelling the effect of castor oil which was thought to lower the performance of D1000 (due to the fact that it appeared not to participate in combustion and exited the exhaust as a liquid – this would require the combusting components to heat up the relatively inert lubricant). A lower magnitude heat release due to a lower combustion-related pressure rise would explain the lower measured peak pressures for D1000 compared to the n-heptane simulations.

As n-heptane had a significantly lower ignition quality than D1000 it was suspected that n-heptane would exhibit a significantly retarded start-of-combustion. While this was generally found to be the case, n-heptane showed slightly advanced CAD positions for 1% MFB for highest-load points in the "Constant Speed" and "Natural Compensation" simulations. The advanced timing for n-heptane in the "Constant Load" Simulation was attributed to the increased EVC temperature applied to the model to achieve auto-ignition. It was surprising then that for the "Natural Compensation" testing, n-heptane showed similar timing to D1000.

It should be noted that the "EVC-$\Delta$T" method of artificially initiating auto-ignition was not used in the "Constant Speed" simulation despite the fact that the lowest-load point did not achieve combustion. In this case, increasing the EVC-$\Delta$T temperature increased the combustion phasing sensitivity of n-heptane and the lowest load point would have required an EVC-$\Delta$T increase of approximately $40^{o}$C even to achieve very late combustion phasing.

A significant weakness of the autoignition model was its inability to adequately deal with the effects of the high level of trapped exhaust residuals found in the engine. While this factor was considered in the combustion chemistry, it was not included in the fundamental ignition delay model. Only its effect on temperature and gas composition was incorporated into the combustion model. As the engine uses high levels of trapped exhaust residuals as a means of controlling combustion-phasing, this aspect should be included in any further work.

Despite the difficulties involved in using a different fuel, the combustion simulation agreed with the trends observed in engine testing. The simulated engine showed responses in combustion phasing which mimicked the real engine. Most notably, however, was that the simulation managed to capture some of the natural-compensation ability observed in engine testing.

# 7. CONCLUSIONS AND SUGGESTED FURTHER WORK

## 7.1. PROPELLER LOAD-SPEED CHARACTERISTICS

- The numerical model under-predicted the load-speed performance of the propellers, but was still a useful tool in guiding the design of the propeller testing rig.
- The propeller characterisation rig successfully mapped the load-speed curves of a suitable variety of propellers.
- Combining the information from the propeller testing rig with the proposed method of tuning the engine for maximum propeller speed provided a useful method of optimising combustion phasing (and overall engine setup).
- It was possible to accurately determine the load from a particular speed measurement and in that manner test the engine at specific load and speed-points.

Utilising propellers as a load proved to be one of the greatest benefits of the test set-up. Initially conceived as a simpler means of testing the engine at a particular load and speed (rather than using an engine dynamometer), the most useful feature was that tuning the engine for maximum speed also meant tuning for maximum power (and hence optimal phasing). This quickly became the defining feature of this test-method and provided an immensely useful, yet simple means of quickly optimising the many operating variables of the engine.

The balance-beam setup used for calibrating the propellers' speed-load profiles proved to be a useful tool for determining the desired propeller characteristics and provided a much more cost-effective solution than more complex ideas (such an electronic load cell instead of balanced weights) without any notable drawbacks. The rig's usefulness and suitability as model-aero propeller calibration tool is ultimately only limited by the speed and power range of the electric motor.

The numerical model was not re-visited after physically calibrating the propellers as it was not an efficient use of time to do so. The underlying method has been well established so it would be expected to produce better results with better input information about the propellers.

## 7.2. FUEL RELATED TESTING

- IQT$^{TM}$ testing of the fuel revealed the cetane blending effects of each component
- While the D1000 fuel did not show any favourable HCCI-enabling characteristics, the fuel is well-suited to the model-aero engine, particularly the components diethyl-ether and isopropyl-nitrate which together provide excellent vaporisation and very high ignition quality.

- The Castor oil was shown to have little effect on ignition quality and combustion characteristics of the fuel blend with a significant portion passing unburned into the exhaust. Testing in the Ricardo E6 showed that it detracted slightly from the autoignition stability of the fuel.

These results suggest that any fuel with suitable properties (vaporisation, ignition quality, lubrication etc.) could be made to run in a suitable HCCI-engine over a wide range. These results also verify the sensitivity of HCCI engine to correct fuels and the importance of the correct fuels as enablers of HCCI technology.

Initially it was hoped that the test-fuels (and components) could be investigated in a rapid-compression machine (RCM) although this was not possible. It is therefore recommended that any further fuels investigation pursue testing in an RCM which would represent homogeneous (HCCI-type) combustion much better than the diesel-like IQT$^{\text{TM}}$.

## 7.3. ENGINE TESTING

- With proper adjustment, the engine exhibited no signs of undesirable combustion behaviour (knock, noise from excessive heat release rate or misfiring) over its full operating range
- The levels of BMEP achieved were slightly higher than those observed in previous studies using similar engines
- No two-stage combustion phenomena were observed in the model-aero engine although two-stage ignition was observed for the same fuel in the Ricardo E6 engine. This is attributed to the vastly different compression ratios, heat loss characteristics and operating speeds of the two engines and their effect on pressure-temperature histories in conjunction with the auto-ignition behaviour of the fuel.
- Fixing the compression ratio of the engine (to ~15:1) limited lower speed maximum power operation due to knocking. This compression ratio was also not high enough to produce maximum power at high speed operation.
- Maximum power for all the tested propellers was achieved using the leanest possible air-fuel ratio while still avoiding the lean-misfire limits.
- The engine exhibited constant combustion phasing along the standard load-speed profile despite changes in both load and speed (and their respective opposing effects on combustion phasing).

The engine's defining feature was its versatility due to a variable compression ratio. This allowed the operator sufficient adjustability so as to ensure correct combustion phasing over greatly varying load and speed range. Fixing the compression ratio of the engine significantly limited the upper speed limits of the operating range, suggesting that more than any other factor, variable CR is a useful enabler in increasing the operating range of HCCI engines.

While the engine's operating range represented its knock-free performance envelope, the engine was not immune to knock. The tested operating range also does not represent the entire possible (theoretical) operating range due to the limited availability of propellers and the safe maximum running speed recommended by the manufacturer. It is suspected that both the ultimate upper load range and ultimate upper speed range will both be limited by compression ratio. The eventual load limit will likely be limited by a CR which is both low enough to avoid knock, yet high enough to initiate autoignition with the correct combustion phasing. If not limited by con-rod strength, the eventual high speed limits may be limited by a CR which is both high enough to provide the correct phasing (appropriately advancing phasing to compensate for the higher speed), yet low enough to avoid the geometric limits of the engine (thus avoiding the piston striking the head at TDC).

The PAW-40 engine, rather than having some anomalous characteristic which enabled HCCI operation, merely represents a simple implementation of HCCI combustion. Engine testing revealed that combustion phasing responded to changes in operating conditions in a manner consistent with classical HCCI engine operation. When viewed in isolation, those effects are not unusual, but a combination thereof results in the unusual capability of an HCCI which is inherently able to run over a wide range of loads and speeds without complex control systems.

Not surprisingly, the engine performed best (good performance with good transient ability) using the recommended propeller and using only the throttle to simultaneously adjust load and speed (as apposed to trying to keep AFR constant by continuously adjusting the AFR needle for example). Testing the engine showed that the combustion phasing was kept approximately constant by balancing the conflicting effects of decreasing speed and decreasing load. Perhaps most of all, this was the most significant finding as naturally-occurring constant combustion phasing would provide a means of operating an engine in HCCI mode over a broad range without complex control strategies.

The engine tests successfully investigated many important performance factors, but the study was constantly plagued by equipment failure due to the harsh test conditions (eg. vibration, solvents, high temperatures, etc). The original test-rig was not intended for the type of extended testing required by this study. For example, the temperature-controlled water supply provided a source of constant problems (due to materials which were ill-suited to the high-temperature environment). In addition, the performance of certain aspects could have been improved upon if all the individual components were designed together rather than added as the need arose (due to the exploratory nature of the study). The engine's small size also provided a substantial challenge in correctly placing the necessary instrumentation, often resulting in compromised functionality.

The single largest weakness of the test set-up was the measurement of the compression ratio. The available method was cumbersome and inconsistent as a result. The uncertainty over the actual compression ratio introduced an unnecessary level of inaccuracy into the study.

It is recommended that any further investigation utilise a micrometer-type means of measuring the compression ratio and/or use a larger engine to facilitate better placement of the required instrumentation. Utilising a larger engine might also allow for the use of fuel-injection instead of a carburettor, thus allowing for better AFR control.

A factor which was not exhaustively investigated was the impact of the size-effect on the engine's operating characteristics. Comparing the E6 and PAW engine tests revealed only that D1000 exhibited two-stage behaviour in the larger, slower E6-engine whereas the same fuel showed single-stage combustion in the smaller, faster PAW engine. There were too many differences in operating conditions (inlet temp, CR, speed, AFR, breathing arrangement etc.) which could affect the AI characteristics of the fuel. The only conclusion was that the pressure and temperature history of the fuel accessed by the PAW engine was sufficiently different to avoid the NTC region of the fuel.

It should be noted that the excellent performance of the castor-oil trap also provided a simple means of accurately determining the AFR by allowing the use of a lambda sensor in a two-stroke engine (without resorting to more complex and expensive commercial filter-based systems).

## 7.4. ENGINE MODELLING

- The CFD model showed significant thermal stratification.
- It also reproduced the observed fresh-charge in-homogeneities inside the cylinder due the port layout as validated by the burn marks observed on the head.
- The in-homogeneous fresh-charge distribution and temperature profiles have a significant effect on the auto-ignition and 'cascading combustion" dynamics in the model aero-engine and likely contribute to the conservative pressure rise rates and knock resistance of this engine.
- Despite using a different fuel, the EXCEL combustion simulation reproduced the trends in combustion phasing found during engine testing at constant load and constant speed.
- The combustion simulation also displayed some "natural-compensation" ability displayed by the engine (for maintaining constant phasing over a variety of operating conditions).

The CFD model provided useful insight into the flow conditions inside the cylinder, but was perhaps not fully exploited due to the limited scope of the investigation and available time. The initial investigation revealed aspects which could have a beneficial effect on characteristics by influencing the autoignition delay and heat release rates, but the actual magnitude of these effects was not investigated due to the lack of a CFD-based combustion model.

The EXCEL combustion simulation showed similar trends to those observed in data from engine-testing, although the use of n-heptane made a direct comparison impossible. The accuracy of the model could also not be determined due to the different fuel. It would therefore be beneficial to test n-heptane-based blend in the model-aero engine and compare those results to numerical modelling results.

## 7.5. GENERAL COMMENTS

The PAW-40 engine possessed critical features which were instrumental in enabling HCCI operation over the observed range and allowed flexible, transient operation. In understanding the underlying reasons for the engine's observed performance capabilities and operating characteristics, the following factors were the most important:

- Correct Fuel

The D1000 fuel-blend was particularly well-matched to the requirements of the engine and operating conditions perhaps due to it being a niche fuel used solely in this type of engine. While not usually a changeable variable (as most vehicles run on a single fuel), the use and consideration of a suitable fuel (or suitable fuel characteristics) is as important as the engine design. Correctly matching an engine's design features to the combustion characteristics of the fuel may avoid many of the problems associated with HCCI-operation instead of trying to accommodate these problems (or their effects) requiring complex control systems.

- Variable Compression Ratio

The ability to vary compression ratio was the single greatest factor in enabling HCCI-operation over the observed range. It provided a primary means of adjustment for correcting combustion phasing thereby significantly extended the operating range of the engine.

- Inherent Ability To Maintain Appropriate Combustion Phasing

The balanced effects (of load and speed on combustion phasing) from using a conventional throttle resulted in approximately constant combustion phasing, despite varying the engine's load and speed. These features resulted in inherently good transient operability and a broad operating range without the need for complex control systems.

While the PAW-40 engine may be limited in its application, the characteristics investigated by this study have shown which universal engine features can be used successfully as an effective means of addressing the combination of problems traditionally associated with HCCI-operation.

Classical HCCI engines do not readily show the “natural compensation” observed in this study. It would, however, be possible to implement this phenomenon in the more common research engines currently under development. The PAW engine utilises trapped exhaust residuals, inlet throttling and crank-case scavenging to autonomously vary the in-cylinder conditions to match the requirements of the operating conditions. There is also some mixture adjustment although this does not achieve optimal results (but does allow the engine run over a wide range with only the throttle used to adjust load and speed).

Strictly, one would not want to use inlet throttling on an HCCI engine as this decreases volumetric efficiency. It would, however be possible to control the amount of exhaust residuals and fresh-charge inducted into the cylinder by using variable valve lift and variable valve timing. At low loads, more exhaust residuals could be trapped by opening the exhaust valve later and closing it earlier while less fresh charge could be inducted by decreasing the valve lift and/or duration during the intake stroke. This could also emulate the PAW engine’s system by not affecting the start-of-compression pressure (as throttling would).

It would be much harder to emulate the flow regimes observed in the CFD analysis of the PAW engine which are a function of the side-ported, two-stroke layout of the engine. It might be possible to control the flow of incoming fresh charge in much the same way as current direct injection petrol engines.

# *8. References and Other Sources*

1. Swihart JM, “*Experimental and Calculated Static Characteristics of a two-blade NACA 10-(3)(062) -045 Propeller”*, *National Advisory Committee for Aeronautics*, 1954
2. Diehl WS, “*Report 447 Static Thrust of Airplane Propellers”*, *National Advisory Committee for Aeronautics*, (Date not Published)
3. Auld DJ and Srinivas K, *“Aeronautics for Students”, section: Blade Element Propeller Analysis,* AMME University of Sydney, 1996-2006
4. U.S. Department of Energy - Office of Transportation Technologies, “*Homogeneous Charge Compression Ignition (HCCI) Technology”*, April 2001*,* p. 11
5. Heywood JB, “*Internal Combustion Engine Fundamentals”*, McGraw-Hill Singapore, 1988, p.16
6. Blakeman, Chiffy, Phillips, Twigg and Walker, “*Development in Diesel Emissions Aftertreatment Technology”*, *SAE* 2003-01-3753
7. Heywood JB*, “Internal Combustion Engine Fundamentals”*, McGraw-Hill Singapore, 1988, p. 572
8. Heywood JB, “*Internal Combustion Engine Fundamentals”*, McGraw-Hill Singapore, 1988, p. 626
9. Heywood JB, “*Internal Combustion Engine Fundamentals”*, McGraw-Hill Singapore, 1988, p. 492
10. Onishi S, Hong Jo S, Shoda K, Do Jo P, Kato S, “*Active Thermo-Atmosphere Combustion (ATAC)-A New Combustion Process for Internal Combustion Engine”s*, *SAE* paper 790501
11. Ishibashi Y, “*Basic Understanding of Activated Radical Combustion and its Two-Stroke Engine Application and Benefits”*, *SAE* paper 2000-01-1836
12. Zhao F, Dennis N. Assanis DN, Najt PM, Dec JE, Eng JA, Asmus TN, (2003), “*Homogeneous charge compression ignition (HCCI) engines: key research and development issues”*, 1st edition, Warrendale, PA, *Society of Automotive Engineers,* p. 327
13. Martinez-Frias J, Aceves SM, Flowers D, Smith JR, Dibble R, “*HCCI Engine Control By Thermal Management”*, SAE International, Paper Submitted to 2000 SAE Conference in Baltimore
14. Johansson B, Tunestal P, Manente V, “*Mini High Speed HCCI Engine Fuel with Ether: Load Range, Emission Characteristics and Optical Analysis”*, *SAE International*, 2007-01-3606
15. Yates ADB and Viljoen CL, “*An Improved Model for Describing Auto-Ignition”*, *SAE International*, 2008-01-1629
16. AI Kohtaro Hashimoto, “*Effect of Ethanol on the HCCI Combustion”*, *SAE* 2007-01-2038
17. Viljoen, C.L., Yates, A.D.B., Swarts, A., Balfour, G., Möller, K, “*An Investigation of the Ignition Delay Character of Different Fuel Components and an Assessment of Various Autoignition Characteristics”*, *SAE International*, 2005-01-2084
18. Owen K and Coley T, “*Automotive Fuels Handbook”*, *SAE Inc USA*, 1990*,* p. 229

19. Bunting B, Szybist JP, "*Cetane Number and Engine Speed Effects on Diesel HCCI Performance and Emissions", SAE* 2005-01-3723
20. Heywood JB, "*Internal Combustion Engine Fundamentals"*, McGraw-Hill Singapore, 1988, p. 375
21. Bengttson J, "*Closed Loop Control of HCCI Engine Dynamics"*, Media Tryck Sweden, 2004
22. Zhao F, Dennis N. Assanis DN, Najt PM, Dec JE, Eng JA, Asmus TN, (2003), "*Homogeneous charge compression ignition (HCCI) engines: key research and development issues"*, 1st edition, Warrendale, PA, *Society of Automotive Engineers*, p.325
23. ASTM Standard D6890-04, "Standard Test Method for Determination of Ignition Delay and Derived Cetane Number of Diesel Fuel Oils by Combustion in a Constant Volume Chamber", ASTM International, 2004
24. Lemberger I, "HCCI Engine Investigation" (undergraduate research project), University of Cape Town, 2006
25. Andy D. B. Yates, Carl Viljoen and Owen Metcalf, "*An Accurate Determination of the Cetane Number Value of GTL Diesel"*, *SAE* 2007-01-0026
26. Ryan T Matheaus A, "*Fuel Requirements for HCCI Engine Operation"*, *SAE International*, 2003-01-1813
27. Shoji H, Yoshida K, Goto K, Iijima A, "*Analysis of the Characteristics of HCCI Combustion and ATAC Combustion Using the Same Test Engine"*, *SAE Japan*, 2004-32-0097
28. Aberg E, "*HCCI 2-stroke – Study of HCCI in a Model Engine (title translated from Swedish)"*, 2001
29. Chang H, Zhang L and Chen L, "*An Applied Thermodynamic Method for Correction of TDC in the indicator diagram and its experimental confirmation"*, *Applied Thermal Engineering* ,Volume 25, Issues 5-6, April 2005
30. Johansson B, Tunestal P, Manente V, "*A Study of a Glow Plug Ignition Engine by Chemiluminescence Images"*, *SAE International*, *SAE* 2007-01-1884
31. Johansson B, Tunestal P, Manente V, "*Influence of Inlet Temperature and Hot Residual Gases on the Performance of a Mini High Speed Glow Plug Engine"*, *SAE International*, 2006-32-0057
32. Sjöberg and Dec, "*Effects of Engine Epeed, Fueling Rate and Combustion Phasing on the Thermal Stratification Required to Limit HCCI Knocking Intensity"*, *SAE International*, 2005-01-2125
33. Berntsson and Denbratt, "*HCCI Combustion using Charge Stratification for Combustion Control"*, *SAE International*, 2007-01-0210
34. Inagaki K, Ueda M, Akihama K, Kuzuyama H, Machida M, "*A Study on Natural Gas Fueled Homogeneous Charge Compression Ignition Engine - Expanding the Operating Range and Combustion Mode Switching"*, *SAE International*, 2007-01-0176
35. Floweday G and Yates DB, "*Integration of Fuel Auto-ignition Characteristics and HCCI Operation"*, *SAE International*, 08SFL-0201
36. Heywood JB, "*Internal Combustion Engine Fundamentals"*, McGraw-Hill Singapore, 1988, p. 678
37. Heywood JB*, "Internal Combustion Engine Fundamentals"*, McGraw-Hill Singapore, 1988, p.43

38. Heywood JB, "*Internal Combustion Engine Fundamentals"*, McGraw-Hill Singapore, 1988, p. 86
39. Heywood JB, "*Internal Combustion Engine Fundamentals"*, McGraw-Hill Singapore, 1988, p. 679
40. Heywood JB, "*Internal Combustion Engine Fundamentals",* McGraw-Hill Singapore, 1988, p. 92
41. Heywood JB, "*Internal Combustion Engine Fundamentals"*, McGraw-Hill Singapore, 1988, p. 87
42. Heywood JB, "*Internal Combustion Engine Fundamentals"*, McGraw-Hill Singapore, 1988, p. 390
43. Livengood JC, and Wu PC, "Correlation of Autoignition Phenomena in Internal Combustion Engines and Rapid Compression Machines", Fifth Symposium on Combustion, Reinholds Publishing Corp 1955

## OTHER SOURCES

- J van Leersum, **A numerical model of a high performance two-stroke engine,** Applied Numerical Mathematics, Issue 27 1998
- M. Bergman, R. U. K. Gustafsson and B. I. R. Jonsson, Emission and Performance **Evaluation of a 25 cc Stratified Scavenging Two-Stroke Engine**, SAE 2003-32-0047
- Hisatoshi Kinoshita and Yuh Motoyama, **The Relationship Between Port Shape and Engine Performance for Two-Stroke Engines**, SAE 1999-01-3333
- Nagesh S. Mavinahally, **An Historical Overview of Stratified Scavenged Two-Stroke Engines – 1901 through 2003**, SAE 2004-32-0008 / 20044295
- Diego A. Arias and Timothy A. Shedd, **Numerical and Experimental Study of Fuel and Air Flow in Carburetors for Small Engines**, SAE 2004-32-0053 / 20044340
- **AVL DITEST catalogue**, 2006
- Joseph MCDONALD, John MENTER, Jane ARMSTRONG, Jitendra SHAH, **Evaluation of Emissions from Asian 2-strokeMotorcycles**, 2005-32-0114 (SAE)
- J. W. G. Turner, R. J. Pearson, B. Holland and R. Peck, **Alcohol-Based Fuels in High Performance Engines**, SAE 2007-01-0056
- Pär Bergstrand**, Effects on Combustion by Using Kerosene or MK1 Diesel**, SAE 2007-01-0002
- H. T. Aichlmayr1, D. B. Kittelson, M. R. Zachariah, **Micro-HCCI combustion: experimental characterization and development of a detailed chemical kinetic model with coupled piston motion**, Combustion and Flame 135 (2003) 227–248

- Dec JE, **Understanding HCCI Charge Stratification Using Optical, Conventional and Computer Diagnostics**, SAE HCCI symposium Lund Sweden, 2005
- Magnus Sjöberg and John E. Dec, **EGR and Intake Boost for Managing HCCI Low-Temperature Heat Release over Wide Ranges of Engine Speed**, SAE 2007-01-0051
- Magnus Sjo¨berg, John E. Dec, **Comparing late-cycle autoignition stability for single- and two-stage ignition fuels in HCCI engines**, Proceedings of the Combustion Institute 31 (2007)
- Aaron Oakley, Hua Zhao, Fabian Mauss, Amit Bhave, Markus Kraft, **Evaluating the EGR-AFR Operating Range of a HCCI Engine**, SAE 2005-01-0161
- H Ma, K Kar, R Stone, R Raine, and H Thorwarth, **Analysis of combustion in a small homogeneous charge compression assisted ignition engine**, Int. J. Engine Res. Vol. 7, JER03805 2006
- Cengel Y and Boles M, **Thermodynamics 4th Edition**, McGraw-Hill, 2002
- Ebbing and Gammon, **General Chemistry 6th Edition**, Houghton Mifflin, 1999

# *9. APPENDICES*

## 9.1. GLAUERT BLADE ELEMENT THEORY SIMULATION INSTRUCTIONS REPRODUCTION FROM TEXT BY AULD AND SRIVIVAS [11]

### Blade Element Subdivision

A propeller blade can be subdivided as shown into a discrete number of sections.

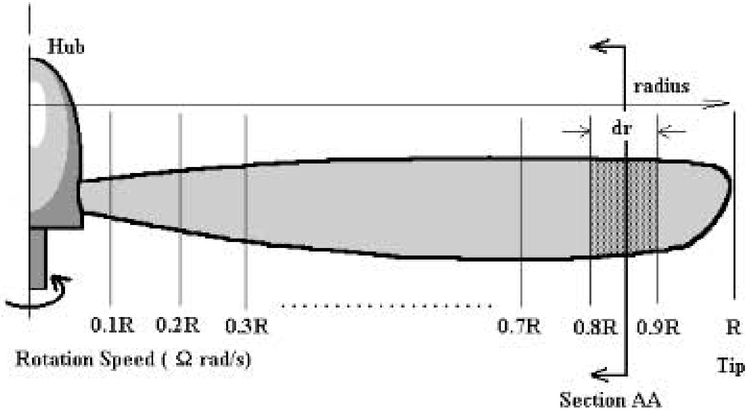

For each section the flow can be analysed independently if the assumption is made that for each there are only axial and angular velocity components and that the induced flow input from other sections is negligible. Thus at section AA (radius = r) shown above, the flow on the blade would consist of the following components.

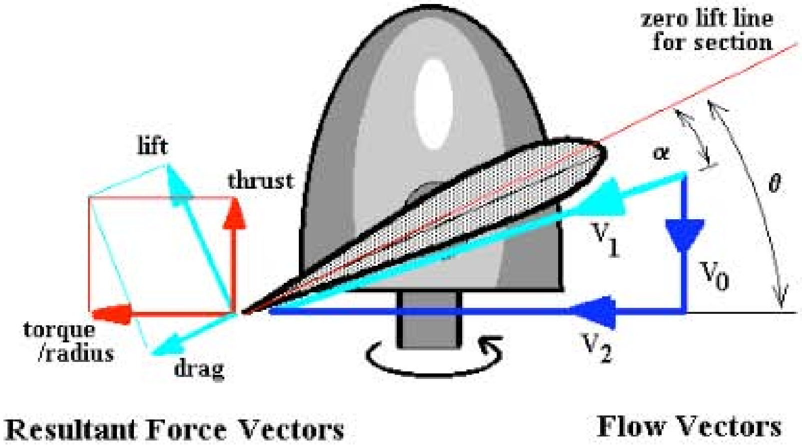

$V_0$ -- axial flow at propeller disk, $V_2$ -- Angular flow velocity vector

$V_1$ -- section local flow velocity vector, summation of vectors $V_0$ and $V_2$

Since the propeller blade will be set at a given geometric pitch angle ($\theta$) the local velocity vector will create a flow angle of attack on the section. Lift and drag of the section can be calculated using standard 2-D aerofoil properties. (Note: change of reference line from chord to zero lift line). The lift and drag components normal to and parallel to the propeller disk can be calculated so that the contribution to thrust and torque of the compete propeller from this single element can be found.

The difference in angle between thrust and lift directions is defined as

$$\phi = \theta - \alpha$$

The elemental thrust and torque of this blade element can thus be written as

$$\Delta T = \Delta L \cos(\phi) - \Delta D \sin(\phi) \quad , \quad \frac{\Delta Q}{r} = \Delta D \cos(\phi) + \Delta L \sin(\phi)$$

Substituting section data ($C_L$ and $C_D$ for the given $\alpha$) leads to the following equations.

$$\Delta L = C_L \tfrac{1}{2}\rho V_1^2 c.dr \quad , \quad \Delta D = C_D \tfrac{1}{2}\rho V_1^2 c.dr_{\text{per blade}}$$

where $\rho$ is the air density, c is the blade chord so that the lift producing area of the blade element is c.dr.

If the number of propeller blades is (B) then,

$$\Delta T = \tfrac{1}{2}\rho V_1^2 c(C_L \cos(\phi) - C_D \sin(\phi)).B.dr \quad \ldots\ldots\ldots(1)$$

$$\frac{\Delta Q}{r} = \tfrac{1}{2}\rho V_1^2 c(C_L \sin(\phi) + C_D \cos(\phi)).B.dr$$

$$\Delta Q = \tfrac{1}{2}\rho V_1^2 c(C_L \sin(\phi) + C_D \cos(\phi)).B.r.dr \quad \ldots\ldots\ldots(2)$$

**Inflow Factors**

A major complexity in applying this theory arises when trying to determine the magnitude of the two flow components $V_0$ and $V_2$. $V_0$ is roughly equal to the aircraft's forward velocity ($V_{inf}$) but is increased by the propeller's own induced axial flow into a slipstream. $V_2$ is roughly equal to the blade section's angular speed ($\Omega$r) but is reduced slightly due to the swirling nature of the flow induced by the propeller. To calculate $V_0$ and $V_2$ accurately both axial and angular momentum balances must be applied to predict the induced flow effects on a given blade element. As shown in the following diagram the induced flow components can be defined as factors increasing or decreasing the major flow components.

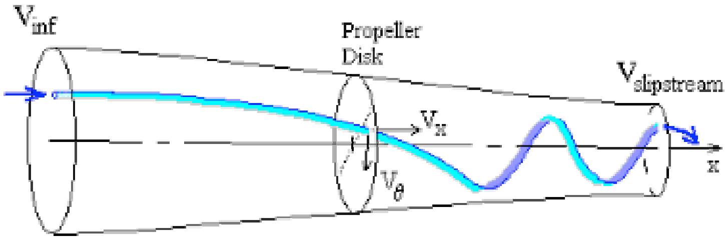

Typical Streamtube of flow passing through Section AA

$V_\theta = b\Omega r \qquad V_x = V_{inf}(1 + a)$

So for the velocities V0 and V2 as shown in the previous section flow diagram,

$V_o = V_{inf} + a.V_{inf}$ where a -- axial inflow factor

$V_2 = \Omega r - b.\Omega r$ where b -- angular inflow factor (swirl factor)

The local flow velocity and the angle of attack for the blade section is thus

$$V_1 = \sqrt{(V_o^2 + V_2^2)} \quad \ldots\ldots\ldots\ldots\ldots\ldots\ldots\ldots (3)$$

$$\alpha = \theta - \tan^{-1}(V_o/V_2) \quad \ldots\ldots\ldots\ldots\ldots\ldots\ldots\ldots (4)$$

**Axial and Angular Flow Conservation of Momentum**

The governing principle of conservation of flow momentum can be applied for both axial and circumferential directions.

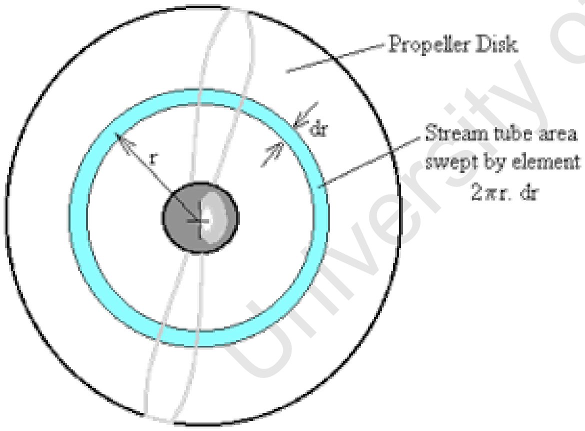

For the axial direction, the change in flow momentum along a stream-tube starting upstream, passing through the propeller at section AA and then moving off into the slipstream, must equal the thrust produced by this element of the blade.

To remove the unsteady effects due to the propeller's rotation, the stream-tube used is one covering the complete area of the propeller disk swept out by the blade element and all variables are assumed to be time averaged values.

$\Delta T$ = change in momentum flow rate

= mass flow rate in tube x change in velocity

$$= \rho 2 \pi r \, dr \, V_o (V_{slipstream} - V_{inf})$$

By applying Bernoulli's equation and conservation of momentum, for the three separate components of the tube, from freestream to face of disk, from rear of disk to slipstream far downstream and balancing pressure and area versus thrust, it can be shown that the axial velocity at the disk will be the average of the freestream and slipstream velocities.

$V_0 = (V_{inf} + V_{slipstream})/2$, that means $V_{slipstream} = V_{inf} (1 + 2a)$

Thus

$$\Delta T = \rho 2 \pi r V_{inf} (1+a). \left(V_{inf} (1+2a) - V_{inf}\right). dr$$

$$\Delta T = \rho 2 \pi r V_{inf}^{2} (1+a) .2 a.dr$$

$$\Delta T = \rho 4 \pi r V_{inf}^{2} (1+a). a.dr \quad \ldots\ldots\ldots (5)$$

For angular momentum

$\Delta$Q = change in angular momentum rate for flow x radius

= mass flow rate in tube x change in circumferential velocity x radius

$$\Delta Q = \rho 2 \pi r \, dr \, V_o . (V_\theta (slipstream) - 0 (freestream)). r$$

By considering conservation of angular momentum in conjunction with the axial velocity change, it can be shown that the angular velocity in the slipstream will be twice the value at the propeller disk.

$$V_\theta (slipstream) = 2 b \Omega r$$

Thus

$$\Delta Q = \rho 2 \pi r V_{inf} (1+a). (2 b \Omega r). r.dr$$

$$\Delta Q = \rho 4 \pi r^3 V_{inf}^{2} (1+a). b \Omega . dr \quad \ldots\ldots\ldots\ldots\ldots (6)$$

Because these final forms of the momentum equation balance still contain the variables for element thrust and torque, they cannot be used directly to solve for inflow factors.

However there now exists a nonlinear system of equations (1),(2),(3),(4),(5) and (6) containing the four primary unknown variables $\Delta$T, $\Delta$Q, a, b. So an iterative solution to this system is possible.

**Iterative Solution procedure for Blade Element Theory.**

The method of solution for the blade element flow will be to start with some initial guess of inflow factors (a) and (b). Use these to find the flow angle on the blade (equations (3),(4)), then use blade section properties to estimate the element thrust and torque (equations (1),(2)). With these approximate values of thrust and torque equations (5) and (6) can be used to give improved estimates of the inflow factors (a) and (b). This process can be repeated until values for (a) and (b) have converged to within a specified tolerance.

It should be noted that convergence for this nonlinear system of equations is not guaranteed. It is usually a simple matter of applying some convergence enhancing techniques (ie Crank-Nicholson under-relaxation) to get a result when linear aerofoil section properties are used. When non-linear properties are used, ie including stall effects, then obtaining convergence will be significantly more difficult.

For the final values of inflow factor (a) and (b) an accurate prediction of element thrust and torque will be obtained from equations (1) and (2).

**Propeller Thrust and Torque Coefficients and Efficiency.**

The overall propeller thrust and torque will be obtained by summing the results of all the radial blade element values.

$$T = \Sigma \Delta T \text{(for all elements), and } Q = \Sigma \Delta Q \text{(for all elements)}$$

The non-dimensional thrust and torque coefficients can then be calculated along with the advance ratio at which they have been calculated.

$$C_T = T/(\rho n^2 D^4) \text{ and } C_Q = Q/(\rho n^2 D^5) \text{ for } J = V_{inf}/(nD)$$

where n is the rotation speed of propeller in revs per second and D is the propeller diameter.

The efficiency of the propeller under these flight conditions will then be

$$\eta\text{(propeller)} = J/(2\pi).(C_T/C_Q).$$

## 9.2. MATLAB PROPELLER SIMULATION CODE

“Input_Variables.m” Program used to initialise the simulation:

```
clc
clear all

chord =  0.015; %chord section
pitch =  input('input pitch:  '); %prop standard pitch
dia = input('input diameter: '); %prop diameter
RPMmin = 2000; %min rpm
RPMmax = 14000; %max RPM
V = 0.01; %incoming air velocity(m/s)
Q1 = 1.01; %torque correction factor

T1 = 0.99; %thrust correction factor

in = [chord,pitch,dia,RPMmin,RPMmax,V,Q1,T1];
```

“Propel.m” Main Simulation:

```
function [tableout] = propel(in)

input_variables %call array of input conditions

chord = in(1); %chord section
pitch = in(2); %prop standard pitch
dia= in(3); %prop diameter
V = in(6); %incoming air velocity(m/s)
Q1 = in(7); %torque correction factor
T1 = in(8); %thrust correction factor

RPMmin = in(4);
RPMmax = in(5);

RPMS = (RPMmax - RPMmin)/500;
RPMnew = RPMmin;
RPM = RPMnew;
tableout = zeros(RPMS,7);

for z = 1 : (RPMS +1)

   R=dia/2; %radius = 1/2 diameter
   tip= atan(pitch/(2*pi*R))*57.29578; %pitch angle setting at tip
   xt=R; %x value at tip
   hub= atan(pitch/(2*pi*0.25*R))*57.29578; %pitch angle setting at 25% radius
```

```
 xs=0.1*R; %step size
 rho=1.225; %air density
 n=RPM/60; %n = revs/s
 omega=n*2*pi; %w = rad/s
 coef1=(tip-hub)/(xt-xs); %blade twist co-eff??
 coef2=hub-coef1*xs; %blade twist co-eff?
 rstep=(xt-xs)/10; %step length along radius
 r1=[xs:rstep:xt]; %step positions along radius
 eff0=0; %initialise efficiency to zero
 thrust=0; %initialise thrust to zero
 torque=0; %initialise torque to zero


for j=1:size(r1,2), %specific step -> running through from root to tip
    rad=r1(j); %x position from r1
    theta=coef1*rad+coef2+pitch; %blade angle
    t2(j)=theta; %adding theta to t2 array
    th=theta/180*pi; %theta in radians
    a=0.1; %axial inflow factor
    b=0.01; %angular inflow factor
    finished=0; %"stop" variable to say when to stop iteration
    sum=1; %iteration counter
    while (finished==0),
        V0=V*(1+a); %axial flow velocity at prop disk
        V2=omega*rad*(1-b); %angular flow velocity
        phi=atan2(V0,V2); %difference in angle between thrust and lift
        alpha=th-phi; %lift angle
        cl=6.2*alpha; %lift co-eff
        cd=0.008-0.003*cl+0.01*cl^2; %drag co-eff
        Vlocal=sqrt(V0*V0+V2*V2); %resultant velocity magnitute
        DtDr=0.5*rho*Vlocal*Vlocal*2.0*chord*(cl*cos(phi)-cd*sin(phi)); %element thrust
        DqDr=0.5*rho*Vlocal*Vlocal*2.0*chord*rad*(cd*cos(phi)+cl*sin(phi)); %element torque
        tem1=DtDr/(4.0*pi*rad*rho*V*V*(1+a)); %variable for new axial inflow factor
        tem2=DqDr/(4.0*pi*rad*rad*rad*rho*V*(1+a)*omega); %variable for new angular inflow factor
        anew=0.5*(a+tem1); %new axial inflow factor
        bnew=0.5*(b+tem2); %new angular inflow factor
        if (abs(anew-a)<1.0e-5), %if dif in axial inflow factor is too small, stop
            if (abs(bnew-b)<1.0e-5), %if dif in angular inflow factor is too small, stop
                finished=1; %stop iteration
            end;
        end;
```

```
            a=anew; %set new axial inflow factor
            b=bnew; %set new angular inflow factor
            sum=sum+1; %tick over iteration counter
            if (sum>500), %if iteration counter is too high, stop iteration
               finished=1; %stop iteration
            end;
         end;
         a2(j)=a; %add axial inflow factor to array
         b2(j)=b; %add angular inflow factor to array
         thrust=thrust+DtDr*rstep; %add thrust element to total amount of thrust
         torque=torque+DqDr*rstep; %add torque element to total amount of torque
      end;

      thrust = thrust * T1; %thrust correction
      torque = torque * Q1; %torque correction

      Ct=thrust/(rho*n*n*dia*dia*dia*dia); %calculate thrust co-eff
      Cq=torque/(rho*n*n*dia*dia*dia*dia*dia); %calculate torque co-eff
      P = 2*pi*n*torque; %calculate power
      Cp = P/(rho*n^3*dia^5); %calculate power co-eff
      RPMtab = RPM/1000;
      Ptab = P/100;
      out = [RPMtab,thrust,Ct,torque,Cq,Ptab,Cp];

      k = 1;
      for k = 1:7
         tableout(z,k) = out(k);
         k = k+1;
      end

      J=V/(n*dia);


      if (Ct<0),
      eff=0.
      else
      eff=Ct/Cq*J/(2.0*pi);
      end;

      RPMnew = RPMmin + 500*z;
      RPM = RPMnew;
   end

end
```

## 9.3. PAW ENGINE TESTING RESULTS TABLES

**Batch 1:**

| Prop | Speed | BMEP | Mix screw | CR |
|---|---|---|---|---|
| Xpitch | rpm | bar | turns open | |
| 1st batch | | | | |
| 11x5 | 9740 | 2.45 | 0.5-0.75 | 13.3 |
| 11x5 | 9803 | 2.48 | 0.5 | 13.3 |
| 11x5 | 10000 | 2.58 | 0.75 | 13.3 |
| 11x5 | 10274 | 2.72 | 0.5 | 10.8 |
| 11x5 | 10526 | 2.86 | 2 | 13.3 |
| 11x5 | 10790 | 3.00 | 2 | 13.3 |
| | | | | |
| 11x6 | 6857 | 1.75 | 0.5 | 10.8 |
| 11x6 | 9022 | 3.03 | 0.25 | 10.8 |
| 11x6 | 9090 | 3.07 | 0.25 | 15 |
| 11x6 | 9404 | 3.29 | 0.25 | 10.8 |
| | | | | |
| 12X6 | 5741 | 1.64 | 0.5 | 17.3 |
| 12X6 | 8240 | 3.38 | min | 9.9 |
| 12x6 | 8400 | 3.51 | min | 20.5 |
| 12x6 | 8474 | 3.57 | min | 16 |
| 12x6 | 8498 | 3.59 | min | 10.8 |
| | | | | |
| 14x8 | 4494 | 2.11 | 0.5-0.75 | 17.3 |
| 14x8 | 4545 | 2.16 | 0.5-0.75 | 15 |
| 14x8 | 6000 | 3.76 | 0.5-0.75 | 11.9 |
| 14x8 | 6000 | 3.76 | 0.75 | 13.3 |
| | | | | |
| 15x10 | 4392 | 3.84 | 0.5 | 15 |
| 15x10 | 4395 | 3.85 | 0.25-0.25 | 15 |
| 15x10 | 4444 | 3.93 | 3.5 | 11.9 |
| 15x10 | 4460 | 3.96 | 2 | 15 |
| 15x10 | 4511 | 4.05 | 0.25 | 11.9 |
| 15x10 | 4563 | 4.15 | 0.5 | 10.8 |

**Batch 2:**

| Prop | Speed | BMEP | Mix screw | Amb T | CR | IMEP | Brk Pow | Max PRR | at CAD | Max HRR | at CAD | Burn Aprx | P | |
|---|---|---|---|---|---|---|---|---|---|---|---|---|---|---|
| Xpitch | rpm | bar | open | C | | bar | Watts | bar/deg | deg | J/deg | deg | deg | b | |
| 11x5 | 11363 | 3.32 | min | 16 | 17 | 4.8 | 412 | 5.1 | 3.5 | 51170 | 3.52 | 19 | | |
| 11x5 | 11278 | 3.27 | min | 16 | 19.9 | 4.0 | 403 | 8.69 | 0.7 | 61785 | 0.7 | 14 | | |
| 11x5 | 11152 | 3.20 | min | 16 | 17 | 3.9 | 390 | 1.49 | 7.5 | 27191 | 8.89 | 20 | | |
| 11x5 | 6258 | 1.00 | 1 turn | 16 | 19.9 | 0.8 | 69 | 1.32 | -23.7 | 6259 | 8.2 | 33 | | |
| 11x5 | 5714 | 0.84 | 1 turn | 16 | 11.1 | 0.9 | 52 | 1.16 | -14.6 | 3683 | 9.36 | 35 | | |
| 11x5 | 5608 | 0.81 | 1 turn | 16 | 14.8 | 1.4 | 50 | 1.1 | -16.4 | 7526 | 8.87 | 32 | | |
| | | | | | | | | | | | | | | |
| 12x6 | 8695 | 3.75 | min | 15 | 14.8 | 5.8 | 356 | 3.48 | 10.1 | 44785 | 11.19 | 18 | | |
| 12x6 | 8670 | 3.73 | min | 15 | 17 | 5.8 | 353 | 9.07 | 2.8 | 66358 | 3.8 | 10.5 | | |
| 12x6 | 8670 | 3.73 | min | 15 | 11.8 | 5.7 | 353 | 10.75 | 4.9 | 113344 | 4.93 | 12 | | |
| 12x6 | 8620 | 3.68 | min | 15 | 11.1 | 5.1 | 347 | 5.29 | 6.2 | 56546 | 6.21 | 12 | | |
| 12x6 | 8522 | 3.54 | min | 15 | 10.8 | 5.8 | 335 | 4.21 | 11.0 | 62925 | 11.01 | 20 | | |
| 12x6 | 8380 | 3.48 | min | 15 | 14.8 | 4.5 | 319 | 13.96 | 2.8 | 107585 | 2.8 | 11 | | |
| 12x6 | 8219 | 3.35 | 3 turn | 15 | 14.8 | 3.3 | 301 | 16.1 | -4.2 | 107187 | -4.18 | 9 | | |
| 12x6 | 8196 | 3.33 | 5 turn | 15 | 14.8 | 4.7 | 298 | 11 | -3.2 | 72037 | -3.23 | 10 | | |
| 12x6 | 8196 | 3.33 | 0.25 turn | 15 | 14.8 | 4.8 | 298 | 18.25 | -1.2 | 126083 | -1.24 | 9 | | |
| 12x6 | 8108 | 3.26 | 4 turn | 15 | 14.8 | 4.9 | 289 | 11.1 | -3.1 | 71247 | -3.11 | 9 | | |
| 12x6 | 8086 | 3.24 | 1 turn | 15 | 14.8 | 3.1 | 286 | 10 | 3.6 | 76886 | 3.62 | 12 | | |
| 12x6 | 8064 | 3.22 | 2 turn | 15 | 14.8 | 3.2 | 284 | 10.8 | 0.7 | 76086 | 1.7 | 13 | | |
| 12x6 | 7978 | 3.15 | 0.5 turn | 15 | 14.8 | 2.2 | 275 | 16.93 | 0.8 | 117468 | 0.75 | 9 | | |
| 12x6 | 5714 | 1.62 | 2 turn | 15 | 14.8 | 1.6 | 101 | 1.3 | -18.2 | 6927 | 7.53 | 24.5 | | |
| 12x6 | 4898 | 1.19 | 1.25 turn | 15 | 14.8 | 2.5 | 64 | 1.03 | -8.1 | 7421 | 9.52 | 40 | | |
| 12x6 | 4858 | 1.17 | 1.25 turn | 15 | 14.8 | 2.1 | 62 | 1.03 | -15.3 | 6833 | 10.95 | 33 | | |
| 12x6 | 4396 | 0.96 | 1.25 turn | 15 | 14.8 | 2.1 | 46 | 1.03 | -11.2 | 5380 | 12.57 | 35 | | |
| | | | | | | | | | | | | | | |
| 15x10 | 4706 | 4.40 | min | 17 | 9.2 | 6.8 | 226 | 12.05 | 5.0 | 88280 | 4.99 | 11 | | |
| 15x10 | 4615 | 4.23 | 0.75 turn | 17 | 10.8 | 6.2 | 213 | 12.35 | -3.4 | 66140 | -3.4 | 12 | | |
| 15x10 | 2575 | 1.32 | 1 turn | 17 | 17 | 1.5 | 37 | 1.32 | -14.8 | 4653 | 8.4 | 31 | | |
| 15x10 | 2521 | 1.26 | 2.5 turn | 17 | 18.8 | 1.4 | 35 | 1.45 | -13.2 | 3403 | 11 | 34 | | |
| 15x10 | 3636 | 2.61 | min | 17 | 20.5 | | 106 | 41 | -13.5 | 111683 | -13.5 | 4.5 | 1 | |
| 15x10 | 3974 | 3.11 | min | 17 | 13.3 | 2.7 | 135 | 26 | -7.7 | 16 | -7.7 | 7 | 1 | |
| 15x10 | 3845 | 2.90 | min | 17 | 17.3 | 2.9 | 122.6 | 44 | -8.0 | 128788 | -8 | 5 | 1 | |

**Batch 3:**

| Prop | Speed | BMEP | Lambda | CR | Amb T | IMEP | Brk Pow | Max PRR | at CAD | Max HRR | at CAD | Burn Aprx | P | |
|---|---|---|---|---|---|---|---|---|---|---|---|---|---|---|
| Xpitch | rpm | bar | | | C | bar | Watts | bar/deg | deg | J/deg | deg | deg | b | |
| 12x6 | 8797 | 3.75 | 1 | 14.8 | 20 | 8.5 | 360 | 8.1 | 9.4 | 85954 | 9.4 | 14 | | |
| 12x6 | 8746 | 3.73 | 0.9 | 14.8 | 20 | 7.6 | 356 | 6 | 10.4 | 68044 | 10.4 | 18 | | |
| 12x6 | 8721 | 3.71 | 0.96 | 17 | 20 | 7.4 | 353 | 10.8 | 2 | 74032 | 2 | 12 | | |
| 12x6 | 8721 | 3.71 | 0.95 | 19.9 | 20 | 6.1 | 353 | 13.7 | 0 | 73826 | 0 | 9 | | |
| 12x6 | 8670 | 3.67 | 1 | 13.1 | 20 | 7.2 | 347 | 4.3 | 11.4 | 59203 | 11.4 | 16 | | |
| 12x6 | 8621 | 3.62 | 1 | 15 | 20 | 6.9 | 341 | 5.1 | 11.4 | 67919 | 11.4 | 18 | | |
| 12x6 | 8621 | 3.62 | 0.95 | 17 | 20 | 7 | 341 | 7.3 | 5.2 | 57738 | 5.2 | 16 | | |
| 12x6 | 4938 | 1.2 | 0.96 | 14.8 | 20 | 2.5 | 64 | NA | NA | NA | NA | 31 | | |
| 12x6 | 4878 | 1.16 | 0.98 | 11.8 | 20 | 3.2 | 62 | NA | NA | NA | NA | 28 | | |
| 12x6 | 4761 | 1.1 | 0.98 | 11.8 | 20 | 3.2 | 58 | NA | NA | NA | NA | 31 | | |
| 12x6 | 4316 | 0.91 | 0.98 | 13.1 | 20 | 3 | 43 | NA | NA | NA | NA | 36 | | |
| | | | | | | | | | | | | | | |
| 15x10 | 4580 | 4.1 | 1.43 | 9.9 | 19 | 11.9 | 205 | 10.8 | 10.7 | 81450 | 10.7 | 12 | | |
| 15x10 | 4580 | 4.07 | 1.65 | 10.8 | 22 | 9.3 | 200 | 7.9 | 11.7 | 60993 | 13.1 | 13 | | |
| 15x10 | 4573 | 4.01 | 1.4 | 11.8 | 26 | 8.5 | 200 | 14.9 | 0 | 267078 | 0 | 9 | | |
| 15x10 | 4545 | 4.01 | 1.03 | 9.9 | 22 | 8.8 | 199 | 7 | 13 | 58715 | 13 | 14 | | |
| 15x10 | 4545 | 4.01 | 0.97 | 9.2 | 22 | 8.9 | 199 | 6.8 | 10.3 | 56493 | 10.3 | 12 | | |
| 15x10 | 4511 | 4 | 1.64 | 9.9 | 19 | 8.9 | 197 | 8.9 | 10.3 | 67230 | 10.3 | 12 | | |
| 15x10 | 4478 | 3.92 | 1.03 | 11.8 | 19 | 7.7 | 192 | 16.6 | 0 | 83036 | 0 | 9 | | |
| 15x10 | 4461 | 3.8 | 0.94 | 11.8 | 26 | 7.4 | 189 | 9.4 | 2.2 | 48096 | 2.2 | 10 | | |
| 15x10 | 4363 | 3.72 | 0.96 | 13.9 | 19 | 7.3 | 178 | 13.6 | -3 | 51384 | -3 | 8 | | |
| 15x10 | 4332 | 3.59 | 1 | 19.9 | 27 | 7.6 | 170 | 14.2 | -4.2 | 34239 | -4.2 | 8 | | |
| 15x10 | 3085 | 1.82 | 0.95 | 9.9 | 26 | 1.8 | 65 | NA | NA | NA | NA | 24 | | |
| 15x10 | 2948 | 1.7 | 0.95 | 9.9 | 26 | 2 | 54 | NA | NA | NA | NA | 29 | | |
| 15x10 | 2685 | 1.4 | 1 | 10.8 | 22 | 2 | 41 | NA | NA | NA | NA | 24 | | |
| 15x10 | 2643 | 1.33 | 0.93 | 19.9 | 27 | 1.5 | 38.5 | NA | NA | NA | NA | 35 | | |
| 15x10 | 2637 | 1.35 | 1 | 10.8 | 22 | 2.1 | 38.9 | NA | NA | NA | NA | 32 | | |

**Batch 4:**

| Prop | Speed | BMEP | Lambda | CR | Amb T | Ex T | IMEP | Brk Pow | Max PRR | at CAD | Max HRR | at CAD | Burn Aprx | | |
|---|---|---|---|---|---|---|---|---|---|---|---|---|---|---|---|
| Xpitch | rpm | bar | | | C | C | bar | Watts | bar/deg | deg | J/deg | deg | deg | | |
| 11x5 | 10423 | 2.8 | 0.95 | 16.7 | 22 | 281 | 5.3 | 314 | 4.3 | 3.7 | 42898 | 5 | 29 | | |
| 11x5 | 10274 | 2.7 | 0.98 | 15 | 22 | 271 | 4.8 | 298 | 7.4 | -1 | 62158 | 0 | 13 | | |
| 11x5 | 5195 | 0.7 | 1 | 14.8 | 22.5 | 115 | 2.7 | 38 | NA | NA | NA | NA | 33 | | |
| | | | | | | | | | | | | | | | |
| 11x6 | 9434 | 3.2 | 0.97 | 15 | 22 | 290 | 6.34 | 333 | 5.9 | 6.2 | 61123 | 6.2 | 18.5 | | |
| | | | | | | | | | | | | | | | |
| 12x6 | 8676 | 3.6 | 0.98 | 16.7 | 22 | 230 | 6.63 | 342 | 12.4 | 3.1 | 88103 | 3.1 | 17 | | |
| 12x6 | 8475 | 3.5 | 0.97 | 13 | 22 | 224 | 7.2 | 322 | 7.2 | 6.2 | 76391 | 7.2 | 21 | | |
| | | | | | | | | | | | | | | | |
| 15x10 | 4511 | 4 | 1.01 | 9.1 | 22 | 205 | 8.5 | 195 | 9 | 8.9 | 70846 | 8.9 | 10 | | |
| 15x10 | 4428 | 3.8 | 1 | 8 | 22 | 205 | 7.9 | 184 | 9.8 | 7.5 | 82298 | 7.5 | 12 | | |
| 15x10 | 4428 | 3.8 | 1.67 | 9.8 | 22 | 252 | 8.1 | 184 | 12.7 | 3.5 | 79868 | 3.5 | 10 | | |
| 15x10 | 4332 | 3.6 | 1.6 | 11.7 | 22 | 225 | 7 | 172 | 16.6 | -0.3 | 78700 | -0.3 | 9 | | |

**Batch 5:**

| Prop | Speed | BMEP | Lambda | CR | Amb T | Ex T | Fuel | IMEP | Brk Pow | Max PRR | at CAD | Max HRR | at CAD | | | |
|---|---|---|---|---|---|---|---|---|---|---|---|---|---|---|---|---|
| Xpitch | rpm | bar | | | C | C | | bar | Watts | bar/deg | deg | J/deg | deg | | | |
| 11x5 | 10101 | 2.60 | 0.8 | 15 | 24 | 290 | D1000 | 4.2 | 281 | 7 | -0.5 | 58460 | -0.5 | | | |
| 11x5 | 9868 | 2.44 | 1 | 15 | 24 | 307 | D1000 | 4.17 | 263 | 9.8 | -1.5 | 101064 | 0 | | | |
| 11x5 | 9449 | 2.2 | 1.4 | 15 | 24 | 317 | D1000 | 3.33 | 231 | 4.7 | -3.4 | 82065 | 0 | | | |
| | | | | 15 | | | | | | | | | | | | |
| 12x6 | 4636 | 1 | 0.8 | 15 | 26 | 170 | D1000 | 1.5 | 52 | NA | NA | NA | NA | | | |
| 12x6 | 4878 | 1.1 | 0.9 | 15 | 26 | 154 | GTL10C | 1.7 | 61 | NA | NA | NA | NA | | | |
| 12x6 | 4878 | 1.1 | 0.75 | 15 | 26 | 150 | GTL10B | 1.5 | 52 | NA | NA | NA | NA | | | |
| 12X6 | 4878 | 1.1 | 1 | 15 | 26 | 160 | GTL10B | 1.1 | 61 | NA | NA | NA | NA | | | |
| 12X6 | 5300 | 1.34 | 0.74 | 15 | 26 | 156 | D1000 | 2.22 | 78 | NA | NA | NA | NA | | | |
| 12X6 | 5465 | 1.4 | 0.75 | 15 | 26 | 148 | GTL10C | 2.9 | 85 | NA | NA | NA | NA | | | |
| 12X6 | 5952 | 1.7 | 1.2 | 15 | 26 | 170 | D1000 | 2.6 | 110 | NA | NA | NA | NA | | | |
| 12x6 | 6579 | 2.1 | 0.9 | 15 | 26 | 254 | GTL10B | 4.3 | 149 | 39 | -10.4 | 232669 | -10.4 | | | |
| 12X6 | 6849 | 2.2 | 1.6 | 15 | 26 | 260 | GTL10B | 3.7 | 168 | 6 | 0.5 | 59051 | 0 | | | |
| 12X6 | 6896 | 2.3 | 1.6 | 15 | 26 | 250 | GTL10C | 4.1 | 171 | 5.8 | 0.44 | 39826 | 0 | | | |
| 12X6 | 6976 | 2.33 | 1.25 | 15 | 26 | 300 | GTL10C | 5.2 | 178 | 17.3 | -9.8 | 98921 | -9.8 | | | |
| 12X6 | 7595 | 2.8 | 1 | 15 | 26 | 316 | D1000 | 4.7 | 229 | 18.5 | -8.4 | 116459 | -8.4 | | | |
| 12x6 | 8108 | 3.15 | 0.75 | 15 | 26 | 220 | GTL10B | 5.2 | 279 | 6.5 | -0.6 | 77553 | 0 | | | |
| 12x6 | 8264 | 3.27 | 0.75 | 15 | 26 | 213 | GTL10C | 5.6 | 295 | 9.5 | -3.7 | 59594 | -3.7 | | | |
| 12X6 | 8499 | 3.46 | 1 | 15 | 26 | 320 | D1000 | 5.3 | 321 | 16.1 | -1.9 | 112183 | -1.9 | | | |
| 12X6 | 8571 | 3.52 | 0.85 | 15 | 26 | 290 | GTL6 | 6.8 | 329 | 4.4 | 9.3 | 51874 | 9.3 | | | |
| 12x6 | 8596 | 3.54 | 0.9 | 15 | 26 | 292 | GTL3 | 6.55 | 332 | 11.9 | 3.2 | 95248 | 4.2 | | | |
| | | | | | | | | | | | | | | | | |
| 15x10 | 3821 | 2.8 | 1.2 | 15 | 24 | 220 | D1000 | 4.5 | 118 | 18.4 | -6.3 | 56157 | -6.3 | | | |

**Batch 6:**

| Prop | Speed | BMEP | Lambda | CR | Amb T | Ex T | IMEP | Brk Pow | Max PRR | at CAD | Max HRR | at CAD | B A | | |
|---|---|---|---|---|---|---|---|---|---|---|---|---|---|---|---|
| Xpitch | rpm | bar | | | C | C | bar | Watts | bar/deg | deg | J/deg | deg | d | | |
| | | | | | | | | | | | | | | | |
| 11x5 | 10170 | 2.58 | 0.81 | 12.3 | 25 | 240 | 3.2 | 286 | 4.82 | 0.1 | 40948 | 0.1 | | | |
| | 6881 | 1.18 | 0.9 | 12.3 | | 130 | 3 | 89 | NA | NA | NA | NA | | | |
| | | | | | | | | | | | | | | | |
| 11x6 | 8310 | 2.5 | 0.82 | 12.3 | | 252 | 3.4 | 225 | 2 | 5.2 | 20490 | 7.2 | | | |
| | 7110 | 1.82 | 0.87 | 12.3 | | 205 | 2.8 | 141 | NA | NA | NA | NA | | | |
| | | | | | | | | | | | | | | | |
| 12x6 | 7518 | 2.7 | 0.78 | 12.3 | | 223 | 3.9 | 223 | 4.75 | 3.5 | 34177 | 3.5 | | | |
| | 4781 | 1.1 | 0.9 | 12.3 | | 137 | 1.7 | 57.3 | NA | NA | NA | NA | | | |
| | 7042 | 2.4 | 0.92 | 12.3 | | 250 | 3.5 | 183 | 5.2 | 1.1 | 31974 | 1.1 | | | |
| | 5240 | 1.3 | 0.92 | 11.9 | | 166 | 1.7 | 75.5 | NA | NA | NA | NA | | | |
| | 6936 | 2.3 | 0.87 | 11.9 | | 220 | 2.9 | 175 | NA | NA | NA | NA | | | |
| | 8242 | 3.3 | 0.92 | 11.9 | | 278 | 4.8 | 294 | 7 | 5.2 | 57022 | 6.2 | 1 | | |
| | 8596 | 3.6 | 0.9 | 11.9 | | 290 | 5.1 | 333 | 4.3 | 10.3 | 45378 | 10.3 | | | |
| | | | | | | | | | | | | | | | |
| 13x6 | 6897 | 2.6 | 0.9 | 12.3 | | 250 | 3.8 | 199 | 3 | 7.1 | 24720 | 7.9 | | | |
| | | | | | | | | | | | | | | | |
| 14x8 | 5063 | 2.6 | 0.79 | 12.3 | | 182 | 4 | 143 | 5.3 | -2.9 | 21007 | -1.4 | | | |
| | 4762 | 2.3 | 0.9 | 12.3 | | 213 | 3.5 | 119 | 2.5 | 6.2 | 13806 | 6.2 | | | |
| | | | | | | | | | | | | | | | |
| 15x8 | 4706 | 2.8 | 0.88 | 12.3 | | 195 | 2.7 | 142 | 16.4 | -7.9 | 62536 | 7.9 | | | |
| | 4511 | 2.5 | 0.81 | 12.3 | | 202 | 3 | 125 | 5.8 | 1.2 | 22791 | 1.2 | | | |
| | | | | | | | | | | | | | | | |
| 15x10 | 3822 | 2.8 | 0.81 | 12.3 | | 187 | 3.6 | 117 | 18.1 | -8.7 | 57484 | -8.7 | | | |

## 9.4. TEST EQUIPMENT SPECIFICATIONS

**Propeller rig motor type and specification:** “SKIL 1830” speed range: 0-28000rpm, 4.9A 230V AC, rated power: 1100W

**Photo tachometer type and specification:** LT type “DT-2236” Range: 5 to 99999rpm, Resolution: 1rpm

**IQT$^{TM}$ type and specification:** Advanced Engine Technologies’ “IQT$^{TM}$- Laboratory Model” compliant with ASTM D6890 testing standard

**In-Cylinder Pressure Transducer type and specification:** “AVL GU12P” sensitivity: 0-200bar temperature range: 400°C or “AVL 6 QP 500a” sensitivity: 0-100bar temperature range: 0-240°C connected to Kistler Charge Amplifier type 5105

**Exhaust Silencer Pressure Transducer**: Same as In-Cylinder Pressure Transducer

**Oscilloscope type and specification:** “Agilent Technologies DSO6014A” 4-channel with sampling rate: 100MHz (2Gsa/s)

**Crank-Case TP type, specification and charge amp:** ”Kistler Piezoresistive 4073” sensitivity: 0-10bar (absolute) water-cooled jacket connected to Kistler Charge Amplifier type 4603

**Thermocouple type and display**: All K-type thermocouples connected to “Fluke 52” thermocouple display

**Lambda sensor type and specification:** “Bosch LSM11 0 258 104 002” connected to “ETAS LA2” power supply and display unit

**Starter motor type:** “Thunder Tiger 12V type 2674 Deluxe Hi-Torque”

**Horiba Emissions Equipment**: “MEXA 7200D”

## 9.5. CHEMKIN THERMODATA TABLES

**Low Temperature Range (300K to 1500K) Data:**

| | | | | | | Chemkin ref | Chemkin ref | Range | 30 |
|---|---|---|---|---|---|---|---|---|---|
| | cpa | cpb | cpc | cpd | cpe | (hf0298-h0298) | (sf0298-s0298) | hf0298 | sf |
| co2 | 18.93376 | 0.08255 | -8.7E-05 | 5.71E-08 | -1.8E-11 | -402458.8824 | 84.76703173 | -393805.2172 | |
| co | 27.14321 | 0.012579 | -3.2E-05 | 4.64E-08 | -2.1E-11 | -119062.0152 | 40.34225745 | -110613.4391 | |
| h2o | 28.17813 | 0.028911 | -5.3E-05 | 5.8E-08 | -2.1E-11 | -251327.9516 | 21.5504281 | -242003.9985 | |
| h2 | 27.44001 | 0.006863 | -6.8E-06 | -7.9E-10 | 3.44E-12 | -8424.055784 | -27.40647784 | 2.45022734 | |
| o2 | 26.73125 | 0.009381 | -4.8E-06 | 1.09E-08 | -7.3E-12 | -8363.554424 | 50.20830792 | -0.848205595 | |
| n2 | 27.44461 | 0.011716 | -3.3E-05 | 4.69E-08 | -2E-11 | -8493.768086 | 32.86663425 | 1.430834294 | |
| heptane | -5.146 | 0.6762 | -0.00037 | 7.66E-08 | 0 | -213098.0463 | 271.2361802 | -187650 | |

**High Temperature Range (1000 to 5000K) Data:**

| | | | | | | Chemkin ref | Chemkin ref | Range | 10 |
|---|---|---|---|---|---|---|---|---|---|
| J/molK | cpa | cpb | cpc | cpd | cpe | (hf0298-h0298) | (sf0298-s0298) | hf0298 | sf |
| co2 | 37.05362 | 0.026126 | -1.1E-05 | 1.99E-09 | -1.4E-13 | -407399.3955 | -7.948782447 | -395280.7469 | |
| co | 25.1683 | 0.012003 | -4.7E-06 | 8.47E-10 | -5.7E-14 | -118711.0077 | 50.81965295 | -110713.3271 | |
| h2o | 22.23193 | 0.025428 | -7.3E-06 | 9.99E-10 | -5.3E-14 | -248757.9396 | 57.09783693 | -241061.5177 | |
| h2 | 24.88829 | 0.005824 | -4.7E-07 | -7.7E-11 | 1.32E-14 | -6947.385478 | -11.27435797 | 727.6496309 | |
| o2 | 30.76342 | 0.005104 | -1E-06 | 1.48E-10 | -9.5E-15 | -10266.1545 | 26.5334808 | -876.132622 | |
| n2 | 24.3493 | 0.01238 | -4.7E-06 | 8.4E-10 | -5.6E-14 | -7677.569225 | 49.75729537 | 92.26552451 | |
| heptane | -5.146 | 0.6762 | -0.00037 | 7.66E-08 | 0 | -213098.0463 | 271.2361802 | -187650 | |

## 9.6. FUEL PROPERTIES FOR AUTOIGNITION MODELS

| Autoignition | Stage 1 | | | Peroxides | | | Cool Flame Temps | | |
|---|---|---|---|---|---|---|---|---|---|
| Fuel Data | Ln(A1) | n1 | B1 | Ln(Ah) | nh | Bh | Tequil | w | Kpress |
| n-Heptane | -18.68 | -0.073 | 14715 | -10.59 | -0.975 | 13853 | 837.3 | -1.341 | 0.041 |

| | Air-Fuel Equivalnce | | | |
|---|---|---|---|---|
| Co effs | 1 | h | µ | |
| n-Heptane | -0.083 | -0.408 | 0.041 | 0.247 |

## 9.7 WOSHNI HEAT TRANSFER MODE COEFFICIENTS

| | |
|---|---|
| Woshni compress C1 | 2.28 |
| Woshni compress C2 | 0 |
| Woshni Comb-Exp C1 | 2.28 |
| Woshni Comb-Exp C2 | 3.24E-03 |
| Woshni C | 3.26 |
| Woshni m | 0.8 |

## 9.8. ENTROPY (ΔS) DERIVATION (BY G FLOWEDAY)

$$dS_{sys} \geq \frac{dQ}{T}$$

where $dS = \frac{dQ_{\text{int}\,rev}}{T}$

$$dQ_{\text{int}\,rev} - dW_{\text{int}\,rev} = dU \qquad \text{(1st law of thermodynamics)}$$

$$dQ_{\text{int}\,rev} = T\ dS \qquad \text{(defn of } dS\text{)}$$

$$dW_{\text{int}\,rev} = F\ dx = PAdx = PdV \quad \text{(defn of } W\text{)}$$

Subst : $T\ dS = dU + PdV$ (1st TdS eqn, Gibbs function)

Since : h = u + pv (defn of $h$)

$$dh = du + p\,dv + v\,dp$$

Subst into Gibbs : $T\ dS = dh - v\,dp$ (2nd TdS eqn)

since : $dh = C_p dT$ (defn of $C_p$)

and : $v = \frac{RT}{P}$ ($I$deal gas law)

$$dS = \frac{dh}{T} - \frac{v\,dp}{T} = \frac{C_p dT}{T} - \frac{R\,dp}{P}$$

$$\int_1^2 dS = \int_1^2 \frac{C_p}{T} dT - R\int_1^2 \frac{1}{P} dP$$

$$S_2 - S_1 = \int_1^2 \frac{C_{pA} + C_{p\mathbf{B}}T + C_{pC}T^2 + C_{pD}T^3 + C_{pE}T^4}{T} dT - R\left[\ln P\right]_1^2$$

$$= \left[C_{pA}\ln T + C_{p\mathbf{B}}T + \frac{C_{pC}T^2}{2} + \frac{C_{pD}T^3}{3} + \frac{C_{pE}T^4}{4} + const\right]_1^2 - R\left(\ln P_2 - \ln P_1\right)$$

now, remember :

$$S_{state} = S_{sens} + S_{f,T=0K}$$

$$S^0_{state} = S^0_{sens} + S^0_{f,T=0K} = S^0_{sens} + (S_{f,T=298K} - S^0_{sens,T=298K})$$

$$= S^0_{sens}\Big|_T - S^0_{sens}\Big|_0 + (S_{f,T=298K} - (S^0_{sens}\Big|_{298} - S^0_{sens}\Big|_0))$$

$$= S^0_{sens}\Big|_T + \text{(chemkin ref)}$$

## 9.9. Kp DERIVATION (BY G FLOWEDAY)

Consider reaction components: A, B, C, D

Stoichiometric coefficients: $v_A$, $v_B$, $v_C$, $v_D$

$$v_A A + v_B B \rightarrow v_C C + v_D D$$

And equilibrium mole numbers: $N_A$, $N_B$, $N_C$, $N_D$

$$N_A A + N_B B \xleftrightarrow[equilibrium]{} N_C C + N_D D$$

$$\text{at equilibrium}: (\mathrm{dG})_{\text{const T\&P}} = \Sigma\left(g_i dN_i\right)_{\text{const T\&P}} = 0$$

Where: $g_i$ is molar Gibbs values

$dN_i$ is the differential change in # of moles

From stoichiometric reaction:

$$v_A A + v_B B \rightarrow v_C C + v_D D$$

We don't know $N_i$ values, but the differential changes are proportional, so:

$$dN_A = -\varepsilon v_A \qquad dN_C = +\varepsilon v_C$$
$$dN_B = -\varepsilon v_B \qquad dN_D = +\varepsilon v_D$$

Where ε is proportionality constant and represents the extent of reaction movement

NB: sign convention -ve for reactants, +ve for products

$$\text{at equilibrium}: (\mathrm{dG})_{\text{const T\&P}} = \Sigma\left(g_i dN_i\right)_{\text{const T\&P}} = 0$$

$$g_A dN_A + g_B dN_B + g_C dN_C + g_D dN_D = 0 \quad (\text{const T \& P})$$

subst $\varepsilon$ expressions:

$$-g_A \varepsilon v_A - g_B \varepsilon v_B + g_C \varepsilon v_C + g_D \varepsilon v_D = 0 \quad (\text{const T \& P})$$

devide through by $\varepsilon$:

$$-g_A v_A - g_B v_B + g_C v_C + g_D v_D = 0 \quad (\text{const T \& P})$$

$\overset{0}{g}_i = \overset{0}{h}_i + T\,\overset{0}{s}_i$ i.e. at 1 atm

Problem: Gibbs is function of T and P

approach: devide the effects

$$\int_1^2 dS = \int_1^2 \frac{C_p}{T}\,dT - R\int_1^2 \frac{1}{P}\,dP$$

$$S_2 - S_1 = \int_1^2 \frac{C_{pA} + C_{p\mathbf{B}}T + C_{pC}T^2 + C_{pD}T^3 + C_{pE}T^4}{T}\,dT - R\left[\ln P\right]_1^2$$

$$= \left[C_{pA}\ln T + C_{p\mathbf{B}}T + \frac{C_{pC}T^2}{2} + \frac{C_{pD}T^3}{3} + \frac{C_{pE}T^4}{4} + const\right]_1^2 - R\left(\ln P_2 - \ln P_1\right)$$

now, remember:

$$S_{state} = S_{sens} + S_{f,T=0K}$$

$$S^0_{state} = S^0_{sens} + S^0_{f,T=0K} = S^0_{sens} + (S_{f,T=298K} - S^0_{sens,T=298K})$$

$$= S^0_{sens}\Big|_T - S^0_{sens}\Big|_0 + (S_{f,T=298K} - (S^0_{sens}\Big|_{298} - S^0_{sens}\Big|_0))$$

$$= S^0_{sens}\Big|_T + (\text{chemkin ref})$$

$\overset{0}{g}_i = \overset{0}{h}_i + T\,\overset{0}{s}_i$ i.e. at 1 atm

$$g_{i(p,T)} = \overset{0}{g}_{i(T)} + P_{correction,T=const}$$

$$P_{correction,T=const} \rightarrow \quad \Delta g = \Delta h - T\Delta s$$

$$\Delta h_{T=const} = 0 \qquad \Delta s_{T=const} = -R\ln\frac{P_2}{P_1}$$

$$P_{correction,T=const} \rightarrow \quad \Delta g = +RT\ln\frac{P_2}{P_1}$$

$g_{i(p,T)} = \overset{0}{g}_{i(T)} + RT\ln P_i$ for partial P in atm

$-g_A\nu_A - g_B\nu_B + g_C\nu_C + g_D\nu_D = 0$ (const T & P)

$$-\left[\overset{0}{g}_A + RT\ln P_A\right]\nu_A - [\ldots]\nu_B + [\ldots]\nu_C + [\ldots]\nu_D = 0$$

define $\Delta G^* = -\overset{0}{g}_A\nu_A - \overset{0}{g}_B\nu_B + \overset{0}{g}_C\nu_C + \overset{0}{g}_D\nu_D$

subst: $\Delta G^* = -RT(-\nu_A\ln P_A - \nu_B\ln P_B + \nu_C\ln P_C + \nu_D\ln P_D)$

$$\therefore\ \Delta G^* = -R_u T \ln\left[\frac{P_C^{\nu_C} P_D^{\nu_D}}{P_A^{\nu_A} P_B^{\nu_B}}\right]$$

define $K_{p1} = [\ ]$

then $K_{p1} = e^{-\Delta G^*/R_u T}$

$$K_{p1} = \left[\frac{P_C^{\nu_C} P_D^{\nu_D}}{P_A^{\nu_A} P_B^{\nu_B}}\right]$$

from partial pressure relation : $P_i = \frac{N_i P_{total}}{N_{total}}$

subst in : $K_{p2} = \left[\frac{N_C^{\nu_C} N_D^{\nu_D}}{N_A^{\nu_A} N_B^{\nu_B}}\right]\left(\frac{P_{total}}{N_{total}}\right)^{\Delta\nu}$

where : $\Delta\nu = \nu_C + \nu_D - \nu_A - \nu_B$

so at equilibrium : $K_{p1} = K_{p2}$